

# Micro scale modeling grain boundary damage under creep conditions

**Dissertation**

zur Erlangung des akademischen Grades

**Doktoringenieur**

**(Dr.-Ing.)**

von M.Sc. Oksana Ozhoga-Maslovskaja  
geb. am 17.10.1986 in Kharkiv  
genehmigt durch die Fakultät für Maschinenbau  
der Otto-von-Guericke-Universität Magdeburg

Gutachter:

Prof. Dr.-Ing.habil. Dr.h.c. Holm Altenbach

Prof. Elisabetta Gariboldi

Promotionskolloquium am 24.01.2014



# Abstract

The current thesis deals with the investigation of the grain boundary cavitation in polycrystalline aggregates. The main idea is to perform the simulation with just some micromechanisms directly influencing the cavitation process. These are the power law creep in the grain interior, the grain boundary sliding and the growth of grain boundary cavities. This assumption is taken on the one hand due to complexity of the mechanisms taking place in real polycrystals during creep and on the other hand in order to investigate the pure contribution of chosen mechanisms.

To achieve this aim the numerical procedure is developed allowing to construct the geometry of a polycrystalline aggregate by means of the unit cell. The anisotropic nature of the grain interior material is introduced by the randomly oriented coordinate system for each grain. The special grain boundary region represents the sliding of mutual grains. The grain boundary sliding leads to the significant stress concentrations, which force the cavity growth. The following observation within the numerical simulation is fully consistent with the experimental one. Both the cavitation and stiffness reduction models are introduced for the grain boundary region to simulate grain boundary damage.

The contribution of the above mentioned mechanisms to each of three creep stages is analyzed. Additionally the case of non-proportional loading is analyzed. The creep strain rate reduction after the principal stresses rotation is observed, leading to the prolongation of the time to rupture.

# Zusammenfassung

Die vorliegende Arbeit beschäftigt sich mit Untersuchungen zur Kavitation an Korngrenzen in Polykristallen. Das Hauptaugenmerk liegt auf Simulationen unter Berücksichtigung von nur einigen Mikromechanismen, die den Kavitationsprozess direkt beeinflussen. Diese sind das Potenzgesetz-Kriechen im Korninneren, das Gleiten der Korngrenzen und das Anwachsen der Korngrenzhohlräume. Diese Annahme wird getroffen, einerseits aufgrund der Komplexität der während des Kriechens auftretenden Mechanismen in realen Polykristallen und andererseits um den Einfluss der gewählten Mechanismen zu untersuchen.

Um dieses Ziel zu erreichen wird ein numerisches Verfahren, welches die Konstruktion von Polykristallen mit Hilfe einer Einheitszelle erlaubt, entwickelt. Die anisotrope Natur des Korninneren wird über ein zufällig orientiertes Koordinatensystem für jedes Korn eingeführt. Die spezielle Korngrenzenregion stellt das gegenseitige Verschieben der Körner dar. Die Korngrenzverschiebung führt zu signifikanten Spannungskonzentrationen, welche Hohlraumwachstum erzwingen. Dieses Phänomen wurde sowohl in der numerischen Simulation, als auch im Experiment beobachtet. Für die Simulation von Korngrenzenschäden in der Korngrenzenregion werden sowohl Kavitations- als auch Steifigkeitsreduktionsmodelle eingeführt.

Die Beiträge der oben genannten Mechanismen zu jedem der drei Kriechstadien werden analysiert. Zusätzlich wird der Fall einer nicht-proportionalen Belastung untersucht. Die Reduzierung der tertiären Kriechrate wird bezüglich der Hauptachsenrotation untersucht, was zu einer Verlängerung der Zeit bis zum Bruch führt.

# Preface

This thesis is written in time period from 2010 to 2013. Within this period I had a position of the scientific employee in Otto-von-Guericke University of Magdeburg. Current position was kindly provided by the graduate school 1554 'Micro–Macro–Interactions in structured Media and Particle Systems' financed by DFG (Deutsche Forschungsgemeinschaft). I would like to acknowledge Otto-von-Guericke-University Magdeburg for the excellent work conditions, allowing me to concentrate on the research and accomplish the study in a such short period.

I would like to thank my supervisors Prof. Dr.-Ing.habil. Konstantin Naumenko and Prof. Dr.-Ing.habil. Dr.h.c. Holm Altenbach, which accepted me as a PhD student in their group and guided me through the all research time, giving the motivation and excellent example of scientific work.

Also I would like to express my acknowledge to Prof. Gariboldi for giving the possibility to perform creep experiments at her laboratory and further being reviewer of this thesis.

The micrographs of the tested specimens were performed with the assistance of Jun.-Prof. Dr.-Ing. Manja Krüger from the Institute of Materials and Joining Technology at the Otto-von-Guericke-University Magdeburg.

Also I would like to appreciate the help of M. Sc. Oleksandr Prygorniev for the creating of programming code to build polycrystalline microstructure. The big appreciation to all my colleagues from the department of Engineering Mechanics of Otto-von-Guericke University Magdeburg for the creative and friendly work atmosphere and fruitful discussions.

Many love and thanks I would like to express to my family: Oleg, Tatjana and Olena and to my boyfriend Stephan Baer for their unfailing support.






---

# Contents

|   |            |
|---|------------|
| <b>Contents</b>   | <b>I</b>   |
| <b>List of Figures</b>  | <b>V</b>   |
| <b>List of Tables</b>   | <b>VII</b> |
| <b>1 Introduction and Motivation</b>                            | <b>1</b>   |
| 1.1 Introduction . . . . .                                      | 1          |
| 1.2 Motivation . . . . .  | 4          |
| <b>2 Constitutive modeling of a polycrystalline material</b>    | <b>9</b>   |
| 2.1 Elasticity . . . . .  | 10         |
| 2.2 Variation of elastic properties in crystals . . . . .       | 13         |
| 2.3 Creep . . . . .   | 15         |
| 2.3.1 General Remarks . . . . .                                 | 15         |
| 2.3.2 Constitutive Equations Based on Creep Potential . . . . . | 17         |
| 2.3.3 Identification of creep parameters . . . . .              | 22         |
| 2.3.4 Crystallographic approach . . . . .                       | 24         |
| 2.3.5 Comparison of both approaches . . . . .                   | 26         |
| 2.3.5.1 Comparison by the predicted creep strain rate           | 26         |
| 2.3.5.2 Creep properties variation in single crystal . .        | 30         |
| <b>3 Grain boundary sliding</b>                                 | <b>35</b>  |
| 3.1 Nature of the grain boundary sliding . . . . .              | 35         |
| 3.2 Grain boundary sliding modeling . . . . .                   | 37         |

|          |  |           |
|----------|--|-----------|
| <b>4</b> | <b>Creep cavitation</b>  | <b>43</b> |
| 4.1      | Overview of existing models . . . . .                              | 43        |
| 4.1.1    | Cavitation due to diffusion processes . . . . .                    | 43        |
| 4.1.2    | Cavitation models based on dislocation creep . . . . .             | 44        |
| 4.1.3    | Cavitation due to various mechanisms . . . . .                     | 45        |
| 4.2      | Tvergaard's cavitation model . . . . .                             | 45        |
| 4.2.1    | Cavity nucleation and growth equations . . . . .                   | 45        |
| 4.2.2    | Creep strain rate evolution due to cavitation . . . . .            | 47        |
| 4.3      | Influence of cavities on the material behavior . . . . .           | 48        |
| <b>5</b> | <b>Numerical implementation</b>                                    | <b>53</b> |
| 5.1      | Geometrical representation of polycrystal . . . . .                | 53        |
| 5.2      | Material model implementation . . . . .                            | 56        |
| 5.3      | Calculation of averaged fields in the unit cell . . . . .          | 57        |
| 5.4      | Statistical analysis of the unit cell . . . . .                    | 58        |
| 5.5      | Choice of the representative number of grains . . . . .            | 61        |
| 5.6      | Choice of the grain boundary region thickness . . . . .            | 62        |
| <b>6</b> | <b>Tensile creep tests for polycrystalline copper at 550 °C</b>    | <b>65</b> |
| 6.1      | Choice of the specimen and test conditions . . . . .               | 65        |
| 6.2      | Experimental procedure . . . . .                                   | 66        |
| 6.3      | Experimental results . . . . .                                     | 68        |
| 6.4      | Validation of the secondary creep stage . . . . .                  | 68        |
| 6.5      | Micrographs of copper under different applied stresses . . . . .   | 70        |
| <b>7</b> | <b>Model application</b>   | <b>73</b> |
| 7.1      | Verification of the model by the separate creep region . . . . .   | 73        |
| 7.1.1    | Primary creep stage validation . . . . .                           | 73        |
| 7.1.2    | Secondary creep stage verification . . . . .                       | 75        |
| 7.1.3    | Tertiary creep stage verification . . . . .                        | 76        |
| 7.2      | Non-proportional loading test . . . . .                            | 78        |
| 7.2.1    | Continuum damage mechanics approach . . . . .                      | 78        |
| 7.2.1.1  | Isotropic damage . . . . .   | 78        |
| 7.2.1.2  | Anisotropic damage . . . . .                                       | 80        |
| 7.2.2    | Non-proportional loading experiments . . . . .                     | 82        |
| 7.2.3    | Non-proportional loading test of the unit cell . . . . .           | 84        |
| <b>8</b> | <b>Conclusions and outlook</b>                                     | <b>87</b> |
| <b>A</b> | <b>Derivation of elasticity equations in engineering constants</b> | <b>91</b> |

|          |   |            |
|----------|---|------------|
| <b>B</b> | <b>Micrographs of the copper specimens</b>                      | <b>95</b>  |
| <b>C</b> | <b>Crystallographic planes and directions in copper crystal</b> | <b>99</b>  |
|          | <b>Bibliography</b>   | <b>101</b> |






---

## List of Figures

|     |   |    |
|-----|---|----|
| 1.1 | Examples of constructions, fractured due to creep . . . . .           | 2  |
| 1.2 | Examples of the creep fracture at different scales . . . . .          | 3  |
| 1.3 | Typical cracking of solder due to plastic and creep deformations . .  | 6  |
| 2.1 | Theoretical tests under single crystal copper . . . . .               | 11 |
| 2.2 | Crystallographic basis in Miller and vector notations . . . . .       | 12 |
| 2.3 | Arbitrary normal $m$ in crystallographic basis . . . . .              | 13 |
| 2.4 | Variation of the elastic modulus with crystallographic orientation .  | 15 |
| 2.5 | Creep strain rate comparison for different type of models . . . . .   | 29 |
| 2.6 | Creep strain rate variation in the material with the cubic symmetry   | 31 |
| 2.7 | Creep strain rate variation predicted by crystal plasticity model . . | 33 |
| 2.8 | Creep strain rate variation in the material with the cubic symmetry   | 34 |
| 3.1 | Grain boundary sliding in copper at 676 °C . . . . .                  | 36 |
| 3.2 | Schematic representation of grains bonding . . . . .                  | 38 |
| 4.1 | Schematic representation of a cavitated grain boundary . . . . .      | 46 |
| 4.2 | Elliptical hole axes with respect to the orthotropy axes . . . . .    | 49 |
| 5.1 | Geometrical representation of a polycrystal . . . . .                 | 55 |
| 5.2 | Grain boundary region with discrete material orientation . . . . .    | 55 |
| 5.3 | Creep curves scatter for 55 realizations of the unit cells . . . . .  | 59 |
| 5.4 | Creep curves scatter for 55 realizations of the unit cells . . . . .  | 60 |
| 5.5 | Creep strain for unit cells with different number of grains . . . . . | 60 |
| 5.6 | Creep strain for unit cell with different grain boundary thickness .  | 62 |

|     |   |    |
|-----|---|----|
| 6.1 | Experimental setup . . . . .  | 67 |
| 6.2 | Geometry of the specimen . . . . .  | 67 |
| 6.3 | Experimental creep curves of copper tested at 550 °C . . . . .            | 68 |
| 6.4 | Normalized minimum creep strain rate vs. normalized stress . . . . .      | 70 |
| 6.5 | Micrographs of the specimen in the initial state (magnification 200x)     | 71 |
| 6.6 | Micrographs of the specimen, tested at 30 MPa (magnification 200x)        | 71 |
| 6.7 | Micrographs of the specimen, tested at 10 MPa (magnification 200x)        | 72 |
| 7.1 | Averaged creep strain variation with the change of $\xi$ . . . . .        | 74 |
| 7.2 | Variation of the sliding and total strain in the unit cell with 80 grains | 76 |
| 7.3 | Equivalent stress variation with different creep properties . . . . .     | 77 |
| 7.4 | Creep curves of the non-proportional loading tests . . . . .              | 83 |
| 7.5 | Simulated creep curves for proportional and non-proportional tests        | 85 |
| 7.6 | Damage distribution within the cross section of the unit cell . . . . .   | 86 |
| B.1 | Micrographs of the specimen in the initial state (magnification 50x)      | 95 |
| B.2 | Micrographs of the specimen in the initial state (magnification 100x)     | 95 |
| B.3 | Micrographs of the specimen, tested at 30 MPa (magnification 50x)         | 96 |
| B.4 | Micrographs of the specimen, tested at 30 MPa (magnification 100x)        | 96 |
| B.5 | Micrographs of the specimen, tested at 10 MPa (magnification 500x)        | 96 |
| B.6 | Micrographs of the specimen, tested at 10 MPa (magnification 100x)        | 97 |



---

## List of Tables

|     |  |     |
|-----|--|-----|
| 5.1 | Prescribed features to the unit cell's materials . . . . . | 57  |
| 6.1 | Summarized data of the experimental creep tests . . . . .  | 69  |
| 7.1 | Material model parameters . . . . .                        | 77  |
| 7.2 | Scheme of the applied loading . . . . .                    | 85  |
| C.1 | First octahedral slip system . . . . .                     | 99  |
| C.2 | Second octahedral slip system . . . . .                    | 100 |
| C.3 | Cubic slip system . . . . .                                | 100 |



---

# Introduction and Motivation

## 1.1 Introduction

The description of mechanical material behavior is an important and challenging task for engineers worldwide. The mechanical behavior of one material can be described with the different rheological models whether elastic, plastic or viscous, depending on the operation conditions of the construction, such as applied load and ambient temperature. Another important factor influencing almost every material object and phenomena is time. In the creep process this factor plays the key role as well. So, if the structure operates under moderate constant load and high temperature  $T/T_m \sim 0.3 - 0.5$  [62, 89], where  $T_m$  is the melting temperature of the material, the strains develop with the time and they are called creep strains. In the literature it is common to determine the temperature level as a ratio to the melting temperature, the same notation is used in the current work.

In contrast to the creep at ambient temperature  $T/T_m \sim 0.1 - 0.3$  [62], the high-temperature creep is the most important for the engineering investigations due to the high order of the resultant deformations. In this case from the rheological point of view inelastic viscous strains should be considered. The phenomenological statement of the creep law is given through the description of the creep strain evolution with time in the dependence on the applied stress.

The well-known constructions undergoing creep are boilers and power plant components. The examples of such power plant components are: rotors, shells, steam chests and casings. Their lifetime is usually counted



**Figure 1.1** Examples of constructions, fractured due to creep: a) the blade failure due to many processes including creep cavitation (taken from <http://www.atslab.com/>); b) creep fracture of a superheater (taken from <http://www.surescreen.com/scientifics/>)

by many decades and the creep strains, exceeding the admissible limits are often the reason of accidents or failures. One important engineering task is to predict the time to rupture of such constructions. The examples of the components after creep fracture are illustrated in Fig. 1.1.

With the measurements of the specimen elongation over time the creep process can be described. For the phenomenological description the set of such uniaxial creep tests is needed. An example of the uniaxial creep tension specimen after fracture is illustrated in Fig. 1.2a). The plotted creep data is called the creep curve, where the evolution of the strain over time or the strain rate vs. strain are plotted. For both cases the typical creep curve shows three regions of the creep strain rate change. The first or primary creep stage is characterized by the decrease of the creep strain rate due to the hardening processes. The secondary or steady-state creep stage is observed when the creep strain rate decreases to some minimal value and does not change over time or with forthcoming deformation. Already during the steady-state creep stage the nucleation and growth of cavities on the grain boundaries of the material takes place. During the tertiary creep stage the interlinkage and the

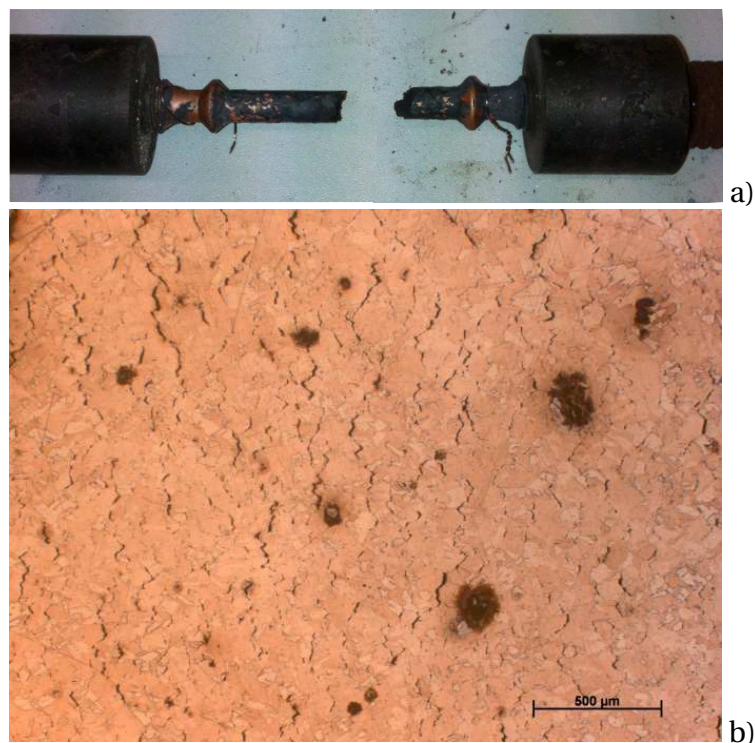


**Figure 1.2** Examples of the creep fracture at different scales: a) creep specimen after fracture; b) micrograph of the copper specimen, tested at 550 °C and 25 MPa within 2 hours

coalescence of cavities into cracks leads to the increase of the creep strain rate and the subsequent fracture. The polycrystal microstructure after creep fracture is illustrated in Fig. 1.2b).

For many engineering materials the steady-state creep stage lasts the major part of the life time, and due to this, the minimum creep strain rate can be used for the time to rupture determination. The expression, for the dependence between the time to rupture of the material and the secondary creep strain rate is well-known as a Monkman–Grant relationship [82] and is represented as following:

$$\dot{\epsilon}_{ss}^m t_r = k_{MG},$$

where  $m$  is a material parameter, usually equal to 1,  $k_{MG}$  is the Monkman–Grant constant,  $\dot{\epsilon}_{ss}$  is the steady-state creep strain rate and  $t_r$  is time to rupture. This expression shows good predictions of the lifetime for the constructions, working under uniaxial constant stress conditions, based only on one creep parameter. For the other loading cases the expression of time

to rupture has much more complicated form and requires to determine other quantities. The time to rupture prediction for the modern materials, working under complex loading conditions (variational loading, varying temperature, aggressive environment, etc.) is still open and actual task for the researchers.

## 1.2 Motivation

The aim of the current work is to contribute to understanding of the creep fracture on the micro- and macrolevels. The description of the material behavior during operation is mostly made with the phenomenological models of the different complexity, prescribed the loading conditions and material microstructure. The disadvantage of such approach is that creep processes are characterized by the physically non-motivated internal variables, which are served to describe the creep curves, but not the processes, taking place in the material. Despite the great amount of existing works, dedicated to the creep damage modeling on the micro scale, only few studies are related to the simulation of creep damage for polycrystalline aggregates.

The micromechanical mechanisms, preceding creep fracture are power law creep of the grain material, grain boundary sliding, contributing to the creep strain and locally leading to the cavities formation on the triple points, the cavity nucleation, growth and coalescence.

Besides the above mentioned advantages, the micromechanical approach leads to increasing of the model complexity. The assumption of the material homogeneity and isotropy, which one can imply for the macromaterial is not acceptable for the model with the length scale equal to grain size. On this level grains orientation and shape should be considered. Grain boundaries act as separate objects, from one hand constructing the grain deformation and leading in this way to the material hardening and from the other hand being the source of the cavitation, leading to the material softening. The source of the deformation in the crystalline material is the presence of the lattice defects, called dislocations. The dislocation structure is changing during the creep process and should be included in the model as well. For example, at high temperature the dislocation climb between the slip planes takes place due to diffusion processes. This process is still not reflected by the existing models and the assumption of the slip only by the crystallographic planes is taken. The direct modeling of the dislocations in crystalline material has limitation from the point of view of computational power. Therefore the current investigation has the aim to make the bridge between several main

mechanisms, taking place on microlevel and the behavior of the creep curve, corresponding to the macromaterial.

One of the possible model application is the simulation of material behavior under non-proportional loading, when the principal stresses rotation over time takes place. In real operating conditions the non-proportionality of loading is often detected. For example, in the case of power plant components due to start ups and shut downs. The detailed observation of the existing tests under non-proportional loading [86, 125] is presented in Chapter 6, but for the sake of consistency the main ensuing conclusions are shown here. Murakami and Ohno [86] discuss the results of creep tests of the tubular copper specimens under constant tension as well as the reversed torsion. The reversion of torsion at the same point of the test is performed in the way to cause the principal directions rotation on the angles 30, 60 and 80°. The principal stress rotation during test leads to the significant prolongation of the time to rupture, which increases with the increase of the rotation angle. The source of this phenomena is found to be on the level of grain boundaries. According to the observations of copper specimens microstructure after creep loading, the cavities are growing on the grain boundaries oriented perpendicularly to the maximum applied tensile stress. Thus, after the maximum principal stress rotation another unaffected grain boundaries are involved in the cavitation process. That grain boundaries, which are orthogonal to the primary oriented principal stress undergo less cavitation. By the significant principal stress rotation formerly cavitated grain boundaries can undergo compression which leads to the material renewal.

On the macro level the tertiary creep stage is usually described by introduction of the damage variable, which represents the material volume affected by cracks, cavities and other defects (see Sect. 7.2.1). The influence of the damage on the creep strain rate is usually accounted by integrating it into constitutive equations as an internal variable.

For an isotropic material under uniaxial tension state the damage variable can be represented through the scalar parameter, though, for the non-proportional loading case, where the damage growth is dependent on the varying with time direction of the principal stress, the damage variable should be represented through the tensor of certain range. Another way to describe the material damage under non-proportional loading is to introduce progress of microstructural form of damage (creep cavitation for copper). In this case the simulation becomes from the one point more complex due to the fact that the grains orientations, grain boundary sliding, subgrains formation and other micromechanical phenomena should be taken into account. From the

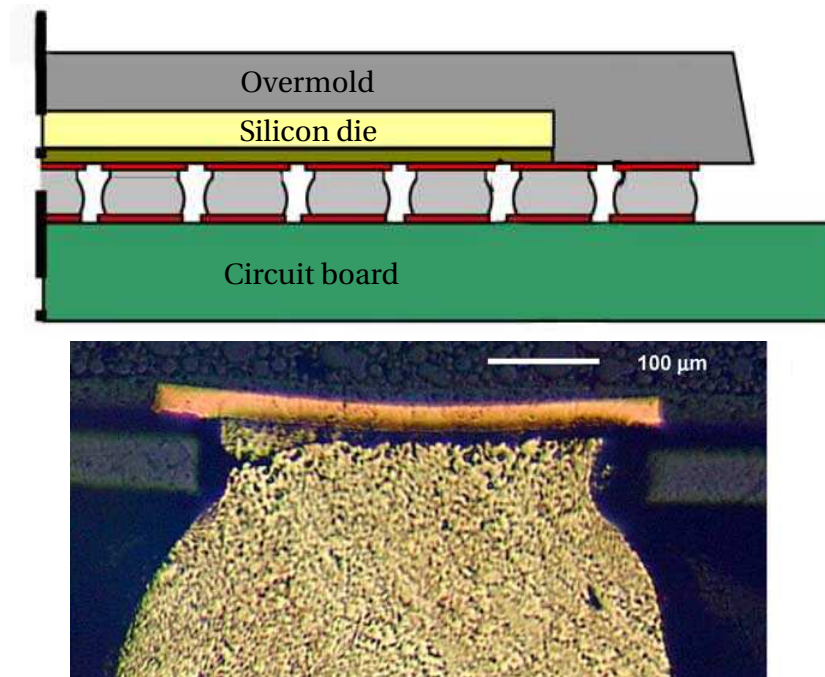


**Figure 1.3** Typical crack through solder joint interface due to plastic and creep deformations. Scheme of solder interconnection in an electronic assembly [124]

other side, such representation allows to introduce creep cavitation through the set of scalar parameters such as cavity radius, cavity spacing, area fraction of holes etc (see Sect. 4.1). Their representation directly on the level of grain boundaries automatically accounts the dependence on the grain boundary orientation to the applied stress.

The aim of the current work is to perform creep damage analysis on the microlevel in order to obtain anisotropic creep damage response on the mesolevel. The copper is chosen as the simulated material to compare the simulation results with the creep tests [86]. The unit cell concept is used to build the representative volume of microstructure. Various mechanisms are introduced for the different phases of the unit cell by means of the appropriate material models. The complexity of the model for each case is chosen from the considerations of efficiency, validity and the minimal numerical costs. Another motivation for the current research gives the necessity of creep fracture simulation of the microelectronic devices. Usually the lifetime of the microelectronic assemblies is limited by the life-time of the solders, connecting the details mechanically, thermally and electrically. Such assemblies are widely used in the modern automotive industry and can

undergo high temperatures due to electro power consumed, due to placement near engines or both. The level of temperatures, registered for such solders is near 175 °C. Their components have dimensions of several mm and even less [102]. The diameter of such solders can have dimensions less than one mm. With this the assumption of the material homogeneity is not acceptable and existing constitutive models of macromaterial are not applicable. Due to high operation temperature and essential mechanical loading the solder material undergo creep deformations. In Fig. 1.3 the fracture of the solder due to plastic and creep deformations is shown. The scheme of the electronic assembly shows the array of solders and the localization of the probable failure. The both motivations on the micro- and macrolevels denote the necessity of the simulation of the creep process from the micromechanical point of view.



---

## Constitutive modeling of a polycrystalline material

On the microlevel metals are composed of grains. In a small material point of a macrocontinuum the number of grains is huge and the distribution of their orientations is random. Therefore the polycrystalline material can be simulated as an isotropic one. But if the simulation on the level of grains is required, then it is necessary to consider its crystalline anisotropic nature. The crystalline structure is formed by periodical reiteration of a crystalline lattice of a certain type. The lattice type defines the type of material anisotropy. In pure phenomenological models [11, 76] constitutive equations for elastic and creep strains evolution are written for an anisotropic material. Furthermore material model parameters are identified from single crystal elastic and creep tests. Another phenomenological approach considers anisotropic material with crystallographical planes of preferential slip. These are planes of the maximum atomic density. Such models describing inelastic deformation of crystals are called crystal viscoplasticity models [6, 55, 100, 116]. Inelastic slip in crystalline materials mainly occurs due to the presence of line defects, which are known as dislocations. Scale dependent crystal viscoplasticity models [5, 38, 44, 45, 68, 138] describe inelastic deformation through the evolution of the dislocation density within the material. In the following section an overview on these main approaches for creep modeling of a polycrystalline material will be provided.

## 2.1 Elasticity

Within the phenomenological modeling of a strain one should account the fact that crystalline materials possess cubic symmetry type [130]. The constitutive equations for the linear viscoelastic model are derived in [11] for the material with cubic symmetry. The projection method is used to represent elasticity fourth rank tensor  $\mathbb{C}$  as followings:

$$\mathbb{C} = \lambda_1 \mathbb{P}_1 + \lambda_2 \mathbb{P}_2 + \lambda_3 \mathbb{P}_3,$$

where

$$\mathbb{P}_1 = \frac{1}{3} \mathbf{I} \otimes \mathbf{I},$$

$$\mathbb{P}_2 = \sum_{i=1}^3 (\mathbf{g}_i \otimes \mathbf{g}_i \otimes \mathbf{g}_i \otimes \mathbf{g}_i) - \mathbb{P}_1,$$

$$\mathbb{P}_3 = \mathbb{I} - \mathbb{P}_1 - \mathbb{P}_2,$$

$\mathbf{I}$  and  $\mathbb{I} = \frac{1}{2} [\mathbf{g}_p \otimes \mathbf{I} \otimes \mathbf{g}_p + \mathbf{g}_i \otimes \mathbf{g}_j \otimes \mathbf{g}_i \otimes \mathbf{g}_j]$  are the unit tensors of the second and fourth order respectively,  $\otimes$  denotes the dyadic product and  $\lambda_i$  are material properties,  $\mathbf{g}_i$  ( $i = 1, 2, 3$ ) are crystallographic axes. With  $\boldsymbol{\sigma} = \mathbb{C} \cdot \boldsymbol{\varepsilon}^{\text{el}}$  the constitutive relation between the stress and the elastic strain tensor for the case of cubic symmetry takes the form:

$$\begin{aligned} \boldsymbol{\sigma} = & \frac{1}{3} \lambda_1 \text{tr} \boldsymbol{\varepsilon}^{\text{el}} \mathbf{I} \\ & + \lambda_2 \left[ \varepsilon_{11}^{\text{el}} \left( \mathbf{g}_1 \otimes \mathbf{g}_1 - \frac{1}{3} \mathbf{I} \right) + \varepsilon_{22}^{\text{el}} \left( \mathbf{g}_2 \otimes \mathbf{g}_2 - \frac{1}{3} \mathbf{I} \right) + \varepsilon_{33}^{\text{el}} \left( \mathbf{g}_3 \otimes \mathbf{g}_3 - \frac{1}{3} \mathbf{I} \right) \right] \\ & + \frac{1}{2} \lambda_3 \left[ \gamma_{12}^{\text{el}} (\mathbf{g}_1 \otimes \mathbf{g}_2 + \mathbf{g}_2 \otimes \mathbf{g}_1) + \gamma_{13}^{\text{el}} (\mathbf{g}_1 \otimes \mathbf{g}_3 + \mathbf{g}_3 \otimes \mathbf{g}_1) \right. \\ & \left. + \gamma_{23}^{\text{el}} (\mathbf{g}_2 \otimes \mathbf{g}_3 + \mathbf{g}_3 \otimes \mathbf{g}_2) \right], \end{aligned} \quad (2.1)$$

where  $\boldsymbol{\sigma}$  is the stress tensor,  $\varepsilon_{ij}^{\text{el}} = \mathbf{g}_i \cdot \boldsymbol{\varepsilon}^{\text{el}} \cdot \mathbf{g}_j$  ( $i = j$ ) and  $\gamma_{ij}^{\text{el}} = 2 \mathbf{g}_i \cdot \boldsymbol{\varepsilon}^{\text{el}} \cdot \mathbf{g}_j$  ( $i \neq j$ ) are normal and shear components of the elastic strain tensor  $\boldsymbol{\varepsilon}^{\text{el}}$  correspondingly.

Equation (2.1) contains three elastic material parameters  $\lambda_1$ ,  $\lambda_2$ ,  $\lambda_3$ , the meaning of which can be explained by means of three theoretical tests presented in Fig. 2.1. The first test in Fig. 2.1a) corresponds to the hydrostatic compression of the cube by an applied spherical stress tensor  $\boldsymbol{\sigma} = -p_0 \mathbf{I}$ . Such a loading leads to vanishing of all stress tensor components except the spherical part, and from constitutive equation (2.1) one can determine  $\lambda_1$ . By the use of compression of two side faces and tension of the upper one the

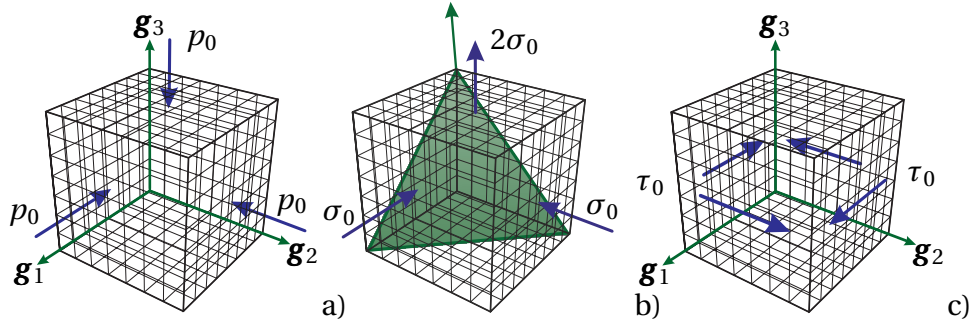


**Figure 2.1** Theoretical tests under single crystal copper: a) the hydrostatic compression test; b) the shear test on the octahedral plane; c) the shear test of the side faces.

shear on the octahedral planes of the crystal is generated. The octahedral plane is a special plane within the crystalline body of a preferable slip due to the higher atomic density [50]. There are eight equivalent octahedral planes in the single crystal. As an example, one possible octahedral plane is illustrated in Fig. 2.1b). In this case the applied stress tensor has the form  $\boldsymbol{\sigma} = \sigma_0(3\mathbf{g}_3 \otimes \mathbf{g}_3 - \mathbf{I})$ . From this test the coefficient  $\lambda_2$  can be determined. The third necessary test is one of the possible shear tests on the side faces of the cube, for example, with  $\boldsymbol{\sigma} = \tau_0(\mathbf{g}_1 \otimes \mathbf{g}_2 + \mathbf{g}_2 \otimes \mathbf{g}_1)$ . Such shear test is illustrated in Fig. 2.1c) and allows to determine the third coefficient  $\lambda_3$ .

The elastic parameters for the single crystal copper can be found in the literature. They may be obtained by measuring the wave velocity, propagating in the different directions of the single crystal. In the current work they are taken at the temperature  $\sim 0.5 T_m$  from [26]:

$$\lambda_1 = 374 \text{ GPa}, \quad \lambda_2 = 37 \text{ GPa}, \quad \lambda_3 = 125 \text{ GPa}. \quad (2.2)$$

The constitutive relation between stresses and elastic strains in Eq. (2.1) can be also derived through the engineering constants. In this case relations between the parameters  $\lambda_1$ ,  $\lambda_2$  and  $\lambda_3$  and the elastic modulus  $E$ , the Poisson's ratio  $\nu$  and the shear modulus  $G$ , determined from tensile and shear tests for the [001]-oriented single crystal copper have the form:

$$\lambda_1 = \frac{E}{1-2\nu}, \quad \lambda_2 = \frac{E}{1+\nu}, \quad \lambda_3 = 2G. \quad (2.3)$$

The derivation of the dependencies (2.3) is given in Appendix A.

The planes and directions in cubic crystals are usually determined with the Miller notation system, which is explained in many textbooks of the material

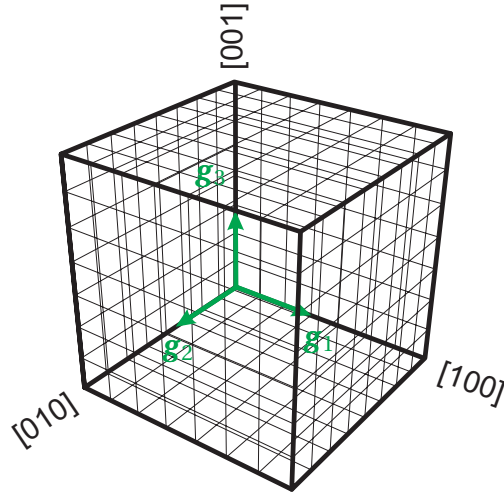


**Figure 2.2** Crystallographic basis in Miller and vector notations

science, for example in [121]. With the help of Miller indices (for example  $abc$ ), enclosed in brackets of the different type one can distinguish between the following objects, used in the current work:

- $[abc]$  – crystallographic direction;
- $\langle abc \rangle$  – crystallographic equivalent directions;
- $(abc)$  – crystallographic plane;
- $\{abc\}$  – planes of a family.

The correspondence between the crystallographic directions in the notations of Miller indices and the vectors is illustrated in Fig. 2.2.

For the special case of isotropy:

$$\lambda_2 = \lambda_3 \quad \text{and} \quad G = \frac{E}{2(1+\nu)}. \quad (2.4)$$

Involving Eqs (2.3) and (2.4) one can rewrite the elasticity law (2.1) as follows:

$$\begin{aligned} \boldsymbol{\sigma} = & \frac{1}{3} \frac{E}{1-2\nu} \text{tr} \boldsymbol{\varepsilon}^{\text{el}} \mathbf{I} \\ & + \frac{E}{1+\nu} \left[ \varepsilon_{11}^{\text{el}} \mathbf{g}_1 \otimes \mathbf{g}_1 + \varepsilon_{22}^{\text{el}} \mathbf{g}_2 \otimes \mathbf{g}_2 + \varepsilon_{33}^{\text{el}} \mathbf{g}_3 \otimes \mathbf{g}_3 \right. \\ & + \varepsilon_{12}^{\text{el}} (\mathbf{g}_1 \otimes \mathbf{g}_2 + \mathbf{g}_2 \otimes \mathbf{g}_1) + \varepsilon_{13}^{\text{el}} (\mathbf{g}_1 \otimes \mathbf{g}_3 + \mathbf{g}_3 \otimes \mathbf{g}_1) \\ & \left. + \varepsilon_{23}^{\text{el}} (\mathbf{g}_2 \otimes \mathbf{g}_3 + \mathbf{g}_3 \otimes \mathbf{g}_2) - \frac{1}{3} \mathbf{I} (\varepsilon_{11}^{\text{el}} + \varepsilon_{22}^{\text{el}} + \varepsilon_{33}^{\text{el}}) \right]. \end{aligned} \quad (2.5)$$

From (2.5) the elasticity law for the case of isotropy can be obtained:

$$\boldsymbol{\sigma} = \frac{E}{1+\nu} \boldsymbol{\varepsilon} + \frac{E\nu}{(1+\nu)(1-2\nu)} \text{tr} \boldsymbol{\varepsilon} \mathbf{I}. \quad (2.6)$$

## 2.2 Dependence of the elastic properties on the crystallographical orientation

In the previous subsection the dependence of the material model parameters on the engineering constants of the [001]-oriented single crystal copper is introduced. The task of the following subsection is to illustrate the dependence of the engineering constants on the crystallographic orientation.

The arbitrary oriented normal  $\mathbf{m}$  in the crystallographic basis  $\mathbf{g}_i$ ,  $i = 1 \dots 3$  is considered in Fig. 2.3. One can uniquely define the normal  $\mathbf{m}$  by its three projections on the crystallographic axes:

$$\begin{aligned} \mathbf{m} \cdot \mathbf{g}_1 &= \sin \alpha \cos \beta, \\ \mathbf{m} \cdot \mathbf{g}_2 &= \sin \alpha \sin \beta, \\ \mathbf{m} \cdot \mathbf{g}_3 &= \cos \alpha. \end{aligned} \quad (2.7)$$

With the stress tensor

$$\boldsymbol{\sigma} = \sigma_0 \mathbf{m} \otimes \mathbf{m} \quad (2.8)$$

the elastic strain in the direction  $\mathbf{m}$  can be derived from Eq. (A.1), using the

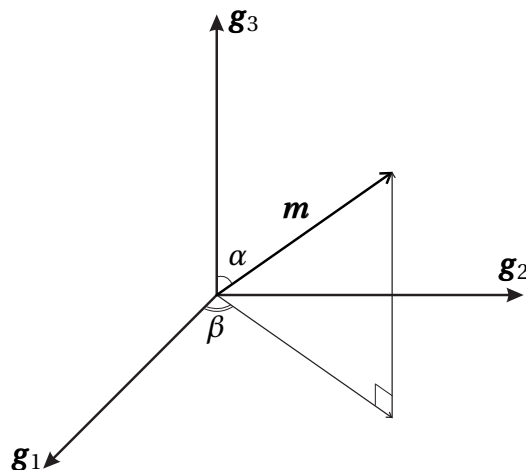


**Figure 2.3** Arbitrary normal  $\mathbf{m}$  in crystallographic basis

material parameters  $\lambda_1$ ,  $\lambda_2$  and  $\lambda_3$  as:

$$\begin{aligned}\varepsilon_{mm} &= \mathbf{m} \cdot \boldsymbol{\varepsilon} \cdot \mathbf{m} = \frac{1}{3} \frac{1}{\lambda_1} \text{tr} \boldsymbol{\sigma} \\ &+ \frac{1}{\lambda_2} \left\{ \sigma_{11} \left[ (\mathbf{m} \cdot \mathbf{g}_1)^2 - \frac{1}{3} \right] + \sigma_{22} \left[ (\mathbf{m} \cdot \mathbf{g}_2)^2 - \frac{1}{3} \right] + \sigma_{33} \left[ (\mathbf{m} \cdot \mathbf{g}_3)^2 - \frac{1}{3} \right] \right\} \\ &+ \frac{1}{\lambda_3} (2\tau_{12} \mathbf{m} \cdot \mathbf{g}_1 \otimes \mathbf{m} \cdot \mathbf{g}_2 + 2\tau_{13} \mathbf{m} \cdot \mathbf{g}_1 \otimes \mathbf{m} \cdot \mathbf{g}_3 + 2\tau_{23} \mathbf{m} \cdot \mathbf{g}_2 \otimes \mathbf{m} \cdot \mathbf{g}_3).\end{aligned}\quad (2.9)$$

The components of the stress tensor (2.8) in the crystallographic basis are determined in the following manner:

$$\begin{aligned}\sigma_{11} &= \mathbf{g}_1 \cdot \boldsymbol{\sigma} \cdot \mathbf{g}_1 = \sigma_0 (\mathbf{m} \cdot \mathbf{g}_1)^2, \\ \sigma_{22} &= \mathbf{g}_2 \cdot \boldsymbol{\sigma} \cdot \mathbf{g}_2 = \sigma_0 (\mathbf{m} \cdot \mathbf{g}_2)^2, \\ \sigma_{33} &= \mathbf{g}_3 \cdot \boldsymbol{\sigma} \cdot \mathbf{g}_3 = \sigma_0 (\mathbf{m} \cdot \mathbf{g}_3)^2, \\ \tau_{12} &= \mathbf{g}_1 \cdot \boldsymbol{\sigma} \cdot \mathbf{g}_2 = \sigma_0 (\mathbf{m} \cdot \mathbf{g}_1) (\mathbf{m} \cdot \mathbf{g}_2), \\ \tau_{23} &= \mathbf{g}_2 \cdot \boldsymbol{\sigma} \cdot \mathbf{g}_3 = \sigma_0 (\mathbf{m} \cdot \mathbf{g}_2) (\mathbf{m} \cdot \mathbf{g}_3), \\ \tau_{13} &= \mathbf{g}_1 \cdot \boldsymbol{\sigma} \cdot \mathbf{g}_3 = \sigma_0 (\mathbf{m} \cdot \mathbf{g}_1) (\mathbf{m} \cdot \mathbf{g}_3).\end{aligned}\quad (2.10)$$

With Eq. (2.10), Eq. (2.9) can be rewritten as follows:

$$\begin{aligned}\frac{\varepsilon_{mm}}{\sigma_0} &= \frac{1}{3} \frac{1}{\lambda_1} + \frac{1}{\lambda_2} \left\{ (\mathbf{m} \cdot \mathbf{g}_1)^2 \left[ (\mathbf{m} \cdot \mathbf{g}_1)^2 - \frac{1}{3} \right] + (\mathbf{m} \cdot \mathbf{g}_2)^2 \left[ (\mathbf{m} \cdot \mathbf{g}_2)^2 - \frac{1}{3} \right] \right. \\ &\quad \left. + (\mathbf{m} \cdot \mathbf{g}_3)^2 \left[ (\mathbf{m} \cdot \mathbf{g}_3)^2 - \frac{1}{3} \right] \right\} \\ &+ \frac{2}{\lambda_3} [(\mathbf{m} \cdot \mathbf{g}_1)^2 (\mathbf{m} \cdot \mathbf{g}_2)^2 + (\mathbf{m} \cdot \mathbf{g}_1)^2 (\mathbf{m} \cdot \mathbf{g}_3)^2 + (\mathbf{m} \cdot \mathbf{g}_2)^2 (\mathbf{m} \cdot \mathbf{g}_3)^2] \\ &= \frac{1}{E_\star(\alpha, \beta)},\end{aligned}\quad (2.11)$$

where  $E_\star(\alpha, \beta)$  is the equation of the surface, denoting the elastic modulus in the dependence on the crystallographical orientation.

The surface  $E_\star(\alpha, \beta)$  for the single crystal copper with the material model parameters (2.2) is presented in Fig. 2.4. The built surface qualitatively illustrates the variation of the elastic modulus of copper with crystallographic orientation. Figure 2.4 demonstrates that the crystal behaves stiffer in the direction, which coincides with the lattice orientation, namely  $\langle 001 \rangle$ . In contrast to this the crystal stiffness in the octahedral directions  $\langle 111 \rangle$  is minimal.

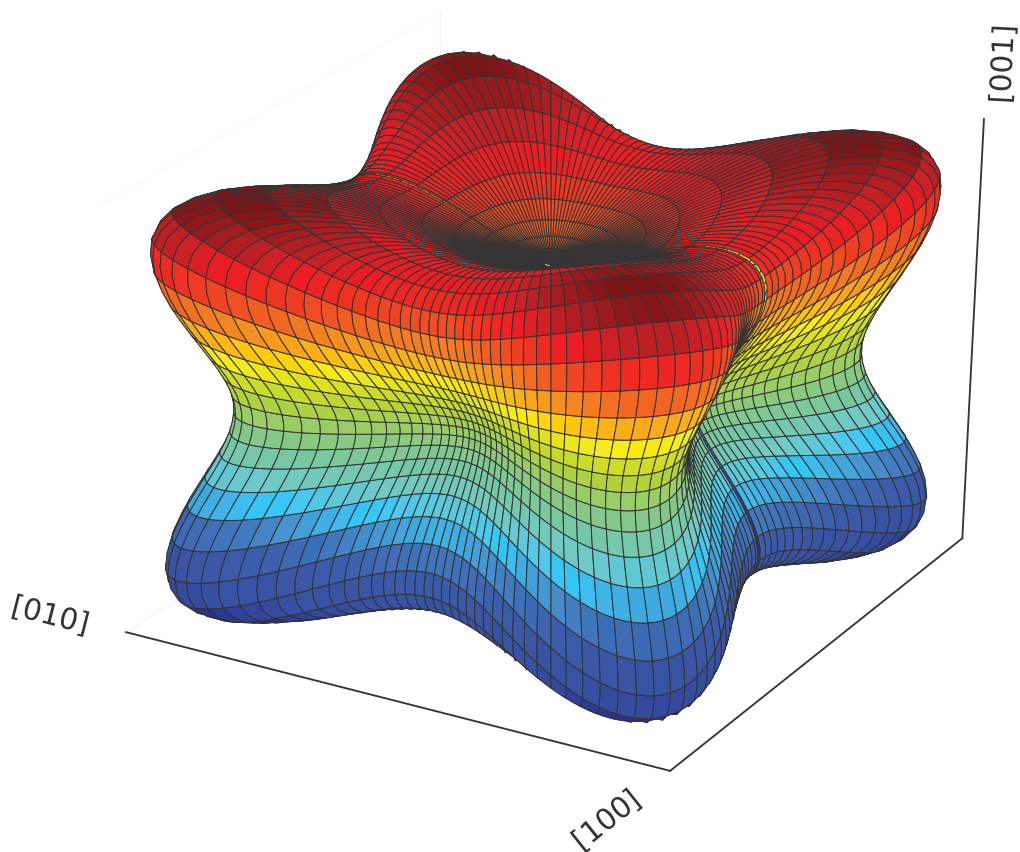


**Figure 2.4** Variation of the elastic modulus of copper with crystallographic orientation

## 2.3 Creep

### 2.3.1 General Remarks

Let us recall several assumptions usually made within the framework of the creep mechanics [14, 89, 98]. With the assumption of infinitesimal strains it is possible to disregard the difference between the true stresses and strains and the engineering stresses and strains. According to the continuum mechanics there are no differences between the Eulerian and the Lagrangian approaches within the material description. Creep equations in the geometrical non-linear case (finite strains) are discussed in the monograph [16], for example. Finite strain equations based on rheological models are presented in the monographs [32, 67, 106]. The linearized equations of continuum creep mechanics can be used in the majority of engineering applications because structures are usually designed such that

the displacements and strains arising as a consequence of the applied loading do not exceed the prescribed small values. Within the continuum micromechanics geometrical nonlinearities cannot be disregarded in general. Indeed, finite local strains can be usually observed within the scale of grains and grain boundaries, in particular within the localized shear band zones. In this work fracture modes related to localized deformation are not analyzed. The attention here is placed on the grain boundary cavitation. This damage mode is usually observed for moderate stress levels at high temperature. For this regime the deformation within the grains is usually not essential such that the linearized theory can be applied as a reasonable approximation.

The next assumption is related to the classical continuum mechanics. The equations of motion within the continuum mechanics include the balance of momentum and the balance of angular momentum, e.g. [36]. These equations introduce the stress and the moment stress tensors. Polar materials are those which are characterized by constitutive equations with respect to both tensors (in general, they are non-symmetric). In addition, the rotation degrees of freedom, i.e. the rotation tensor and the angular velocity, are introduced as independent quantities. Models of polar continua found application to granular or porous materials [31, 35, 84], fiber suspensions [4, 37], or other media with changing microstructure. A Cosserat-type model for crystal plasticity is presented in [40].

Creep deformation is accompanied by various microstructural changes having different influences on the strain rate. The current state of the material microstructure is determined by the entire previous history of the creep process. It can be characterized by a set of additional field variables termed as internal or hidden state variables.

Hardening processes are usually associated with interaction of moving dislocations with obstacles (particles, grain boundaries, dislocation forest etc.) and with the non-uniformity of inelastic deformation inside individual grains (layered structure of slip) and in polycrystals (different deformation in different grains).

Processes associated with hardening within the grains will be disregarded in this work, for the sake of simplicity. Hardening variables and hardening evolution equations are presented in [30, 39, 40, 90, 91]. Models with gradient effects of hardening and inelastic deformation inside grains are discussed in [9, 45, 123] among others.

Two approaches to derive creep constitutive equations will be discussed in this work. The first one is based on the creep potential hypothesis and the flow rule. Within the second approach the creep rate tensor is assumed to

be the sum of contributions from slip systems in a cubic crystal. Both the approaches will be compared based on the simulation of a uni-axial creep for different crystallographic directions.

### 2.3.2 Constitutive Equations Based on Creep Potential

The associated flow rule has the origin in the engineering theory of plasticity. The basic assumptions of this theory are:

- The existence of a yield condition (creep condition, see [13], for example) expressed by the equation  $F(\boldsymbol{\sigma}) = 0$ , where  $F$  is a scalar valued function. In the general case one can presume that  $F$  depends not only on the stress tensor but also on the internal state variables and the temperature [78, 109], i.e. the yield condition has a form:

$$F(\boldsymbol{\sigma}, H_i, \omega_j, T) = 0, \quad i = 1, \dots, n, \quad j = 1, \dots, m. \quad (2.12)$$

- The existence of a flow potential as a function of the stress tensor  $\Phi(\boldsymbol{\sigma})$ .

The flow rule (sometimes called the normality rule) is the following assumption for the inelastic strain rate tensor

$$\dot{\boldsymbol{\epsilon}}^{\text{in}} = \dot{\eta} \frac{\partial \Phi}{\partial \boldsymbol{\sigma}}, \quad (2.13)$$

where  $\dot{\eta}$  is a scalar factor. In the special case that the flow potential coincides with the yield function i.e.  $\Phi = F$ , Eq. (2.13) represents the associated flow rule. With respect to the variation of the stress tensor  $\delta \boldsymbol{\sigma}$  one distinguishes between the cases of elastic state, unloading from an elastic-plastic state, neutral loading and loading, i.e.

$$\left\{ \begin{array}{ll} F(\boldsymbol{\sigma}) < 0, & \text{elastic state} \\ F(\boldsymbol{\sigma}) = 0, \text{ and } \delta F = \delta \boldsymbol{\sigma} \cdot \frac{\partial F}{\partial \boldsymbol{\sigma}} < 0 & \text{unloading} \\ F(\boldsymbol{\sigma}) = 0, \text{ and } \delta F = \delta \boldsymbol{\sigma} \cdot \frac{\partial F}{\partial \boldsymbol{\sigma}} = 0 & \text{neutral loading} \\ F(\boldsymbol{\sigma}) = 0, \text{ and } \delta F = \delta \boldsymbol{\sigma} \cdot \frac{\partial F}{\partial \boldsymbol{\sigma}} > 0 & \text{loading} \end{array} \right.$$

For work hardening materials  $\dot{\eta} > 0$  is set in the case of loading/neutral loading, otherwise  $\dot{\eta} = 0$ , see e.g. [77]. Further details of the flow theory as well as different arguments leading to (2.13) can be found in textbooks on theory of plasticity, e.g. [51, 57, 61, 63, 77, 79, 120].

Within the creep mechanics the flow theory is usually applied without the concept of the yield stress or yield condition. This is motivated by the fact that creep is a thermally activated process and the material starts to creep even under low and moderate stresses lying below the yield limit. In monographs [13, 14, 77, 78, 107] the flow rule is applied as follows:

$$\dot{\boldsymbol{\epsilon}}^{\text{cr}} = \dot{\eta} \frac{\partial \Phi}{\partial \boldsymbol{\sigma}}, \quad \dot{\eta} > 0. \quad (2.14)$$

Equation (2.14) states the “normality” of the creep rate tensor to the surfaces  $\Phi(\boldsymbol{\sigma}) = \text{const}$ . The scalar factor  $\dot{\eta}$  is determined according to the hypothesis of the equivalence of the dissipation power [2, 14]. The dissipation power is defined by  $P = \dot{\boldsymbol{\epsilon}}^{\text{cr}} \cdot \boldsymbol{\sigma}$ . It is assumed that  $P = \dot{\epsilon}_{\text{eq}}^{\text{cr}} \sigma_{\text{eq}}$ , where  $\dot{\epsilon}_{\text{eq}}^{\text{cr}}$  is an equivalent creep rate and  $\sigma_{\text{eq}}$  is an equivalent stress. The equivalent measures of stress and creep rate are convenient to compare experimental data under different stress states. From the above hypothesis follows

$$\dot{\eta} = \frac{P}{\frac{\partial \Phi}{\partial \boldsymbol{\sigma}} \cdot \boldsymbol{\sigma}} = \frac{\dot{\epsilon}_{\text{eq}}^{\text{cr}} \sigma_{\text{eq}}}{\frac{\partial \Phi}{\partial \boldsymbol{\sigma}} \cdot \boldsymbol{\sigma}}. \quad (2.15)$$

The equivalent creep rate is defined as a function of the equivalent stress according to the experimental data for uni-axial creep as well as creep mechanisms operating for the given stress range. An example is the power law stress function

$$\dot{\epsilon}_{\text{eq}}^{\text{cr}}(\sigma_{\text{eq}}) = a \sigma_{\text{eq}}^n. \quad (2.16)$$

Another form of the flow rule without the yield condition has been proposed by Odqvist, [97, 99]. The steady-state creep theory by Odqvist, see [97], p.21 is based on the variational equation  $\delta W = \delta \boldsymbol{\sigma} \cdot \dot{\boldsymbol{\epsilon}}^{\text{cr}}$  leading to the flow rule

$$\dot{\boldsymbol{\epsilon}}^{\text{cr}} = \frac{\partial W}{\partial \boldsymbol{\sigma}}, \quad (2.17)$$

where the scalar valued function  $W(\boldsymbol{\sigma})$  plays the role of the creep potential. Taking into account that  $W(\boldsymbol{\sigma}) = W(\sigma_{\text{eq}}(\boldsymbol{\sigma}))$  the flow rule (2.17) yields

$$\dot{\boldsymbol{\epsilon}}^{\text{cr}} = \frac{\partial W}{\partial \sigma_{\text{eq}}} \frac{\partial \sigma_{\text{eq}}}{\partial \boldsymbol{\sigma}} = \dot{\epsilon}_{\text{eq}}^{\text{cr}} \frac{\partial \sigma_{\text{eq}}}{\partial \boldsymbol{\sigma}}, \quad \dot{\epsilon}_{\text{eq}}^{\text{cr}} \equiv \frac{\partial W}{\partial \sigma_{\text{eq}}}. \quad (2.18)$$

The creep potential  $W(\sigma_{\text{eq}})$  is defined according to experimental data of creep under uni-axial stress state for the given stress range. An example is the Norton-Bailey-Odqvist creep potential

$$W = \frac{\sigma_0}{n+1} \left( \frac{\sigma_{\text{vM}}}{\sigma_0} \right)^{n+1}, \quad (2.19)$$

widely used for the description of steady-state creep of metals and alloys. In (2.19)  $\sigma_0$  and  $n$  are material constants and  $\sigma_{\text{VM}}$  is the von Mises equivalent stress. Below we discuss various restrictions on the potentials, e.g. the symmetries of the creep behavior and the inelastic incompressibility.

The flow rules (2.14) and (2.17) lead to the same creep constitutive equation if the equivalent stress satisfies the following partial differential equation [89]

$$\frac{\partial \sigma_{\text{eq}}}{\partial \boldsymbol{\sigma}} \cdot \boldsymbol{\sigma} = \sigma_{\text{eq}}. \quad (2.20)$$

The potential formulations originate from the works of Richard von Mises, where the existence of variational principles is assumed in analogy to those known from the theory of elasticity (the principle of the minimum of the complementary elastic energy, for example) [131]. Secondary or stationary creep is for many applications the most important approximation. After a relatively short transient period the material creeps in such a manner that an approximate equilibrium between hardening and recovery processes can be assumed. This equilibrium exists for a certain time and the long term behavior of a structure can be analyzed assuming stationary creep processes.

The classical equation for the isotropic steady-state flow is derived as follows. Under the assumption of the isotropic creep, the creep potential must satisfy the following restriction

$$W(\mathbf{Q} \cdot \boldsymbol{\sigma} \cdot \mathbf{Q}^T) = W(\boldsymbol{\sigma}) \quad (2.21)$$

for any symmetry transformation  $\mathbf{Q}$ ,  $\mathbf{Q} \cdot \mathbf{Q}^T = \mathbf{I}$ ,  $\det \mathbf{Q} = \pm 1$ . From (2.21) it follows that the potential depends only on the three scalar invariants of the stress tensor. With the principal invariants

$$\begin{aligned} J_1(\boldsymbol{\sigma}) &= \text{tr } \boldsymbol{\sigma}, & J_2(\boldsymbol{\sigma}) &= \frac{1}{2}[(\text{tr } \boldsymbol{\sigma})^2 - \text{tr } \boldsymbol{\sigma}^2], \\ J_3(\boldsymbol{\sigma}) &= \det \boldsymbol{\sigma} = \frac{1}{6}(\text{tr } \boldsymbol{\sigma})^3 - \frac{1}{2}\text{tr } \boldsymbol{\sigma} \text{tr } \boldsymbol{\sigma}^2 + \frac{1}{3}\text{tr } \boldsymbol{\sigma}^3 \end{aligned} \quad (2.22)$$

the potential takes the form

$$W(\boldsymbol{\sigma}) = W(J_1, J_2, J_3).$$

The stress tensor is decomposed as follows

$$\boldsymbol{\sigma} = \sigma_m \mathbf{I} + \mathbf{s}, \quad \text{tr } \mathbf{s} = 0 \quad \Rightarrow \quad \sigma_m = \frac{1}{3} \text{tr } \boldsymbol{\sigma},$$

where  $\mathbf{s}$  is the stress deviator and  $\sigma_m$  is the mean (hydrostatic) stress. With the principal invariants of the stress deviator

$$J_{2D} = -\frac{1}{2} \text{tr } \mathbf{s}^2 = -\frac{1}{2} \mathbf{s} \cdot \mathbf{s}, \quad J_{3D} = \frac{1}{3} \text{tr } \mathbf{s}^3 = \frac{1}{3} (\mathbf{s} \cdot \mathbf{s}) \cdot \mathbf{s}$$

the potential takes the form

$$W = W(J_1, J_{2D}, J_{3D}).$$

From the flow rule (2.17) it follows

$$\dot{\boldsymbol{\epsilon}}^{\text{cr}} = \frac{\partial W}{\partial J_1} \mathbf{I} - \frac{\partial W}{\partial J_{2D}} \mathbf{s} + \frac{\partial W}{\partial J_{3D}} \left( \mathbf{s}^2 - \frac{1}{3} \text{tr} \mathbf{s}^2 \mathbf{I} \right). \quad (2.23)$$

In the classical creep theory it is assumed that the inelastic deformation does not produce a significant change in volume. The spherical part of the creep rate tensor is neglected, i.e.  $\text{tr} \dot{\boldsymbol{\epsilon}}^{\text{cr}} = 0$ . Setting the trace of (2.23) to zero results in

$$\text{tr} \dot{\boldsymbol{\epsilon}}^{\text{cr}} = 3 \frac{\partial W}{\partial J_1} = 0 \quad \Rightarrow \quad W = W(J_{2D}, J_{3D}).$$

It follows that the creep behavior is not sensitive to the hydrostatic stress state  $\boldsymbol{\sigma} = -p\mathbf{I}$ , where  $p > 0$  is the hydrostatic pressure. The creep equation (2.23) can be formulated as

$$\dot{\boldsymbol{\epsilon}}^{\text{cr}} = -\frac{\partial W}{\partial J_{2D}} \mathbf{s} + \frac{\partial W}{\partial J_{3D}} \left( \mathbf{s}^2 - \frac{1}{3} \text{tr} \mathbf{s}^2 \mathbf{I} \right). \quad (2.24)$$

The last term in the right-hand side of (2.24) is non-linear with respect to the stress deviator  $\mathbf{s}$ . Equations of this type are called tensorial non-linear equations, e.g. [8, 14, 78, 109] as several non-linear (higher-order) effects can be considered. For example, the torsion would lead to elongation creep rate is the square of the stress deviator is considered, e. g. [89]. Within the engineering creep mechanics such effects are usually neglected and with

$$W = W(J_{2D})$$

is the classical von Mises type potential [131]. In applications it is convenient to introduce the equivalent stress to compare the creep behavior under different stress states including the uni-axial tension. The von Mises equivalent stress is defined as follows

$$\sigma_{\text{vM}} = \sqrt{\frac{3}{2} \mathbf{s} \cdot \mathbf{s}} = \sqrt{-3J_{2D}}. \quad (2.25)$$

With  $W = W(\sigma_{\text{vM}}(\boldsymbol{\sigma}))$  the flow rule (2.17) results in

$$\dot{\boldsymbol{\epsilon}}^{\text{cr}} = \frac{\partial W(\sigma_{\text{vM}})}{\partial \sigma_{\text{vM}}} \frac{\partial \sigma_{\text{vM}}}{\partial \boldsymbol{\sigma}} = \frac{\partial W(\sigma_{\text{vM}})}{\partial \sigma_{\text{vM}}} \frac{3}{2} \frac{\mathbf{s}}{\sigma_{\text{vM}}}. \quad (2.26)$$

The second invariant of  $\dot{\boldsymbol{\epsilon}}^{\text{cr}}$  can be calculated as follows

$$\dot{\boldsymbol{\epsilon}}^{\text{cr}} \cdot \dot{\boldsymbol{\epsilon}}^{\text{cr}} = \frac{3}{2} \left[ \frac{\partial W(\sigma_{\text{vM}})}{\partial \sigma_{\text{vM}}} \right]^2.$$

Introducing the notation  $\dot{\epsilon}_{\text{vM}}^2 = \frac{2}{3}\dot{\epsilon}^{\text{cr}} \cdot \dot{\epsilon}^{\text{cr}}$  and taking into account that

$$P = \frac{\partial W(\sigma_{\text{vM}})}{\partial \sigma_{\text{vM}}} \sigma_{\text{vM}} \geq 0$$

one can write

$$\dot{\epsilon}^{\text{cr}} = \frac{3}{2} \dot{\epsilon}_{\text{vM}} \frac{\mathbf{s}}{\sigma_{\text{vM}}}, \quad \dot{\epsilon}_{\text{vM}} = \frac{\partial W(\sigma_{\text{vM}})}{\partial \sigma_{\text{vM}}}. \quad (2.27)$$

With the power law type creep potential

$$\dot{\epsilon}^{\text{cr}} = \frac{3}{2} a \sigma_{\text{vM}}^{n-1} \mathbf{s}, \quad (2.28)$$

where  $a$  and  $n$  are material parameters. The constitutive equation of steady-state creep (2.27) was proposed by Odqvist [99]. Experimental verifications of this equation can be found, for example, in [122] for steel 45, in [94] for titanium alloy Ti-6Al-4V and in [105] for alloys Al-Si, Fe-Co-V and XC 48. This model is widely used in estimations of steady-state creep in structures, e.g. [19, 21, 89, 99, 107, 109].

For anisotropic materials this theory is extended as follows. The creep potential is assumed to be an isotropic function of the stress tensor and a system of direction tensors associated with the orientation of the materials microstructure. For example, for the point group  $O_h$  (the symmetry group of the FCC lattice) the creep potential should be formulated as an isotropic function of the following two arguments

$$W = W(\boldsymbol{\sigma}, \mathbb{O}), \quad \mathbb{O} = \sum_{i=1}^3 \mathbf{g}_i \otimes \mathbf{g}_i \otimes \mathbf{g}_i \otimes \mathbf{g}_i, \quad (2.29)$$

where the fourth-rank tensor  $\mathbb{O}$  is called the structure tensor, e.g. [17]. With the theory of isotropic scalar-valued tensor functions it is possible to derive a system of independent arguments of  $W$  corresponding to the given symmetry group, e.g. [89]. Here we limit ourselves to the quadratic form of the creep potential. The most general quadratic form can be formulated as follows

$$\sigma_{\text{eq}}^2 = \frac{3}{2} \boldsymbol{\sigma} \cdot \mathbb{B} \cdot \boldsymbol{\sigma}, \quad (2.30)$$

where  $\sigma_{\text{eq}}$  is the equivalent stress. The fourth rank tensor  $\mathbb{B}$  contains the material parameters and has the same structure as the elasticity or the compliance tensor.

The flow rule (2.18) provides the following generalized anisotropic creep equation

$$\dot{\epsilon}^{\text{cr}} = \frac{3}{2} \frac{\dot{\epsilon}_{\text{eq}}^{\text{cr}}}{\sigma_{\text{eq}}} \mathbb{B} \cdot \boldsymbol{\sigma}, \quad \dot{\epsilon}_{\text{eq}}^{\text{cr}} \equiv \frac{\partial W}{\partial \sigma_{\text{eq}}}. \quad (2.31)$$

For materials with the cubic symmetry the tensor  $\mathbb{B}$  has the same structure as the tensor  $\mathbb{C}$ , that is

$$\mathbb{B} = \alpha_1 \mathbb{P}_1 + \alpha_2 \mathbb{P}_2 + \alpha_3 \mathbb{P}_3, \quad (2.32)$$

where  $\alpha_i$  are material parameters. Inserting Eq. (2.32) into Eq. (2.31) we obtain

$$\dot{\boldsymbol{\epsilon}}^{\text{cr}} = \frac{3}{2} \frac{\dot{\epsilon}_{\text{eq}}^{\text{cr}}}{\sigma_{\text{eq}}} \left( \sum_{i=1}^3 \alpha_i \mathbb{P}_i \right) \cdot \boldsymbol{\sigma}. \quad (2.33)$$

With  $\text{tr } \dot{\boldsymbol{\epsilon}}^{\text{cr}} = 0$  it follows that  $\alpha_1 = 0$  and (2.33) simplifies to

$$\dot{\boldsymbol{\epsilon}}^{\text{cr}} = \frac{3}{2} \frac{\dot{\epsilon}_{\text{eq}}^{\text{cr}}}{\sigma_{\text{eq}}} \left( \sum_{i=1}^2 \alpha_i \mathbb{P}_i \right) \cdot \boldsymbol{\sigma}, \quad \sigma_{\text{eq}}^2 = \frac{3}{2} \boldsymbol{\sigma} \cdot \left( \sum_{i=1}^2 \alpha_i \mathbb{P}_i \right) \cdot \boldsymbol{\sigma}. \quad (2.34)$$

In (2.34) assuming the power law creep and with  $\xi = \alpha_3/\alpha_2$ , Eqs (2.34) can also be given as follows

$$\dot{\boldsymbol{\epsilon}}^{\text{cr}} = \frac{3}{2} a \alpha_1 \sigma_{\text{eq}}^n (\mathbb{P}_1 + \xi \mathbb{P}_2) \cdot \boldsymbol{\sigma}, \quad \sigma_{\text{eq}}^2 = \frac{3}{2} \alpha_1 \boldsymbol{\sigma} \cdot (\mathbb{P}_1 + \xi \mathbb{P}_2) \cdot \boldsymbol{\sigma}, \quad (2.35)$$

where  $a$  and  $n$  are material parameters. The parameter  $\alpha_1$  can be selected arbitrarily. Below we set  $\alpha_1 = 1$ . One may verify that for  $\xi = 1$  Eq. (2.31) provides the classical isotropic creep constitutive equation (2.28). Equation (2.35) can also be written as follows

$$\begin{aligned} \dot{\boldsymbol{\epsilon}}^{\text{c}} = \frac{3}{2} a \sigma_{\text{eq}}^{n-1} & \left\{ \sigma_{11} \left( \mathbf{g}_1 \otimes \mathbf{g}_1 - \frac{1}{3} \mathbf{I} \right) + \sigma_{22} \left( \mathbf{g}_2 \otimes \mathbf{g}_2 - \frac{1}{3} \mathbf{I} \right) + \sigma_{33} \left( \mathbf{g}_3 \otimes \mathbf{g}_3 - \frac{1}{3} \mathbf{I} \right) \right. \\ & \left. + \xi \left[ \tau_{12} (\mathbf{g}_1 \otimes \mathbf{g}_2 + \mathbf{g}_2 \otimes \mathbf{g}_1) + \tau_{13} (\mathbf{g}_1 \otimes \mathbf{g}_3 + \mathbf{g}_3 \otimes \mathbf{g}_1) + \tau_{23} (\mathbf{g}_2 \otimes \mathbf{g}_3 + \mathbf{g}_3 \otimes \mathbf{g}_2) \right] \right\}, \end{aligned} \quad (2.36)$$

where

$$\sigma_{\text{eq}} = \sqrt{\frac{1}{2} \left[ (\sigma_{11} - \sigma_{22})^2 + (\sigma_{11} - \sigma_{33})^2 + (\sigma_{22} - \sigma_{33})^2 + 6\xi (\tau_{12}^2 + \tau_{23}^2 + \tau_{13}^2) \right]}. \quad (2.37)$$

### 2.3.3 Identification of creep parameters for the model based on potential

To complete modeling of the crystalline material parameters should be identified. In the current work model-based material is pure copper at the level of single crystal. For the elastic deformation region material parameters are reported in the literature as it is mentioned in Sect. 2.1.

For the inelastic region material model parameters  $a$ ,  $\xi$  and  $n$  should be determined from the creep tests under single crystal copper. For the

polycrystalline copper the power law exponent  $n$  is usually determined from the curve, showing dependence of minimum strain rate on stress at one temperature. The procedure is well known and in details described in many textbooks, for instance, in the textbook of Naumenko and Altenbach [89]. In this case tensile creep curves in a wide stress range are required.

Copper is one of the most popular materials used in academical research for the simulation. That is why many experimental data are reported in the literature starting from the middle of the last century. Orlova and Kucharova [104] performed compression tests of the double-notched single crystal specimen in order to realize shear strain on a range of crystal planes. The tests were performed at temperatures of 773 and 783 K and applied compression stress ranged between 5 and 20 MPa. In the work detailed creep curves are presented. Strain rate vs. strain curves of [001]-oriented single crystal specimen under constant shear conditions are reported in the paper of Borbely et al. [18]. The specimens were tested at 293 and 527 K and applied shear stress 60 and 54.7 MPa, correspondingly. In the following tests minimum creep strain rate was reached. A series of results from tensile tests under single crystal copper is published within the last decades, see [43, 103, 137] among others.

For the accurate and reliable material model parameters identification the set of the creep curves in [100] and [111] crystallographic directions at one temperature is required. Any of the tests mentioned above contain such data. So, in the current work creep data, obtained in a private communication is used, which is recently published in [132]. One of the authors performed tensile creep tests under [100] and [111]-oriented single crystal copper at 550 °C and of 10, 15 and 20 MPa of applied stress.

Power exponents for single crystal copper were determined from these tests for the creep curves of the crystals at [001] and [111] orientations at 2 and 3 stress levels, respectively. The power law exponents for the current modeling were taken as the average between 2 curves. These values are equal 9.25. The scattering from the average value is around 15%.

To determine the rest of the parameters tensile creep tests of [001]- and [111]-oriented single crystal are needed. The creep strain tensor expression of the [001]- oriented material under applied stress  $\sigma_0$  reduces from Eq. (2.36) to the following form:

$$\dot{\epsilon}_{[001]}^{CF} = a\sigma_0^n.$$

From this test the material parameter  $a$  can be determined as

$$a = \frac{\dot{\epsilon}_{[001]}^{\text{cr}}}{\sigma_0^n}.$$

The parameter  $\xi$  can be determined from the tensile test of [111]-oriented crystal. The resulting expression for the creep strain rate has the form:

$$\dot{\epsilon}_{[111]}^{\text{cr}} = a\sigma_0^n \xi^{\frac{n+1}{2}}.$$

From the above formula the expression for  $\xi$  is obtained as:

$$\xi = \left( \frac{\dot{\epsilon}_{[111]}^{\text{cr}}}{a\sigma_0^n} \right)^{\frac{2}{n+1}}, \quad (2.38)$$

where  $\dot{\epsilon}_{[001]}^{\text{cr}}$  and  $\dot{\epsilon}_{[111]}^{\text{cr}}$  are creep strains taken from the correspondent experimental data. Model material parameters determined for single crystal copper based on the experimental data of O. Frederik are:

$$a = 1.96 \cdot 10^{-15} \frac{(\text{MPa})^{-n}}{\text{h}}, \quad n = 9.4, \quad \xi = 0.026.$$

### 2.3.4 Crystallographic approach

In the current work polycrystalline materials are described by the model, based on the creep potential. Though for the sake of completeness a short overview on a crystallographic modeling is presented.

Power plant components design is an important branch of the engineering simulations during the last 50 years. Widely used materials for the power plants blades are Ni-based single crystal alloys. Their microstructure corresponds to the structure of the material within one grain. That is why research of the Ni-based alloys led to the progress in the crystallographic modeling. The crystallographic approach is based on the fact that the energy, which is necessary for the atom slip in the crystal lattice is not the same for every direction and there are plains of preferential slip. It is well known from the literature for instance Smith [121] that the lattice of certain type has its own slip systems. In FCC crystal there are 4 independent slip planes with 3 slip directions within each plain, what results in 12 slip systems. However, experiments show that it is possible to activate other slip systems with the higher critical resolved shear stress value during creep [117]. Usually these are the cubic system and non-classical directions within the octahedral plains. Thus, slip will occur on the active planes due to presence of dislocations in

the single crystal material. For the slip system activation it is necessary that applied resolved shear stress acting on the slip plane exceed a critical value. This condition of slip is well known as Schmid's law. The value of critical resolved shear stress can be obtained experimentally. Resolved shear stress can be recalculated by multiplying magnitude of the applied stress on the orientational cosines of the normal to the slip plane and slip direction [115]. Contribution to the overall deformation of the single crystal gives the sum of slips from all active slip systems.

For example, the crystal creep theory proposed in [100] describes the secondary creep stage with the usage of the power law. As operating during creep  $\{111\}\langle 110\rangle$  octahedral,  $\{111\}\langle 112\rangle$  octahedral and  $\{100\}\langle 110\rangle$  cubic slip-systems were considered. Nevertheless the microstructure of a pure crystalline material differs from the microstructure of single crystal superalloys, for example, by the presence in the last one so called  $\gamma$  or  $\gamma'$  phases, which impede dislocation motion and consequently lead to the strengthening during creep. Thus, advanced constitutive models, taking into account this phenomenon [116], are not sufficient to describe the pure single crystal material.

Hutchinson [55] describes the creep of FCC and ionic polycrystals. Constitutive equations for the shear rate on every slip system are based on power law creep. In addition, the way of calculation of average strain and stress fields is proposed. Based on the minimum principle for the strain rates proposed in [53] the upper bounds for the average strain in polycrystal are estimated. As a result, a self-consistent theory for the secondary creep is proposed, evaluating overall polycrystal deformation based on the single slip within the individual grain.

More enhanced crystal plasticity models consider dislocations in the intragranular material and within the grain interior. For such a model the primary length parameter is the length of the Burgers vector.

The conventional crystal plasticity model of Asaro and Needleman [6] is extended in [68] to account dislocation dynamics. Two possibilities to introduce the scale dependence in the viscoelastic constitutive equations are represented. The first one consists in the representation of the slip resistance parameter in the way proposed by Han et al. [45], where it depends on the dislocation densities of different types. The second opportunity is the introduction of a gradient back stress, depending on the spatial gradient of the density of geometrically necessary dislocations. An overview on the existing scale dependent models is provided in [5, 38, 44, 138] among others.

In [38] a scale dependent crystal plasticity model in the finite strain

framework is presented. The slip resistance parameter is assumed to be dependent on dislocation densities. In addition, this work offers an explanation of dislocations nature and their type.

## **2.3.5 Comparison of both approaches**

### **2.3.5.1 Comparison by the predicted creep strain rate level**

Currently both ways of creep modeling (crystallographic and based on creep potential) are used to describe inelastic deformation of a crystalline material. In the previous Sects. 2.3.2 and 2.3.4 a brief overview on the existing models is given. The aim of the current section is to compare both models, representing two different ways of simulation. Han et al. [46, 47] compared pure phenomenological (the model, based on creep potential) and crystallographic models for the case of plasticity. The pure phenomenological model is based on the viscoplastic constitutive equations of Chaboche [25] for isotropic materials. The extension for the anisotropic case is done by introducing the yield criterion, the back stress and the kinematic hardening in the anisotropic form. For the crystallographic model constitutive equations [25] are adopted for every of 18 slip systems, which possesses nickel base single crystal superalloy material. The procedure to identify material model parameters is developed and applied for the same experimental data in order to enable results comparison for both models.

After the comparison, the authors conclude that model, based on creep potential and crystallographic model have strong similarities. Significant differences appear after a direct comparison of the results at various orientations. To check this the peak stresses corresponding to the total strain of 1.2% were compared. The results of both models for the crystals near [001] and [111] orientations correspond well while the maximum relative error near [011] orientation was found around 17%. This can be partly explained by the fact that the total inelastic strain of the crystal near [001] orientation is dominated by the octahedral slip and of the [111] oriented crystal by the cubic slip. The total inelastic strain of the [011] oriented crystal consists of the contribution of both slip systems. The diagrams of the relative errors between these two models shows significant peaks at the orientations, where both slip systems interaction takes place. Thus the better representation of the slip systems interaction during creep of crystal is required.

In the current work the aim is set to perform similar comparison for both approaches for the creep models based on the same constitutive law of strain

rate evolution. The total amount of creep strain for the crystals of various orientations, predicted separately by each model, as a comparison criteria is used. As far as simulations are performed with the help of Mathcad software, the estimation of the computational time is difficult. The simulation will include a material parameter identification for both models, and numerical tests in some characteristic directions to evaluate the strain rate at every separate slip system.

For the comparison with the anisotropic model, based on creep potential, described in Sect. 2.1, crystal viscoplasticity model, proposed in [100], is used. Both models are based on the power law creep and are relatively simple in implementation.

According to the model of Ohno et al. [100] the total creep strain rate tensor is built as a sum of slip rates from every slip system along every  $k$ th direction multiplied by the orientation tensor:

$$\dot{\boldsymbol{\epsilon}}^{\text{cr}} = \sum_{k=1}^{12} \dot{\gamma}_{\text{oct1}}^{(k)} \boldsymbol{\alpha}_{\text{oct1}}^{(k)} + \sum_{k=1}^{12} \dot{\gamma}_{\text{oct2}}^{(k)} \boldsymbol{\alpha}_{\text{oct2}}^{(k)} + \sum_{k=1}^6 \dot{\gamma}_{\text{cub}}^{(k)} \boldsymbol{\alpha}_{\text{cub}}^{(k)}. \quad (2.39)$$

The orientation tensor  $\boldsymbol{\alpha}_s^{(k)}$  can be expressed through the unit vectors, defining the slip direction  $\mathbf{b}_s^k$  and normal to the slip plane  $\mathbf{v}_s^k$  in the following form:

$$\boldsymbol{\alpha}_s^{(k)} = \frac{1}{2} \left( \mathbf{b}_s^k \otimes \mathbf{v}_s^k + \mathbf{v}_s^k \otimes \mathbf{b}_s^k \right), \quad (2.40)$$

where  $s = \text{oct1, oct2, cub}$ . The values of the vectors  $\mathbf{b}_s^k$  and  $\mathbf{v}_s^k$  used in the current calculation are given in Appendix C.

The slip rate in its turn, as it was mentioned above, is developed by power law according to the shear stress of the  $k$ th slip system:

$$\dot{\gamma}_s^{(k)} = K_s \text{sign}[\tau_s^{(k)}] [\tau_s^{(k)}]^{n_s}. \quad (2.41)$$

If  $\boldsymbol{\sigma}$  is the applied stress tensor to the crystalline body, then:

$$\tau_s^{(k)} = \text{tr} \left( \boldsymbol{\sigma} \cdot \boldsymbol{\alpha}_s^{(k)} \right). \quad (2.42)$$

In general, to identify material model parameters for the single crystal FCC material tensile tests in 2 directions are used. These are tests on [001] and [111] oriented single crystal specimens. Tension in these directions is used for the activation of only one of the slip systems. For instance, in the [001]-oriented crystal only octahedral system operates, whereas in [111]-oriented crystal only the cubic one [29].

In the reference article of Ohno et al. [100] creep constants for different slip systems in a directionally solidified alloy IN738LC are presented:

$$\begin{aligned} K_{\text{Oct1}} &= 1.07 \cdot 10^{-23} \frac{(\text{MPa})^{-n}}{h}, & K_{\text{Oct2}} &= 4.91 \cdot 10^{-23} \frac{(\text{MPa})^{-n}}{h}, \\ K_{\text{Cub}} &= 1.41 \cdot 10^{-24} \frac{(\text{MPa})^{-n}}{h}. \end{aligned} \quad (2.43)$$

The power law exponent  $n = 9.2$  is similar for every slip system. The following assumption is often used for the materials with different origins of anisotropy, for example, the case of weld metals is discussed in [56]. The difficulties in individual determination of  $n$  for every slip system can be connected with the lack of experimental data. For its determination it is necessary to have tensile tests for all characteristic directions under wide range of applied stresses. Nevertheless the aim of the current simulation is to compare two approaches. The precise simulation of definite material behavior is not required and the assumption of equal power law exponent for every slip system is acceptable. Also the same power law exponent for the anisotropic creep model is assumed. Other material parameters  $a$  and  $\xi$  can be determined numerically, following the procedure derived in Sect. 2.3.3. Only the longitudinal strains  $\dot{\epsilon}_{[001]}^{\text{cr}}$  and  $\dot{\epsilon}_{[111]}^{\text{cr}}$  should be taken not as experimental data, but that one calculated in Mathcad for the crystallographic model in the directions [001] and [111], correspondingly. The parameters determined in this way are:

$$a = 2.019 \cdot 10^{-25} \frac{(\text{MPa})^{-n}}{h}, \quad \xi = 0.508.$$

In this way one material by means of two different models is presented. To evaluate creep response of these models three tests are performed. These are [011] – tensile test, shear test and the test, activating slip of the octahedral plane, already described above and illustrated in Fig. 2.1.

For every tests creep strain rates are plotted in the most characteristic directions. They are calculated in the following way:

$$\begin{aligned} \dot{\epsilon}_{[011]}^{\text{cr}} &= \mathbf{n}_{[011]} \cdot \dot{\boldsymbol{\epsilon}}^{\text{cr}} \cdot \mathbf{n}_{[011]}^{\text{T}}, \\ \dot{\epsilon}_{\text{shear}}^{\text{cr}} &= \mathbf{g}_2 \cdot \dot{\boldsymbol{\epsilon}}^{\text{cr}} \cdot \mathbf{g}_3^{\text{T}}, \\ \dot{\epsilon}_{\text{Oct}}^{\text{cr}} &= \mathbf{n}_{\text{Oct}} \cdot \dot{\boldsymbol{\epsilon}}^{\text{cr}} \cdot \mathbf{n}_{\text{Oct}}^{\text{T}}, \end{aligned} \quad (2.44)$$

where  $\mathbf{n}_{[011]} = \frac{1}{\sqrt{2}}(\mathbf{g}_2 + \mathbf{g}_3)$  and  $\mathbf{n}_{\text{Oct}} = \frac{1}{\sqrt{6}}(-\mathbf{g}_1 - \mathbf{g}_2 + 2\mathbf{g}_3)$ .

In Fig. 2.5 the creep strain rate evolution with respect to the applied stress is demonstrated. In octahedral slip test there is a good correlation of

both models. The shear and tensile at [011] oriented crystal tests show a big difference. The recalculation of  $\xi$  parameter taking into account only the second octahedral slip system improves significantly the agreement between both models at shear test.

### 2.3.5.2 Creep properties variation with the crystallographic orientation

In order to illustrate the symmetry type of the creep strain rate tensor (2.36) derived for the model, based on the creep potential its dependence on the crystallographic directions is defined. Using the notations, introduced in Sect. 2.2, the projection operators are:

$$\mathbf{m} \otimes \mathbf{m} \cdot \mathbb{P}_2 \cdot \mathbf{m} \otimes \mathbf{m} = \alpha - \frac{1}{3},$$

$$\mathbf{m} \otimes \mathbf{m} \cdot \mathbb{P}_3 \cdot \mathbf{m} \otimes \mathbf{m} = 1 - \alpha,$$

where

$$\alpha = \sum_{l=1}^3 (\mathbf{m} \cdot \mathbf{g}_l)^4.$$

With this operators the expression for the equivalent stress (2.37) can be rewritten as follows:

$$\begin{aligned} \sigma_{\text{eq}}^2 &= \frac{3}{2} \sigma_0^2 \left( \alpha - \frac{1}{3} + \xi(1 - \alpha) \right) \\ &= \sigma_0^2 \left( \frac{3}{2} \alpha - \frac{1}{2} + \frac{3}{2} \xi(1 - \alpha) \right). \end{aligned} \quad (2.45)$$

Introducing the notation:

$$\omega = \sqrt{\frac{1}{2} [3\alpha - 1 + 3\xi(1 - \alpha)]},$$

we obtain:

$$\sigma_{\text{eq}} = \sigma_0 \omega. \quad (2.46)$$

Substituting the obtained expression for the equivalent stress in Eq. (2.36) for the creep strain rate tensor the expression for the resultant creep strain rate in the arbitrary direction  $\mathbf{m}$  is obtained:

$$\begin{aligned} \dot{\epsilon}_{mm}^{\text{cr}} &= \frac{3}{2} a (\sigma_0 \omega)^{n-1} \sigma_0 \left[ \alpha - \frac{1}{3} + \xi(1 - \alpha) \right] \\ &= a \omega^{n+1} \sigma_0^n. \end{aligned} \quad (2.47)$$

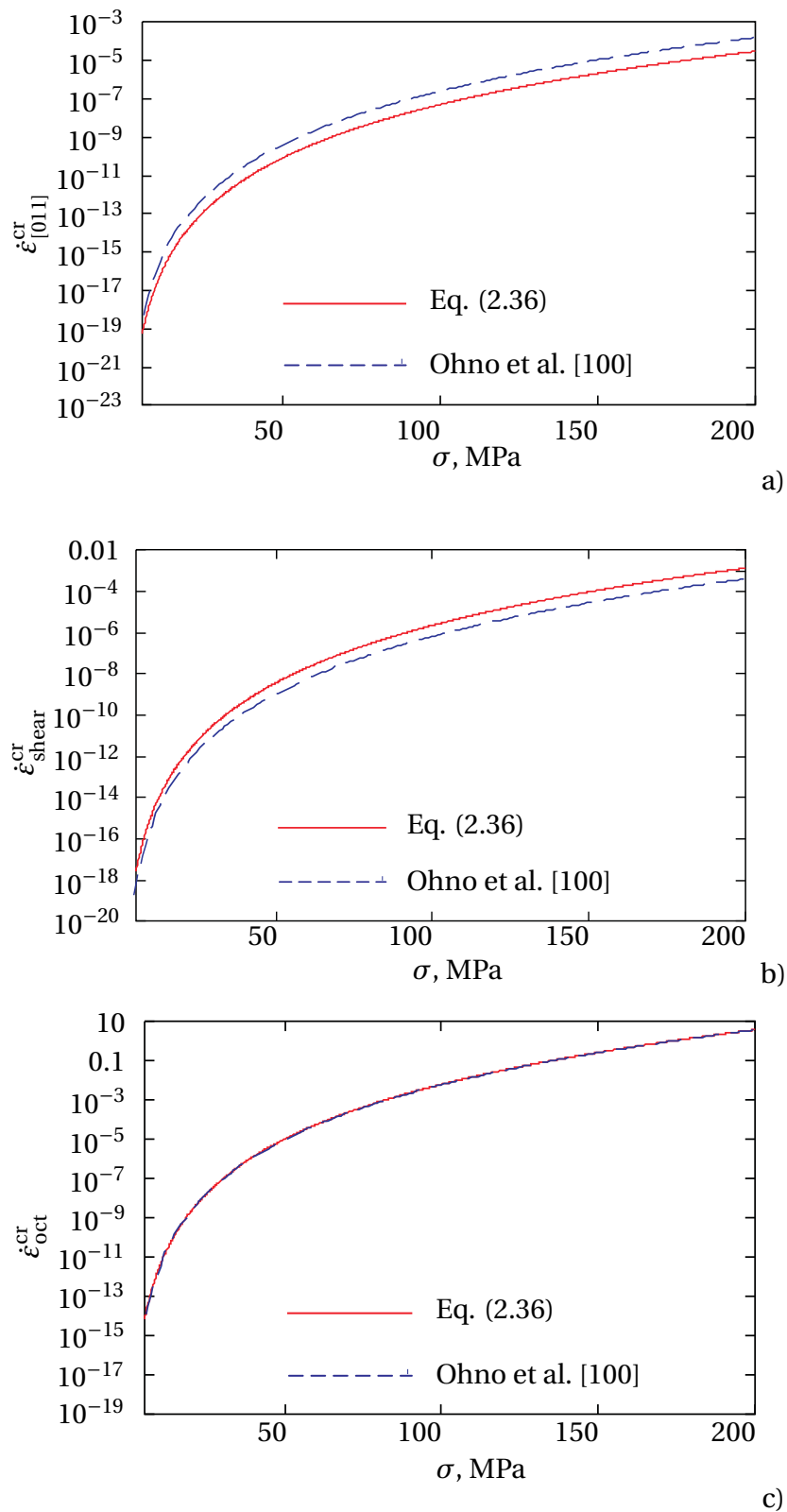


**Figure 2.5** Value of creep strain rate in crystalline calculated with both models at different loadings: a) tension in [011] direction; b) shear test; c) octahedral slip

After normalizing this expression on the value of the magnitude of the applied stress as in the case of elasticity, presented in Sect. 2.2, the equation of the surface, characterizing change of the creep strain rate with the crystallographic orientation is obtained:

$$\frac{\dot{\epsilon}_{mm}^{cr}}{\sigma_0^n} = a\omega^{n+1}. \quad (2.48)$$

To perform the comparison of the symmetry types, prescribed by both creep models, the following surface with the material model parameters, determined in Sect. 2.3.5 for the model, based on the creep potential, is built and presented in Fig. 2.6.

To investigate the variation of the creep properties in the crystalline material, predicted by the crystallographic model [100], the expression for the creep strain rate acting on the plane with the arbitrary normal  $\mathbf{m}$  (Fig. 2.3) should be derived. The creep strain rate tensor is presented in Eq. (2.39), where the shear strain rate, corresponding to the  $k$ th slip system is shown in Eq. (2.41). The resolved shear stress, corresponding to the  $s$ th slip system and

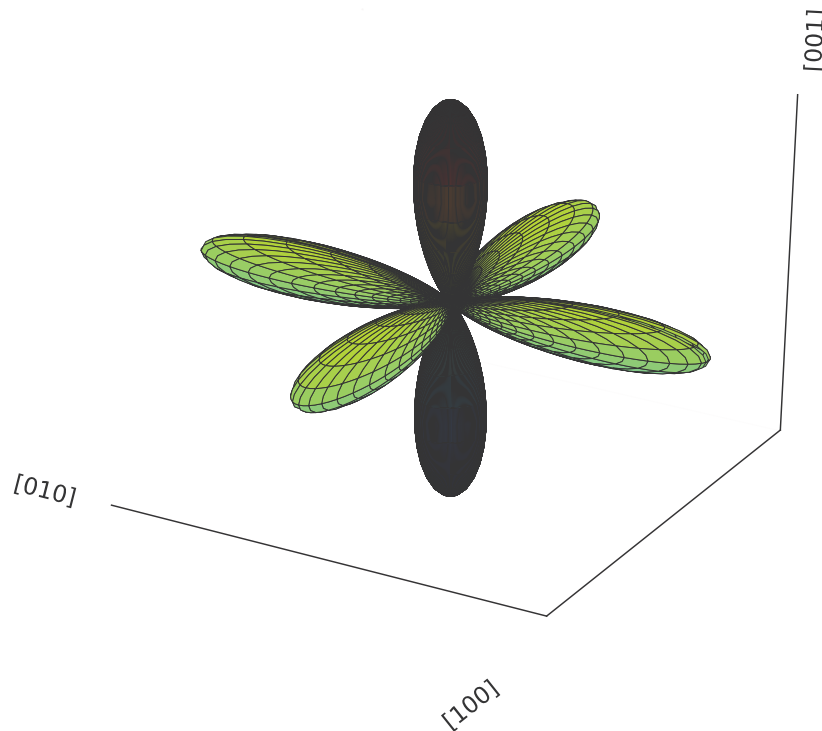


**Figure 2.6** Variation of the normalized creep strain rate with the crystallographic orientation, predicted by the model based on the creep potential

$k$ th slip direction can be expressed as follows:

$$\tau_s^{(k)} = \mathbf{b}_s^k \cdot \boldsymbol{\sigma} \cdot \mathbf{v}_s^k, \quad (2.49)$$

where  $\mathbf{b}_s^k$  are the slip directions and  $\mathbf{v}_s^k$  are the normals to the slip planes in the of crystallographic basis  $\mathbf{g}_i$ ,  $i = 1 \dots 3$ , represented in Fig. 2.3. In the component form both vectors can be expressed as:

$$\mathbf{b}_s^k = (b_s^k)^i \mathbf{g}_i,$$

$$\mathbf{v}_s^k = (v_s^k)^i \mathbf{g}_i,$$

where  $(b_s^k)^i$  and  $(v_s^k)^i$ , are coordinates of the correspondent vectors.

For the stress tensor  $\boldsymbol{\sigma} = \sigma_0 \mathbf{m} \otimes \mathbf{m}$  Eq. (2.49) takes the form:

$$\tau_s^{(k)} = \sigma_0 (\mathbf{m} \cdot \mathbf{b}_s^k) (\mathbf{m} \cdot \mathbf{v}_s^k). \quad (2.50)$$

Denotation of the scalar product of the slip direction vector on the normal  $\mathbf{m}$  as  $\Omega$  and of the scalar product of the normal to the slip plane on the normal  $\mathbf{m}$  as  $\Gamma$  results in:

$$\Omega_s^k = \mathbf{m} \cdot \mathbf{b}_s^k = \sum_{j=1}^3 (b_s^k)^j \mathbf{m} \cdot \mathbf{g}_j,$$

$$\Gamma_s^k = \mathbf{m} \cdot \mathbf{v}_s^k = \sum_{j=1}^3 (v_s^k)^j \mathbf{m} \cdot \mathbf{g}_j,$$

where  $\mathbf{m} \cdot \mathbf{g}_j$  are projections of the normal  $\mathbf{m}$  on the crystallographic basis, formerly defined in Eq. (2.7). With this, the expression for the shear stress can be rewritten in the form:

$$\tau_s^{(k)} = \sigma_0 \Omega_s^k \Gamma_s^k. \quad (2.51)$$

Substituting (2.51) in (2.39) one can obtain:

$$\dot{\epsilon}_{\text{mm}}^{\text{cr}} = 2\sigma_0^n \sum_s K_s (\Omega_s \Gamma_s)^{n+1} \text{sign}(\Omega_s \Gamma_s),$$

with the notation

$$Z_s = (\Omega_s \Gamma_s)^{n+1} \text{sign}(\Omega_s \Gamma_s)$$

one can finally get the expression of the creep strain rate evolving in the direction  $\mathbf{m}$ :

$$\dot{\epsilon}_{\text{mm}}^{\text{cr}} = 2\sigma_0^n (K_{\text{Oct1}} Z_{\text{Oct1}} + K_{\text{Oct2}} Z_{\text{Oct2}} + K_{\text{Cub}} Z_{\text{Cub}}). \quad (2.52)$$

Normalizing the expression for the creep strain rate tensor to the power law constant of the first octahedral system one can obtain the equation, qualitatively characterizing change of the creep properties with the crystallographic direction:

$$\frac{\dot{\varepsilon}_{mm}^{cr}}{2K_{oct1}\sigma_0^n} = Z_{oct1} + \frac{K_{oct2}}{K_{oct1}}Z_{oct2} + \frac{K_{cub}}{K_{oct1}}Z_{cub}. \quad (2.53)$$

The surface, corresponding to Eq. (2.53), with the material model parameters (2.43) is presented in Fig. 2.7.

Comparing Figs. 2.6 and 2.7 one can see that both figures have similar symmetries. The values of the creep strain rates have maximum in the directions  $\langle 001 \rangle$  for both models. In Fig. 2.7 some additional convex sections in the central region can be observed, which are completely absent in the surface in Fig. 2.6. Due to their small magnitude their contribution to the results discrepancy of two models is small. More pronounced distinction lies in the volume of the  $\langle 001 \rangle$ -oriented sections. The volume of the surface, correspondent to the material with the cubic symmetry is influenced by  $\xi$  coefficient. The optimal value is found close to 0.75 and the corrected surface is presented in Fig. 2.8. The following value of  $\xi$  improves the result

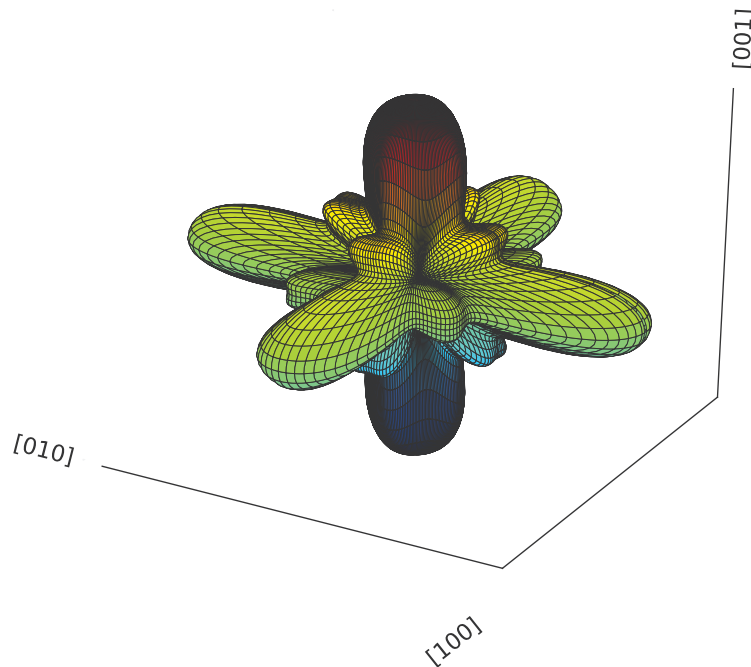


**Figure 2.7** Variation of the normalized creep strain rate, predicted by the crystal plasticity model

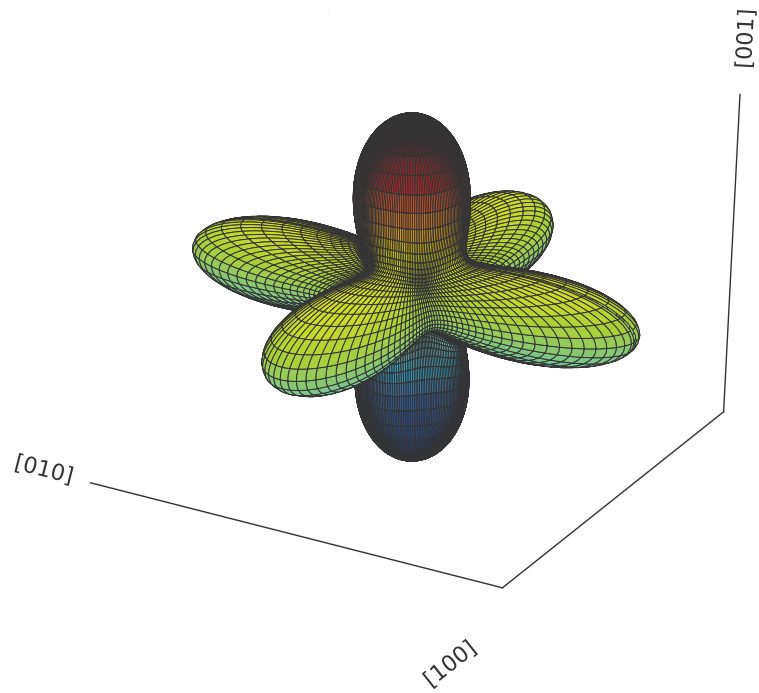


**Figure 2.8** Variation of the normalized creep strain rate, predicted by the model based on creep potential for  $\xi = 0.75$

discrepancies between both models for the tension test of [011]-oriented crystal. The conclusion arises that the determination of  $\xi$  coefficient by Eq. (2.38) leads to its significant underestimation and should be taken into account during the further calculations.

---

## Grain boundary sliding

The main mechanisms leading to the creep fracture are found to be dislocation creep within the grain, diffusion transport of matter from the grain boundaries or interior and grain boundary sliding (GBS). If one performs the creep simulation up to fracture on the microlevel all these processes should be reflected as resulting in the material softening during the tertiary creep. Therefore the aim of this chapter is to introduce constitutive equations for the grain boundary sliding and to show its contribution during the secondary and the tertiary creep stages.

### 3.1 Nature of the grain boundary sliding

The grain boundary sliding in a polycrystalline material is not an independent process and does not occur in the polycrystalline material instantly after applying the load. It occurs owing to the intragranular deformation and in this way contributes to the total creep strain. Thus, the diffusion creep [22, 111], the dislocation creep [42] or both processes occurring in the grain interior can generate the grain boundary sliding. Different grain boundary sliding models are presented in the literature starting from the pioneering work [10].

The source of diffusion creep is the presence of vacancies or in other words point defects in a crystalline material. Under conditions of high temperature the applied stress activates vacancies diffusion from the compressed grain boundaries to that one, undergoing tension. This process is followed then by diffusion in the opposite direction. The phenomena of diffusion transport of matter in the material is described e.g., Poirier [108]. Such type of

intergranular deformation activates diffusion near the grain boundaries and leads to the sliding of mutual grains. In this case the grain boundary sliding is geometrically characterized by elongation of grains along the specimen, meanwhile the number of grains along the specimen length stays the same. This type of GBS is called Lifshitz sliding [72].

The description of the grain sliding rate accumulated due to diffusion creep is made through the material parameters such as grain-boundary diffusivity, grain boundary width, average grain size, besides the driving forces for the GBS such as applied stress and temperature. At first the model of such type was introduced in [111] and then improved in [42].

Dislocation based creep leads to another type of the GBS, so called Rachinger type [110] of sliding, which is characterized by an increased grain number along the specimen, but mostly does not influence the grain shape. The slip within the grain interior leads to accumulation of dislocations on the grain boundaries. The sliding occurs because the continuity between the mutual grains should be held. As a consequence the high-angle boundaries have a higher tendency to sliding, because the dislocations within low-angle boundaries can freely slide under applied stress, not causing the displacement of grain boundaries. In Fig. 3.1 the micrograph of OFHC copper, tested at creep conditions at 676 °C is shown. The GBS is estimated by measurement of

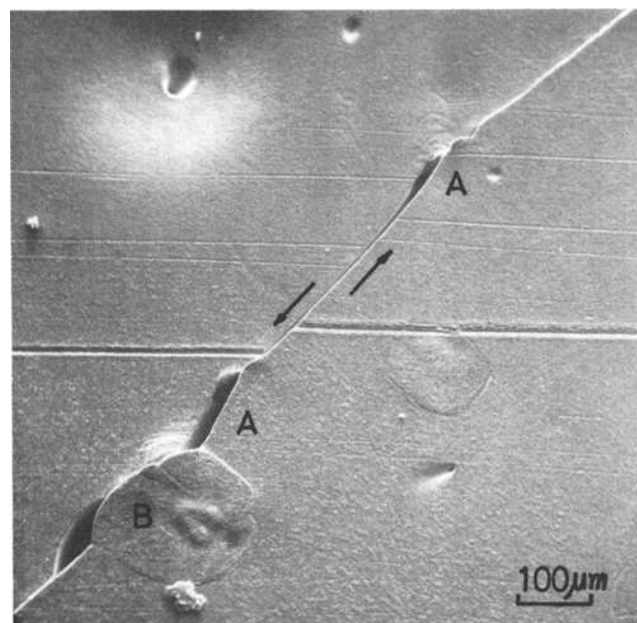


**Figure 3.1** Manifestation of GBS in copper at 676 °C, after [133]. The grain boundary irregularities: bend (A) and island grain (B).

the offset of transversal marker line, traced on the specimen surface before testing. As a result for the current example the cavity formation due to interaction of the grain boundary irregularities and grain boundary sliding is observed.

## 3.2 Grain boundary sliding modeling

A widely used way of the polycrystalline geometry representation is the two-dimensional massive of equal size hexagons. Such geometry is considered in [28] in order to simulate grain boundary sliding. The problem is solved with assumptions of a plane strain under applied shear stress. Grain elements are prescribed to deform inelastically by power law. The grains are connected by thin layers of grain boundary elements, which are prescribed to shear in a Newtonian viscous manner. Different ways of viscosity coefficient derivation are proposed depending on the grain boundary geometry.

Van der Giessen and Tvergaard [129] supplement [28] with a grain boundary cavitation model. The axisymmetric problem is analyzed under constant tension conditions.

In [42] the improved geometry of a grain is considered as a core with a conventional single crystal behavior and a mantle, possessing additional slip systems. The mantle, as a creep softer region is used to introduce grain boundary sliding. The material response of the set of alloys during superplasticity and creep is considered. Under this condition the author accounts the fold formation, dislocation motion and pure diffusion as mechanisms relevant at grain boundary sliding. The comparison of simulated strain rate – stress curves with experimental data is presented.

In the current research grain boundary sliding due to dislocation creep in grains is simulated. As far as the microstructure of the polycrystal is directly considered, GBS can be represented by direct displacement of mutual grains, which should occur on some dependence on the applied shear stress. In the unit cell without grain boundary layer grain boundary sliding can be implemented by introducing special kind of interactions or boundary conditions between grains, for instance, by defining the traction–separation law available in Abaqus Standard. But such approach would lead to significant model complication and would increase calculation time.

In order to avoid these difficulties the so called grain boundary layer is introduced. It is designed as a separate part object in Abaqus and consists of plane regions of a non-zero thickness, connecting grains. The discussion of

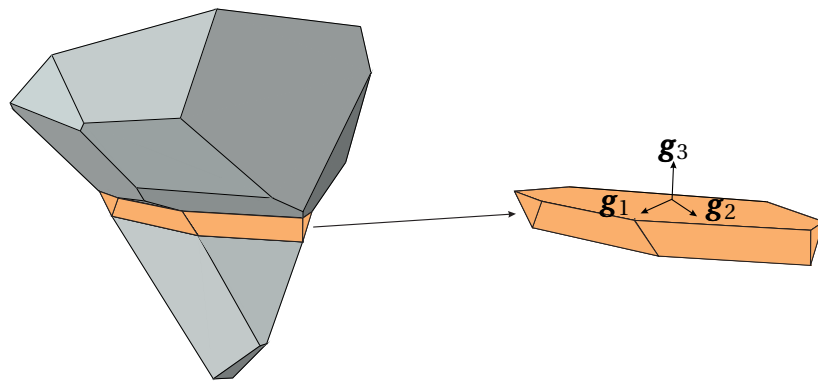


**Figure 3.2** Schematic representation of two grains connected by the grain boundary region with the specific material orientation

the detailed procedure of the layer construction is held in Chapter 5.1. Two grains of a random shape connected by grain boundary region are presented in Fig. 3.2. The thickness of this region is a pure phenomenological value and for this example taken by the illustrative reason.

For the grain boundary sliding representation the shear and the normal deformation of the grain boundary should be distinguished. To this purpose an individual local coordinate system is determined for every plane region of the grain boundary region. An example of such coordinate system is shown in the right-hand side of Fig. 3.2. In this case the direction  $\mathbf{g}_3$  is set as a normal to the grain boundary and the other two directions  $\mathbf{g}_1$  and  $\mathbf{g}_2$  are in the grain boundary plane. In the regions of grain boundaries junction the smooth transition from one coordinate system to another is automatically performed by Abaqus.

The material model implementation in Abaqus is done by the usage of user defined material. Within the UMAT (User Material) program the description of only one material behavior is possible. The different response of grain boundary material in different directions induces a higher level of symmetry than cubic, namely orthotropic. The constitutive equations for the cubic symmetry, presented in Sect. (2.1), should be rewritten for the case of orthotropy. The procedure of derivation of creep strain rate evolution equation for the material with different types of anisotropy is standard and presented, for instance, in [89].

The six orthotropic invariants of the elastic strain tensor can be introduced

in the following form:

$$\begin{aligned}
I_{n_1 n_1} &= \mathbf{n}_1 \cdot \boldsymbol{\varepsilon}^{\text{el}} \cdot \mathbf{n}_1 = \varepsilon_{11}, \\
I_{n_2 n_2} &= \mathbf{n}_2 \cdot \boldsymbol{\varepsilon}^{\text{el}} \cdot \mathbf{n}_2 = \varepsilon_{22}, \\
I_{n_3 n_3} &= \mathbf{n}_3 \cdot \boldsymbol{\varepsilon}^{\text{el}} \cdot \mathbf{n}_3 = \varepsilon_{33}, \\
I_{n_1 n_2} &= \mathbf{n}_1 \cdot \boldsymbol{\varepsilon}^{\text{el}} \cdot \mathbf{n}_2 = \varepsilon_{12}, \\
I_{n_1 n_3} &= \mathbf{n}_1 \cdot \boldsymbol{\varepsilon}^{\text{el}} \cdot \mathbf{n}_3 = \varepsilon_{13}, \\
I_{n_2 n_3} &= \mathbf{n}_2 \cdot \boldsymbol{\varepsilon}^{\text{el}} \cdot \mathbf{n}_3 = \varepsilon_{23},
\end{aligned} \tag{3.1}$$

where  $\mathbf{n}_i$ ,  $i = 1 \dots 3$  are unit vectors, characterizing three planes of material symmetry. The elastic strain energy is a quadratic form constructed on (3.1) and for the orthotropic case can be written as:

$$\begin{aligned}
U &= \frac{1}{2} \left[ (\alpha_1 I_{n_1 n_1} + \alpha_2 I_{n_2 n_2} + \alpha_3 I_{n_3 n_3})^2 + \beta_2 (I_{n_1 n_1} - I_{n_3 n_3})^2 \right. \\
&\quad \left. + \beta_3 (I_{n_2 n_2} - I_{n_3 n_3})^2 + \beta_1 (I_{n_1 n_1} - I_{n_2 n_2})^2 \right] + \beta_{12} I_{n_1 n_2}^2 + \beta_{13} I_{n_1 n_3}^2 + \beta_{23} I_{n_2 n_3}^2,
\end{aligned} \tag{3.2}$$

where  $\alpha_1$ ,  $\alpha_2$ ,  $\alpha_3$ ,  $\beta_1$ ,  $\beta_2$ ,  $\beta_3$ ,  $\beta_{12}$ ,  $\beta_{13}$ ,  $\beta_{23}$  are material parameters. To obtain the dependence of the stress tensor on the elastic strain tensor the well known Green's formula for the elastic strain energy can be used:

$$\boldsymbol{\sigma} = \frac{\partial U}{\partial \boldsymbol{\varepsilon}^{\text{el}}} = \frac{\partial U}{\partial I_{n_i n_j}} \frac{\partial I_{n_i n_j}}{\partial \boldsymbol{\varepsilon}^{\text{el}}}, \quad i, j = 1..3,$$

where  $I_{n_i n_j}$  is the invariant's set (3.1).

For the case of elasticity we assume that all elastic normal strains equally contribute to the stress tensor, it means that we can make the simplification  $\alpha_1 = \alpha_2 = \alpha_3$ . After some algebraical operations we obtain the stress-strain dependence for the case of orthotropy

$$\begin{aligned}
\boldsymbol{\sigma} &= \alpha_1^2 (\varepsilon_{11} + \varepsilon_{22} + \varepsilon_{33}) (\mathbf{n}_1 \otimes \mathbf{n}_1 + \mathbf{n}_2 \otimes \mathbf{n}_2 + \mathbf{n}_3 \otimes \mathbf{n}_3) \\
&\quad + [\beta_1 (\varepsilon_{11} - \varepsilon_{22}) + \beta_2 (\varepsilon_{11} - \varepsilon_{33})] \mathbf{n}_1 \otimes \mathbf{n}_1 + [\beta_1 (\varepsilon_{22} - \varepsilon_{11}) + \beta_3 (\varepsilon_{22} - \varepsilon_{33})] \mathbf{n}_2 \otimes \mathbf{n}_2 \\
&\quad + [\beta_2 (\varepsilon_{33} - \varepsilon_{11}) + \beta_3 (\varepsilon_{33} - \varepsilon_{22})] \mathbf{n}_3 \otimes \mathbf{n}_3 + 2\beta_{12} \varepsilon_{12} (\mathbf{n}_1 \otimes \mathbf{n}_2 + \mathbf{n}_2 \otimes \mathbf{n}_1) \\
&\quad + 2\beta_{13} \varepsilon_{13} (\mathbf{n}_1 \otimes \mathbf{n}_3 + \mathbf{n}_3 \otimes \mathbf{n}_1) + 2\beta_{23} \varepsilon_{23} (\mathbf{n}_2 \otimes \mathbf{n}_3 + \mathbf{n}_3 \otimes \mathbf{n}_2).
\end{aligned} \tag{3.3}$$

Through the following parameters set:

$$\alpha_1 = \sqrt{\frac{\lambda_1}{3}}, \quad \beta_1 = \beta_2 = \beta_3 = \frac{\lambda_2}{3}, \quad \beta_{12} = \beta_{13} = \beta_{23} = \frac{\lambda_3}{2}$$

equation (3.3) reduces to the cubic symmetry case (2.1).

The equation for the creep strain rate could be derived from the flow rule (2.17) [97]: where  $W$  is the creep potential, which is a function of the equivalent stress  $W(\boldsymbol{\sigma}) = W(\sigma_{\text{eq}}(\boldsymbol{\sigma}))$ , [89]. With this (2.17) could be rewritten as:

$$\dot{\boldsymbol{\epsilon}}^{\text{cr}} = \frac{\partial W}{\partial \sigma_{\text{eq}}} \frac{\partial \sigma_{\text{eq}}}{\partial \boldsymbol{\sigma}} = \dot{\boldsymbol{\epsilon}}_{\text{eq}}^{\text{cr}} \frac{\partial \sigma_{\text{eq}}}{\partial \boldsymbol{\sigma}}, \quad \dot{\boldsymbol{\epsilon}}_{\text{eq}}^{\text{cr}} \equiv \frac{\partial W}{\partial \sigma_{\text{eq}}}. \quad (3.4)$$

In order to introduce the equivalent stress in form valid for both orthotropic and cubic symmetry cases, let us introduce 6 invariants of the stress tensor, which satisfy the incompressibility condition:

$$\begin{aligned} \tilde{I}_{n_1 n_1} &= \mathbf{n}_1 \cdot \boldsymbol{\sigma} \cdot \mathbf{n}_1 - \frac{1}{3} \text{tr} \boldsymbol{\sigma}, \\ \tilde{I}_{n_2 n_2} &= \mathbf{n}_2 \cdot \boldsymbol{\sigma} \cdot \mathbf{n}_2 - \frac{1}{3} \text{tr} \boldsymbol{\sigma}, \\ \tilde{I}_{n_3 n_3} &= \mathbf{n}_3 \cdot \boldsymbol{\sigma} \cdot \mathbf{n}_3 - \frac{1}{3} \text{tr} \boldsymbol{\sigma}, \\ \tilde{I}_{n_1 n_2} &= \mathbf{n}_1 \cdot \boldsymbol{\sigma} \cdot \mathbf{n}_2 = \tau_{12}, \\ \tilde{I}_{n_1 n_3} &= \mathbf{n}_1 \cdot \boldsymbol{\sigma} \cdot \mathbf{n}_3 = \tau_{13}, \\ \tilde{I}_{n_2 n_3} &= \mathbf{n}_2 \cdot \boldsymbol{\sigma} \cdot \mathbf{n}_3 = \tau_{23}. \end{aligned} \quad (3.5)$$

Then the expression for the equivalent stress can be written in the following form:

$$\begin{aligned} \sigma_{\text{eq}}^2 &= \frac{1}{2} \mu_2 (\tilde{I}_{n_2 n_2} - \tilde{I}_{n_3 n_3})^2 + \frac{1}{2} \mu_3 (\tilde{I}_{n_3 n_3} - \tilde{I}_{n_1 n_1})^2 + \frac{1}{2} \mu_1 (\tilde{I}_{n_1 n_1} - \tilde{I}_{n_2 n_2})^2 \\ &+ 3\mu_{12} \tilde{I}_{n_1 n_2}^2 + 3\mu_{13} \tilde{I}_{n_1 n_3}^2 + 3\mu_{23} \tilde{I}_{n_2 n_3}^2, \end{aligned} \quad (3.6)$$

where  $\mu_1$ ,  $\mu_2$ ,  $\mu_3$ ,  $\mu_{12}$ ,  $\mu_{13}$  and  $\mu_{23}$  are material model parameters, which should be determined from the creep curves. Using the flow rule (2.17) and the expression for the equivalent stress (3.6) the following dependence can be

derived:

$$\begin{aligned}
\dot{\boldsymbol{\varepsilon}}^{\text{cr}} &= \frac{\dot{\varepsilon}_{\text{eq}}^{\text{cr}}}{2\sigma_{\text{eq}}} \left( \frac{\partial \sigma_{\text{eq}}}{\partial \tilde{I}_{n_1 n_1}} \frac{\partial \tilde{I}_{n_1 n_1}}{\partial \boldsymbol{\sigma}} + \frac{\partial \sigma_{\text{eq}}}{\partial \tilde{I}_{n_2 n_2}} \frac{\partial \tilde{I}_{n_2 n_2}}{\partial \boldsymbol{\sigma}} + \frac{\partial \sigma_{\text{eq}}}{\partial \tilde{I}_{n_3 n_3}} \frac{\partial \tilde{I}_{n_3 n_3}}{\partial \boldsymbol{\sigma}} \right. \\
&\quad \left. + \frac{\partial \sigma_{\text{eq}}}{\partial \tilde{I}_{n_1 n_2}} \frac{\partial \tilde{I}_{n_1 n_2}}{\partial \boldsymbol{\sigma}} + \frac{\partial \sigma_{\text{eq}}}{\partial \tilde{I}_{n_1 n_3}} \frac{\partial \tilde{I}_{n_1 n_3}}{\partial \boldsymbol{\sigma}} + \frac{\partial \sigma_{\text{eq}}}{\partial \tilde{I}_{n_2 n_3}} \frac{\partial \tilde{I}_{n_2 n_3}}{\partial \boldsymbol{\sigma}} \right) \\
&= \frac{\dot{\varepsilon}_{\text{eq}}^{\text{cr}}}{2\sigma_{\text{eq}}} \left( \mu_3 (\tilde{I}_{n_1 n_1} - \tilde{I}_{n_3 n_3}) \frac{\partial \tilde{I}_{n_1 n_1}}{\partial \boldsymbol{\sigma}} + \mu_1 (\tilde{I}_{n_1 n_1} - \tilde{I}_{n_2 n_2}) \frac{\partial \tilde{I}_{n_1 n_1}}{\partial \boldsymbol{\sigma}} \right. \\
&\quad + \mu_2 (\tilde{I}_{n_2 n_2} - \tilde{I}_{n_3 n_3}) \frac{\partial \tilde{I}_{n_2 n_2}}{\partial \boldsymbol{\sigma}} + \mu_1 (\tilde{I}_{n_2 n_2} - \tilde{I}_{n_1 n_1}) \frac{\partial \tilde{I}_{n_2 n_2}}{\partial \boldsymbol{\sigma}} \\
&\quad + \mu_2 (\tilde{I}_{n_3 n_3} - \tilde{I}_{n_2 n_2}) \frac{\partial \tilde{I}_{n_3 n_3}}{\partial \boldsymbol{\sigma}} + \mu_3 (\tilde{I}_{n_3 n_3} - \tilde{I}_{n_1 n_1}) \frac{\partial \tilde{I}_{n_3 n_3}}{\partial \boldsymbol{\sigma}} \\
&\quad \left. + 6\mu_{12} \tilde{I}_{n_1 n_2} \frac{\partial \tilde{I}_{n_1 n_2}}{\partial \boldsymbol{\sigma}} + 6\mu_{13} \tilde{I}_{n_1 n_3} \frac{\partial \tilde{I}_{n_1 n_3}}{\partial \boldsymbol{\sigma}} + 6\mu_{23} \tilde{I}_{n_2 n_3} \frac{\partial \tilde{I}_{n_2 n_3}}{\partial \boldsymbol{\sigma}} \right). \tag{3.7}
\end{aligned}$$

After calculation the partial derivations of the stress invariants with respect to the stress tensor

$$\begin{aligned}
\frac{\partial \tilde{I}_{n_1 n_1}}{\partial \boldsymbol{\sigma}} &= \mathbf{n}_1 \otimes \mathbf{n}_1 - \frac{1}{3} \mathbf{I}, \\
\frac{\partial \tilde{I}_{n_2 n_2}}{\partial \boldsymbol{\sigma}} &= \mathbf{n}_2 \otimes \mathbf{n}_2 - \frac{1}{3} \mathbf{I}, \\
\frac{\partial \tilde{I}_{n_3 n_3}}{\partial \boldsymbol{\sigma}} &= \mathbf{n}_3 \otimes \mathbf{n}_3 - \frac{1}{3} \mathbf{I}, \\
\frac{\partial \tilde{I}_{n_1 n_2}}{\partial \boldsymbol{\sigma}} &= \mathbf{n}_1 \otimes \mathbf{n}_2 + \mathbf{n}_2 \otimes \mathbf{n}_1, \\
\frac{\partial \tilde{I}_{n_1 n_3}}{\partial \boldsymbol{\sigma}} &= \mathbf{n}_1 \otimes \mathbf{n}_3 + \mathbf{n}_3 \otimes \mathbf{n}_1, \\
\frac{\partial \tilde{I}_{n_2 n_3}}{\partial \boldsymbol{\sigma}} &= \mathbf{n}_2 \otimes \mathbf{n}_3 + \mathbf{n}_3 \otimes \mathbf{n}_2
\end{aligned}$$

we obtain after some algebra the expression for the creep strain rate in the

following form:

$$\begin{aligned}
\dot{\boldsymbol{\epsilon}}^{\text{cr}} = & \frac{\dot{\epsilon}_{\text{eq}}^{\text{cr}}}{2\sigma_{\text{eq}}} \left[ \left( \mathbf{n}_1 \otimes \mathbf{n}_1 - \frac{1}{3}\mathbf{I} \right) (\mu_3(\sigma_{11} - \sigma_{33}) + \mu_1(\sigma_{11} - \sigma_{22})) \right. \\
& + \left( \mathbf{n}_2 \otimes \mathbf{n}_2 - \frac{1}{3}\mathbf{I} \right) (\mu_2(\sigma_{22} - \sigma_{33}) + \mu_1(\sigma_{22} - \sigma_{11})) \\
& + \left( \mathbf{n}_3 \otimes \mathbf{n}_3 - \frac{1}{3}\mathbf{I} \right) (\mu_2(\sigma_{33} - \sigma_{22}) + \mu_3(\sigma_{33} - \sigma_{11})) \\
& + 6\mu_{12}\tau_{12}(\mathbf{n}_1 \otimes \mathbf{n}_2 + \mathbf{n}_2 \otimes \mathbf{n}_1) + 6\mu_{13}\tau_{13}(\mathbf{n}_1 \otimes \mathbf{n}_3 + \mathbf{n}_3 \otimes \mathbf{n}_1) \\
& \left. + 6\mu_{23}\tau_{23}(\mathbf{n}_2 \otimes \mathbf{n}_3 + \mathbf{n}_3 \otimes \mathbf{n}_2) \right]. \tag{3.8}
\end{aligned}$$

The sliding deformation is assumed to occur also by power law and the expression for the equivalent creep strain rate  $\dot{\epsilon}_{\text{eq}}^{\text{cr}}$  for this case takes the form:

$$\dot{\epsilon}_{\text{eq}}^{\text{cr}} = a\sigma_{\text{eq}}^n. \tag{3.9}$$

The expression for the equivalent stress (3.6) can be written through the stress tensor components as:

$$\begin{aligned}
\sigma_{\text{eq}}^2 = & \frac{1}{2}\mu_2(\sigma_{22} - \sigma_{33})^2 + \frac{1}{2}\mu_3(\sigma_{33} - \sigma_{11})^2 + \frac{1}{2}\mu_1(\sigma_{11} - \sigma_{22})^2 \\
& + 3\mu_{12}\tau_{12}^2 + 3\mu_{13}\tau_{13}^2 + 3\mu_{23}\tau_{23}^2. \tag{3.10}
\end{aligned}$$

Written in this form Eqs. (3.10) and (3.8) allow transition to the correspondent Eqs. (2.37) and (2.36) for the cubic symmetry case by the following set of material model parameters:

$$\mu_1 = \mu_2 = \mu_3 = 1, \quad \mu_{12} = \mu_{13} = \mu_{23} = \xi. \tag{3.11}$$

As it was mentioned above only shear strain components should contribute to the overall deformation of the grain boundary region. In the elastic deformation region it leads to the assumption that the boundary region possesses higher stiffness in normal directions, in comparison to grain material. In creep deformation region the contribution of the normal stress components to the creep strain rate is minimized by setting in Eq. (3.8)  $\mu_1 = \mu_2 = \mu_3 = 0$ . Other material parameters are determined from numerical tests and comparison with experimental data [7].

---

## Creep cavitation

The following chapter is dedicated to the description of the tertiary creep stage in a polycrystalline material, where the fracture occurs due to the grain boundary cavitation. The way of cavitation depends on the processes accommodating creep during the first two stages. For example, under lower applied stress the diffusion of matter leads to the intensive cavity nucleation on the entire surface of grain boundary. When the processes of the dislocation slip are dominant within the grain interior, the fracture occurs due to the cavity growth, their coalescence and consequently macrocrack formation.

The grain boundary cavitation due to creep was studied by many authors and detailed classification of the approaches in modeling is given in textbooks [62, 113]. The aim of this chapter is to make a state of the art report and to ground the model choice for the current research.

### 4.1 Overview of existing models

#### 4.1.1 Cavitation due to diffusion processes

When the diffusion process is dominant in the material, the fracture occurs due to cavity nucleation. The brittle fracture occurs at the material point, when the entire grain boundary appear to be seeded by cavities. In this case the cavitation model should describe nucleation and diffusion controlled cavity growth processes. High temperature regimes and rather moderate external load initiate vacancy diffusion along the grain boundaries. It leads to vacancy transport and accumulation with subsequent cavity formation.

In the pioneering work of Hull and Rimmer [54] the cavity growth by grain boundary diffusion is examined, the contribution of the lattice diffusion is estimated to be around 6% of total diffusion and assumed to be negligible during cavitation. The classical equation of cavity radius growth is derived through the definition of the vacancy flux potential through the grain boundary. The cavitation is assumed to occur on the grain boundaries orthogonal to the applied tensile stress, as it was confirmed by many experiments, for instance [125]. This fact requires the introduction of the normal stress in the constitutive equation of cavity radius growth. The normal stress should operate as a driving force of the cavity nucleation and growth. The work of Hull and Rimmer [54] is extended in [112].

In [135] the variational approach in diffusion cavity growth is proposed. In contrast to Hull and Rimmer [54] the grain boundary and surface diffusion are assumed to be relevant during cavity formation and growth. To determine the flux of vacancies for a single cavity the minimum principle to the functional is applied. The vacancy flux for the multiple cavities is calculated by simple summation of single fluxes. For the finite element representation the cavity element is used, consisting of a grain boundary and two circular arcs, which intersect each other at the cavity tips. The validity of this scheme is formerly proved in [136]. In addition to the cavity growth the presented model is supplemented with the nucleation and coalescence by involving the remeshing rule. So, when a nucleation condition is held, the new cavity appears by addition of a new cavity element. And in opposite, the two cavity elements are substituted by one, when the coalescence of two cavities takes place. The results comparison with models of Tvergaard [127] and Onck and van der Giessen [101] is performed. In the real operating conditions the combined action of both vacancy diffusion and dislocation pile ups lead to cavitation. The models including both these processes are described in the further subsections.

#### **4.1.2 Cavitation models based on dislocation creep**

At lower temperature and higher magnitudes of loading the higher strain rates are revealed, initiating the slip within grain interior. The slip induces dislocations accommodation on the grain boundaries, which leads to cavity formation. In this case the cavitation modeling approach should base on the power law mechanism as the driving force to cavity nucleation and growth.

In [27] the approximate derivation of the creep cavity growth equation due to the power law creep is given. The extension to the multiaxial stress

state is presented by introducing only the influence of the hydrostatic pressure or tension. The equation of the rate of growth of the area fraction of holes is derived in the dependence on the steady state creep rate. The evolution equation of an axial strain rate of a cylinder with the damage parameter is given.

In [34] the validation of the model of Cocks and Ashby [27] is performed with the experimental data of cavitation in pure copper. The authors obtain the area fraction of voids from tomographic slices and perform comparison between the experiments and the model. In the work it is reported that the model underestimates the damage parameter value and more than twice overestimates the time to rupture. As a possible reason for this the absence in model of the continuous cavity nucleation due to diffusion creep is mentioned.

### **4.1.3 Cavitation due to various mechanisms**

The enhanced models, which can predict the time to rupture due to cavitation for a wider temperature and stress range should account for as much as possible microprocesses occurring in the polycrystal. In the model of Tvergaard [127] the cavity radius growth rate is described through the contribution of diffusion and dislocation creep parts and this model is used in the current work. The continuous cavity nucleation is assumed. In [74] the fracture modeling in a copper polycrystal is performed. In contrast to the conventional phenomenological damage variable the damage variable, based on a microcavitation model of Tvergaard [127], is involved to introduce the cavitation on the macrolevel. The 2D geometrical model based on Voronoi tessellation for the representation of a polycrystalline microstructure is used. The tertiary creep stage of the polycrystalline material is represented introducing the dependence of the creep strain rate on the micromechanical state variables, notably cavity radius and cavity spacing.

## **4.2 Tvergaard's cavitation model**

### **4.2.1 Cavity nucleation and growth equations**

In the current work the cavitation model, derived by Tvergaard [127] for the cavity growth due to both diffusion and power law creep is used. The schematic geometry of a grain boundary with cavities is presented in Fig. 4.1. The cavities of an average diameter  $2a$  are uniformly distributed with an

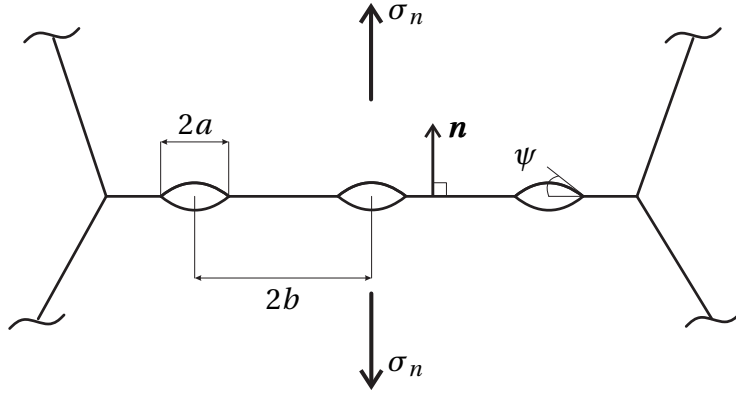


**Figure 4.1** Schematic representation of a cavitated grain boundary

average spacing  $2b$  on the grain boundary. The spherical-cup shaped cavities are considered, the cavity tip angle, characterizing the geometry, is assumed to be constant during cavity growth and equal  $2\psi \approx 75^\circ$ .  $\sigma_n$  is a normal tensile stress acting on the grain boundary. The cavity radius growth rate is assumed to consist of the diffusion  $\dot{V}_1$  and creep deformation  $\dot{V}_2$  parts:

$$\dot{a} = (\dot{V}_1 + \dot{V}_2) / [4\pi a^2 h(\psi)], \quad (4.1)$$

where  $h(\psi) = [(1 + \cos \psi)^{-1} - 0.5 \cos \psi] / \sin \psi$ . The cavity volume growth parts due to diffusion and dislocation creep are described as following:

$$\dot{V}_1 = 4\pi D \frac{\sigma_n}{\ln(1/f) - (3-f)(1-f)/2},$$

$$\dot{V}_2 = \begin{cases} \pm 2\pi \dot{\epsilon}_{\text{eq}}^{\text{cr}} a^3 h(\psi) \left( \frac{3}{2n} \left| \frac{\sigma_m}{\sigma_{\text{eq}}} \right| + \frac{(n-1)(n+0.4319)}{n^2} \right)^n & \text{for } \pm \frac{\sigma_m}{\sigma_{\text{eq}}} > 1, \\ 2\pi \dot{\epsilon}_{\text{eq}}^{\text{cr}} a^3 h(\psi) \left( \frac{3}{2n} + \frac{(n-1)(n+0.4319)}{n^2} \right)^n \frac{\sigma_m}{\sigma_{\text{eq}}} & \text{for } \left| \frac{\sigma_m}{\sigma_{\text{eq}}} \right| \leq 1. \end{cases}$$

The expression of the creep deformation cavity radius growth rate  $\dot{V}_2$  is written for the cases of low- and high-triaxiality of loading. The criteria, switching between these two cases, is the ratio of the mean and the equivalent stresses.  $D$  is a model parameter, related to the material diffusion,  $\dot{\epsilon}_{\text{eq}}^{\text{cr}}$  is already defined in Eq. (3.9).  $f$  serves as a length scale parameter, governing the rate of contribution of diffusion and power law creep to the cavity growth. According to [92] it is provided as follows:

$$f = \max \left\{ (a/b)^2, [a/(a+1.5L)]^2 \right\},$$

$$L = \left( D \sigma_{\text{eq}} / \dot{\epsilon}_{\text{eq}}^{\text{cr}} \right)^{1/3}.$$

In the current research the cavitation is prescribed to occur within the grain boundary region, therefore the equivalent stress  $\sigma_{eq}$  should be taken for the case of orthotropy as it is presented in Eq. (3.6). The normal stress  $\sigma_n$  is determined in Abaqus as the stress tensor component, acting in the normal direction  $\mathbf{g}_3$ , defined for the grain boundary region.  $\sigma_m$  is a mean stress applied to the grain boundary (see Fig. 3.2):

$$\sigma_m = \sum_{k=1}^3 \frac{\sigma_{kk}}{3}.$$

The stress tensor components  $\sigma_{kk}$ ,  $k = 1, 2, 3$ , are given for every element of the grain boundary region. Under the assumption of continuous cavity nucleation during creep, which is the case for the most engineering alloys, the equation of cavity spacing decrease rate can be expressed in the form:

$$\dot{b} = -\frac{\pi}{2} b^3 \beta \sigma_n^2 \dot{\epsilon}_{eq}^{cr}, \quad (4.2)$$

where  $\beta$  is a material parameter.

#### 4.2.2 Creep strain rate evolution due to cavitation

To describe the creep strain rate change due to the presence of cavities the constitutive equations of Cocks and Ashby [27] are involved. The proposed model describes the creep strain rate increase as a result of material softening during tertiary creep stage. The evolution equation of the creep strain rate is derived for a cylinder, loaded by a multiaxial traction. The proposed equation for the strain rate change in the axial direction of the cylinder has the form:

$$\frac{d\epsilon_a}{dt} = \dot{\epsilon}_{ss} \left\{ 1 + \frac{2r_h}{\alpha d} \left( \frac{1}{(1-f_h)^n} - 1 \right) \right\}. \quad (4.3)$$

The  $\epsilon_a$  is a strain in the axial direction of the cylinder,  $r_h$  is a radius of a circular hole, analogous to cavity radius  $a$ , described in Sect. 4.2.1,  $d$  is the grain size.  $\dot{\epsilon}_{ss}$  is the steady state strain rate in absence of voids defined in the current work in Eq. (3.9). The area fraction of holes on grain boundary  $f_h$  is determined in notations, used in previous subsection as:

$$f_h = \frac{a^2}{b^2}.$$

The quantity  $\alpha$  has the form:

$$\alpha = \frac{1}{\sinh \left\{ -2 \frac{(n-0.5)p}{(n+0.5)\sigma_{eq}} \right\}},$$

where  $p = -\frac{1}{3}\text{tr}\sigma$ .

Thus the constitutive equations of grain boundary cavitation consist in multiplying the creep strain rate tensor (3.8) on the coefficient in front of creep strain rate in Eq. (4.3). The exact form of this coefficient depends on the shape of inclusion and, for instance, is derived for a solid with crack inclusion in [114]. The evolution equation of cavity radius growth (4.1) and cavity spacing decrease (4.2) are taken from the model of Tvergaard [127].

### 4.3 Influence of cavities on the material behavior

The cavitation in a material is an indicator of forthcoming softening and the tertiary stage of the creep curve. Nevertheless many engineering materials spend during the tertiary creep stage the significant period of the lifetime and to improve the time to rupture prediction this period of the material lifetime should be simulated as more detailed as possible.

The influence of the appeared cavity on the creep deformation rate is described according to Cocks and Ashby [27] by dependence (4.3). But this model does not account for the stress redistribution within the material surrounding the cavity. On the macrolevel this task is successfully solved, for example, with the theory of M. Kachanov [59], representing the concept of an effective undamaged surface and acting on it an effective stress. This theory implies the introduction of the continuum damage variable, which is characterized by the occupied by voids and cracks surface, not resisting the applied load. On the microlevel one can introduce the elastic stiffness reduction due to voids, which accounts for the reduction of the surface, carrying the load.

The definition of the effective moduli of a solid with an inclusion has been an actual task for the scientist during the last decades. In most cases this task is solved with the application of the Eshelby tensor. The problem in this case consists in the consideration of an inhomogeneity, possessing different elastic properties, than surrounding it matrix. The solution of the Eshelby problem consists in the definition of the elastic fields, generated by, firstly, remotely applied stresses or strains and, secondly, prescribed eigenstrains in the inclusion domain. The solution of this problem for inclusions and holes of different shapes is discussed in details in [60, 93] for the case of an isotropic body.

The case of an orthotropic body with cylindrical cracks is considered in Monchiet et al. [81]. The homogenization scheme, based on the classical

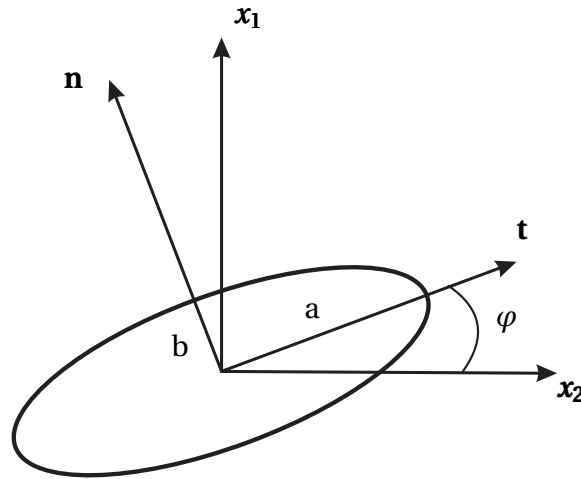


**Figure 4.2** Orientation of elliptical hole axes  $\mathbf{n}, \mathbf{t}$  with respect to the orthotropy axes  $\mathbf{x}_1, \mathbf{x}_2$

inclusion equivalent method is used to derive the effective stiffness tensor. The important task in the linkage of the micro- and macrolevels consists in the finding of the fourth-order localization tensor, relating the microscopic strain field to the macroscopic one. In [81] two ways of solution are proposed, depending on the concentration of the inhomogeneous inclusions. If the concentration of inclusions in the homogeneous matrix is assumed to be infinitesimal, the dilute scheme can be efficient. If the number of inclusions is high enough and interaction effects should be taken into account, the application of the Mori-Tanaka homogenization scheme is recommended [83].

The obtained solution is used to develop a micromechanical damage model for initially orthotropic materials such as unidirectional composites.

The effective moduli for an orthotropic solid with elliptical voids in plane stress formulation were firstly published by Tsukrov and Kachanov [126]. The theory is derived also for other special cases of inclusions such as circles and cracks with various orientations relatively to the orthotropy axes. The elliptic hole with the axes  $2a$  and  $2b$  is considered in the orthotropic matrix with the orientation axes  $\mathbf{x}_1$  and  $\mathbf{x}_2$  as it is presented in Fig. 4.2. The compliance tensor of the solid with elliptical holes is considered as a sum of the compliance tensor of a matrix material and the compliance tensor of the hole  $\mathbb{H} = \mathbb{H}^{\text{matrix}} + \mathbb{H}^{\text{hole}}$ . The axes, defining the orientation of the hole in the matrix, are located along the hole axes and denoted as  $\mathbf{t}$  and  $\mathbf{n}$ . The hole compliance tensor is

derived as follows:

$$\begin{aligned}
H_{tttt} &= \frac{\pi b}{A} \left\{ \frac{a}{E_t^0} + b [C(1 - D \cos 2\varphi)] \right\}, \\
H_{tttn} &= \frac{\pi b}{4A} \left\{ a \left[ \frac{1}{E_2^0} - \frac{1}{E_1^0} - F \cos 2\varphi \right] + 2bCD \right\} \sin 2\varphi, \\
H_{ttnn} &= \frac{\pi ab}{4A} \left( F \sin^2 2\varphi - \frac{4}{\sqrt{E_1^0 E_2^0}} \right), \\
H_{tntn} &= \frac{\pi a^2}{4A} C(1 - D \cos 2\varphi) + \frac{\pi b^2}{4A} C(1 + D \cos 2\varphi) \\
&\quad + \frac{\pi ab}{4A} \left[ \left( \frac{1}{E_1^0} + \frac{1}{E_2^0} \right)^2 - F \cos^2 2\varphi \right], \\
H_{tnnn} &= \frac{\pi a}{4A} \left\{ 2aCD + b \left[ \frac{1}{E_2^0} - \frac{1}{E_1^0} + F \cos 2\varphi \right] \right\} \sin 2\varphi, \\
H_{nnnn} &= \frac{\pi a}{A} \left\{ a [C(1 + D \cos 2\varphi)] + \frac{b}{E_n^0} \right\}.
\end{aligned} \tag{4.4}$$

From the consideration that the cavities are growing on the grain boundary plane, we can assume that cavity axes coincide with the symmetry axes of the grain boundary region, so  $\varphi = 0^\circ$ . With this assumption the components of the compliance tensor  $H_{tttn}$  and  $H_{ttnn}$  are zero. The constants  $C$ ,  $D$  and  $F$  are expressed through the engineering constants of the matrix material in the following from:

$$\begin{aligned}
C &= \frac{1}{2} \frac{\sqrt{E_1^0} + \sqrt{E_2^0}}{\sqrt{E_1^0 E_2^0}} \sqrt{\frac{1}{G_{12}^0} - \frac{2\nu_{12}^0}{E_1^0} + \frac{2}{\sqrt{E_1^0 E_2^0}}}, \\
D &= \frac{\sqrt{E_1^0} - \sqrt{E_2^0}}{\sqrt{E_1^0} + \sqrt{E_2^0}}, \\
F &= \frac{1 + \nu_{12}^0}{E_1^0} + \frac{1 + \nu_{21}^0}{E_2^0} - \frac{1}{G_{12}^0}.
\end{aligned}$$

In the case when the void orientation coincides with the orientation of the matrix the Young's moduli in the following directions are equal  $E_t^0 = E_1^0$  and  $E_n^0 = E_2^0$ . The values of the engineering constants of the matrix  $E_1^0$ ,  $E_2^0$ ,  $G_{12}^0$ ,  $\nu_{12}^0$  and  $\nu_{21}^0$  are derived from the stiffness tensor components, calculated in Abaqus. The moduli  $\nu_{ij}^0$  characterize the transverse strain in the  $j$ th direction,

when the material is tensed in the  $i$ th direction. With the above mentioned assumptions the non-zero components of Eqs. (4.4) can be rewritten in the notations of matrix orthotropy axes in a following manner:

$$\begin{aligned}
 H_{1111} &= \frac{\pi b}{A} \left\{ \frac{a}{E_1^0} + b[C(1-D)] \right\}, \\
 H_{1122} &= -\frac{\pi ab}{A} \frac{1}{\sqrt{E_1^0 E_2^0}}, \\
 H_{1212} &= \frac{\pi a^2}{4A} C(1-D) + \frac{\pi b^2}{4A} C(1+D) + \frac{\pi ab}{4A} \left[ \left( \frac{1}{E_1^0} + \frac{1}{E_2^0} \right)^2 - F \right], \\
 H_{2222} &= \frac{\pi a}{A} \left\{ a[C(1+D)] + \frac{b}{E_2^0} \right\}.
 \end{aligned} \tag{4.5}$$

The parameter  $A$  is the representative area and is set phenomenologically in the current research.

In the chosen cavity growth model of Tvergaard [127] the spherical-cap cavity is considered. From the geometrical considerations the cavity high  $b$  can be derived as follows:

$$b = a \frac{1 - \cos \psi}{\sin \psi}.$$

In the current research the difference between the geometry of the spherical-cup and elliptical cavity is neglected. The inaccuracy related to this assumption is considered in the set of parameter  $A$ .



---

## Numerical implementation

In the current chapter details of the numerical implementation of the problem, stated in previous chapters, are given. An overview of possible geometrical representations of polycrystalline materials is presented. Voronoi tessellation algorithm is chosen to generate random grain cores of the three dimensional polycrystal. Based on that approach, the algorithm of unit cell construction is described. Details of the user defined material behavior implementation in Abaqus are discussed as well as the procedure of averaging of stress and strain fields within the unit cell. With the help of elaborated procedure a statistical analysis of the unit cell is performed in dependence on number of grains, randomness of geometry, etc.

### 5.1 Geometrical representation of polycrystal

An overview of the current state of art in the polycrystalline microstructure modeling is given, in [96, 118] among others. Some very simplified models represent two dimensional grain geometry by arrays of hexagons [128] and hexagons with additional grain boundary elements [101]. In [48] three dimensional array of truncated octahedrons is used to represent large array of polycrystal.

Other more complex models present microstructure of polycrystalline materials by Voronoi tessellation with a random distribution of grain cores and random grain shapes. For two dimensional problems planar Voronoi tessellation is used. Description of the idea of planar Voronoi tessellation is given, for example, in [74, 75]. An example of a three dimensional grain unit

cell, constructed with the help of Voronoi tessellation, is described in [41]. In [88] zircaloy material is simulated by means of two and three dimensional Voronoi tessellation. Additionally, an improved algorithm with repulsion distance is used in order to control minimum grain size and to obtain regular grain size distribution within the unit cell. Grain boundaries are constructed with an additional element layer on the surface of grains. Additional grain boundary elements are used to represent transgranular cracking of zircaloy. In [30] an analogous polycrystalline unit cell is meshed with the special program, allowing the regular and free space meshing. Influence of finite element type and size on the unit cell response are discussed within the work. In [96] a rectangular region of the polycrystal is generated by packing of spherical particles of different volume. The number of particles of the specific volume is defined by the user. The particle packing is done by two different techniques, involving molecular dynamics and discrete element method. Both techniques generate interaction forces between particles, condensing them to the chosen simulated region. With the particles packing and subsequent space decomposition by interconnected polyhedrons with the help of Voronoi tessellation, a polycrystalline geometry is generated, consisting of grains, grain boundaries and interface regions. Above described geometry is used to represent a three dimensional polycrystal model of the dual phase steel.

Most advanced models [118] deal with reproduction of real polycrystalline geometry, which is obtained by use of the X-ray diffraction contrast tomography. In addition to the realistic geometry information about grain orientations is also added. Despite their realistic polycrystal representations, such models require an unreasonable amount of computational costs.

Within the current work a Python script is developed, which allows to design an analogous unit cell in Abaqus. In the developed model the following input parameters are defined: number of grains, average grain size, material properties, and grain boundary thickness. Dimensions of the cells are calculated from grain size and grain number. Grain boundary thickness corresponds to the thickness of the plane, separating the neighboring grains. Figure 5.1a) shows an unit cell consisting of 50 grains with zero grain boundary thickness.

Planar defects between the grains, known as grain boundaries, occur due to lattices incompatibilities of the neighboring grains. This region, surrounding the connection of 2 grains, possesses a less ordered crystalline structure in comparison to the grain interior. A description of grain boundaries of the crystalline copper is given in [95]. Due to non-perfect

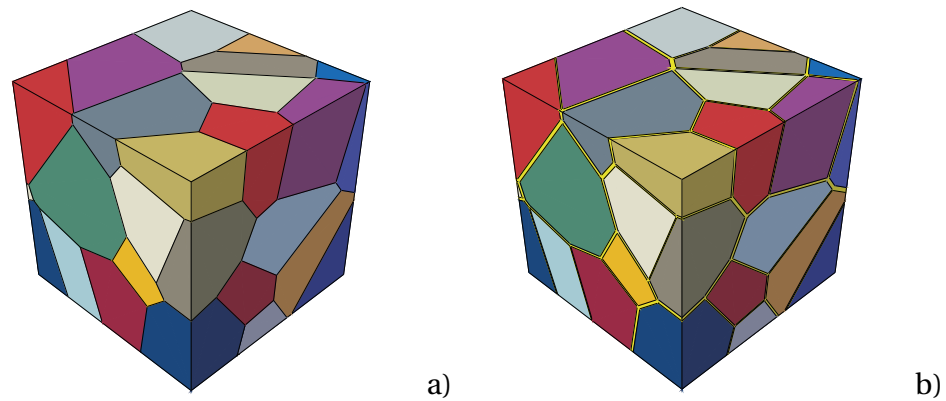


**Figure 5.1** Geometrical representation of a polycrystal: a) unit cell with zero grain boundary thickness; b) unit cell with non-zero grain boundary thickness

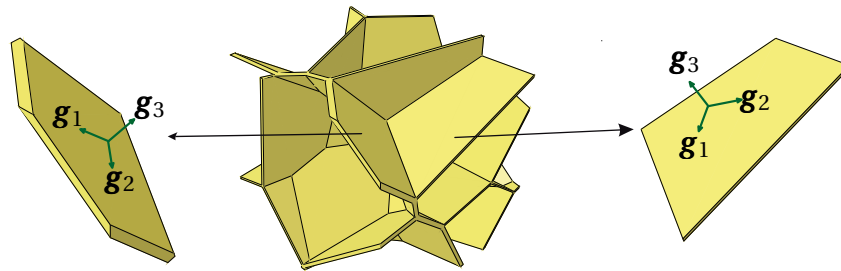


**Figure 5.2** Grain boundary region with discrete material orientation

arrangement of atoms in the vicinity of a grain boundary every atom in it occupies larger volume in comparison to perfect packing. Description of this phenomena requires introduction of a specific region, which possesses different behavior than grain interior. Its atomistic structure prescribes creep softer material behavior during creep. For this purpose a unit cell with grain boundary region is constructed (5.1b).

An important step in the simulation of the polycrystalline body is the set of material orientation. To this end local coordinate systems are used. In every grain local cartesian coordinates are specified, which are rotated by a random angle relatively to the global coordinate system of the unit cell. With this a random crystallographical orientation is reflected, which is naturally observed in a polycrystal. For the grain boundary sliding representation one should distinguish between the shear and the normal deformation of the grain boundary. Therefore an individual local coordinate system is determined for every plane of the grain boundary region. An example of such coordinate

system one can see in Fig. 5.2. In this case the direction  $\mathbf{g}_3$  is set as a normal to the grain boundary and the other two directions  $\mathbf{g}_1$  and  $\mathbf{g}_2$  lie in the grain boundary plane. In regions of grain boundary junctions smooth transition from one coordinate system to another is automatically performed by Abaqus.

## 5.2 Material model implementation

For the description of anisotropic creep in Abaqus/Standard Hill's potential function is utilized [52], allowing the description of the materials possessing different types of symmetry, including orthotropic as the highest one. Potential functions of Hill's type correspond to the yield criteria in the case of plasticity and are used to build the equivalent stress expression, defining flow stress limit in the case of creep. The micromechanically based damage model of Tvergaard [127] is not presented in the standard version of Abaqus and that is the reason to develop the user defined material behavior in the current research. The user defined material behavior in Abaqus enables a formulation of any constitutive law for the calculation of stresses, elastic and inelastic strains. The Abaqus interface for the UMAT (user material) subroutine requires to give the code in the programming language Fortran. Stresses at every iteration are calculated based on the explicit Euler integration scheme. This method is widely used for the creep analysis due to its simplicity. The stability of the method depends on the time step size, which should be limited by some critical value  $\Delta t_s$ . The time step size should be set manually in Abaqus/CAE for the whole analysis. Then the step size is calculated in the subroutine at every increment and compared with the set in Abaqus/CAE value. For the integration step the smallest one is chosen, what increase the numerical stability of the solution. In [1] the stability of the solution is proposed to be estimated by the criteria that the creep strain rate should not exceed the total elastic strain. The leading from this criteria formula has the look:

$$\Delta t_s = 0.5 \frac{1}{\dot{\epsilon}_{\text{eq}}^{\text{cr}}} \frac{\sigma_{\text{eq}}}{\bar{E}},$$

where  $\bar{E}$  is an effective elastic modulus and  $\sigma_{\text{eq}}$  is the von Mises equivalent stress, which in the current work is substituted by the expression for the equivalent stress of material with cubic symmetry (2.37) or orthotropic one (3.6). The effective elastic modulus  $\bar{E}$  is chosen from considerations of analysis stability for the general case of anisotropic material. In the current

work it is proposed as follows:

$$\bar{E} = 3\lambda_3 \frac{\lambda_3 + \lambda_1 - \lambda_2}{3\lambda_3 + 2\lambda_1 - 2\lambda_2}.$$

The values of material parameters  $\lambda_i$  are given in Table 7.1.

The represented unit cell consists of two phases: grain and grain boundary. The different material behavior should be assigned to each phase. At the same time the mechanical behavior of both phases should be written in one UMAT. The material model parameters, which are set in the Abaqus/CAE, prescribe whether orthotropic or cubic symmetry to the material. An additional material model parameter corresponding to possibility of damage evolution in the material is represented. The same parameter activates stiffness matrix reduction due to damage. Summary of features prescribed for the materials of the unit cell is given in Table 5.1. Solution-dependent variables STATEV are

**Table 5.1** Prescribed features to the unit cell's materials

| Feature                    | Grain interior material | Grain boundary material |
|----------------------------|-------------------------|-------------------------|
| Symmetry type              | cubic                   | orthotropic             |
| Damage evolution           | -                       | +                       |
| Stiffness matrix reduction | -                       | +                       |

used to store and update damage variables at every integration step.

### 5.3 Calculation of averaged fields in the unit cell

For the averaged fields calculation the subroutine UVARM is used. It is called by Abaqus at every iteration and executed parallel to the UMAT subroutine, which allows to decrease the solution time. In addition to decrease the postprocessing time the multithreading is used. The averaged fields of stresses and strains within the unit cells are calculated by involving the simple rule:

$$\bar{\sigma} = \frac{1}{V} \int_V \sigma dV,$$

$$\bar{\epsilon} = \frac{1}{V} \int_V \epsilon dV,$$

where the bar quantities are averaged values within the grains, grain boundary region or the whole unit cell's volume. Before the averaging the creep, the total

strain tensor and the stress tensor is rotated to the global coordinate system. It is done by involving the routine ROTSIG, which performs the multiplication of stress and strain tensor with an orientation tensor. Following this procedure the next averaged quantities are obtained:

- creep strain tensor components;
- total strain tensor components;
- stress tensor components;
- creep strain and stress tensor components, averaged within the grains;
- creep strain and stress tensor components, averaged within the grain boundary region;
- value of the equivalent stress, averaged within the whole unit cell (grains and grain boundary region).

The obtained values are printed to the file for the consequent processing and visualization of the results.

## 5.4 Statistical analysis of the unit cell

The unit cell with the grains of random geometry and random orientation is used to represent a material point of the macromaterial, considered on the microlevel. For correct prediction of the material macroproperties the response of the unit cell should be as much as possible independent of geometrical features of a certain realization. In order to consider an averaged response of the unit cell as a representative one, dependence on the number of grains, the element size and the model parameters should be studied.

The first validation criteria is the scatter of the averaged creep strain within the unit cells with completely identical material parameters. For this purpose 55 realizations of the unit cell with zero grain boundary thickness, consisting of 40 grains, are built. Taking into account that the grain boundary thickness is set as zero only the grain material is presented in the unit cell. The aim of the current analysis not the investigation of mechanical behavior of the real material, but the investigation of the influence of the grains geometry and orientations on the averaged creep response of the unit cell. That is why the model parameters for some abstract material with the cubic symmetry are taken as follows:

$$\lambda_1 = 410 \text{ GPa}, \quad \lambda_2 = 47 \text{ GPa}, \quad \lambda_3 = 150 \text{ GPa},$$

$$a = 8.928 \cdot 10^{-12} \frac{(\text{MPa})^{-n}}{\text{s}}, \quad n = 5.69, \quad \xi = 0.05.$$

The obtained unit cells are tested under applied tensile pressure of 52 MPa during 100 hours. With the help of UVARM subroutine the averaged creep strain field is calculated. The creep strain in the loading direction for the every 55 realizations is presented in Fig. 5.3.

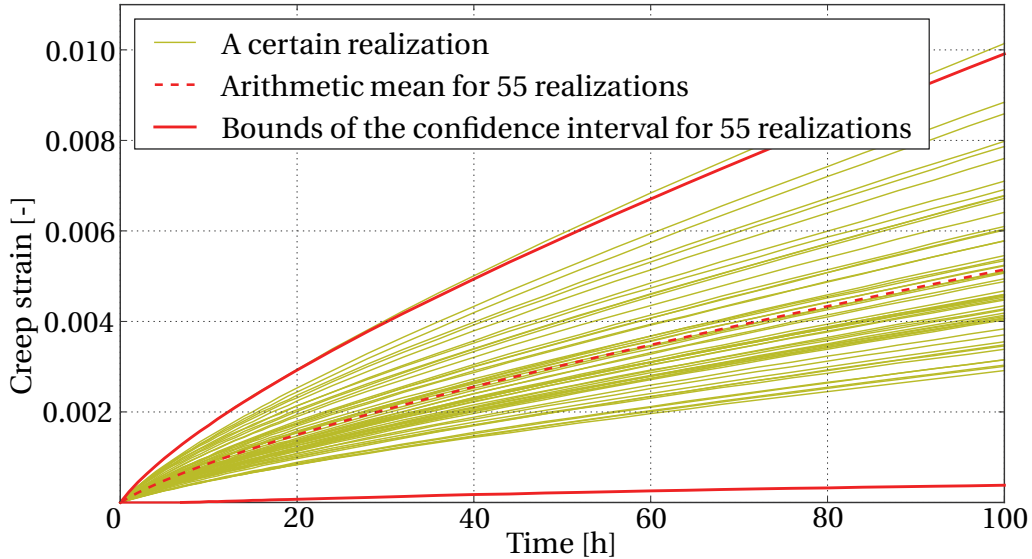


**Figure 5.3** Creep curves scatter for 55 realizations of the unit cells

To evaluate the scatter of creep curves the arithmetic mean and bounds of the confidence interval are calculated with involving the well known formulas of probability theory. The standard deviation  $\sigma$  under assumption of normal (Gaussian) distribution is determined as follows:

$$\sigma = \sqrt{\sum_{i=0}^n (X_i - X^*)^2 / n},$$

where  $n$  is the number of samples,  $X_i$  is the value of a certain random variable.  $X^*$  is the arithmetic mean:

$$X^* = \sum_{i=0}^n X_i / n.$$

According to the rule of 'three sigma' for the random variable [134], the probability that the random realization lies outside of the three standard deviations from the expectation value is significantly smaller than 1/9. For example, for the random values, distributed by the normal law, this probability equals to 0.0027. This rule is widely applicable for the cases, where

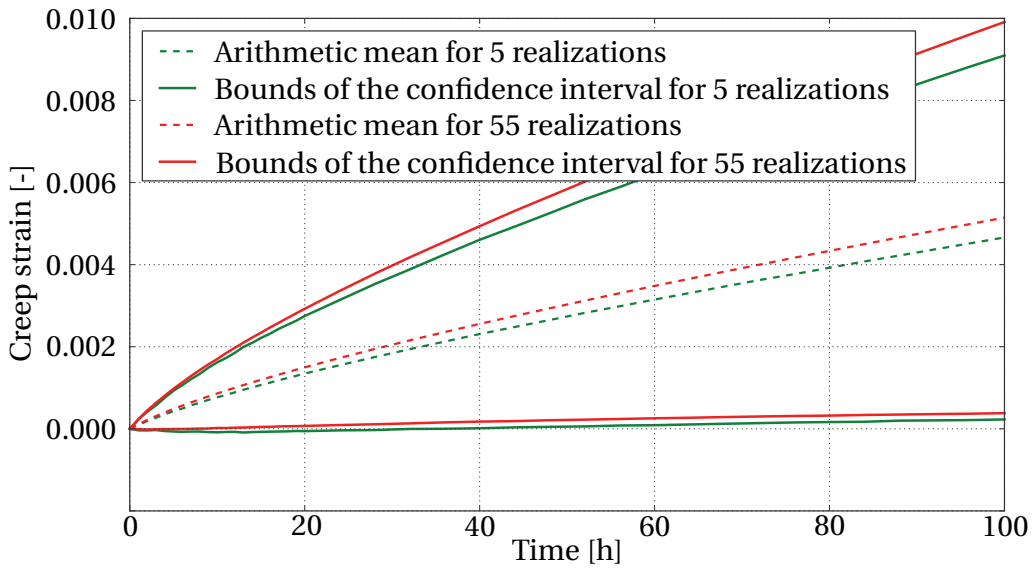


**Figure 5.4** Creep curves scatter for 55 realizations of the unit cells

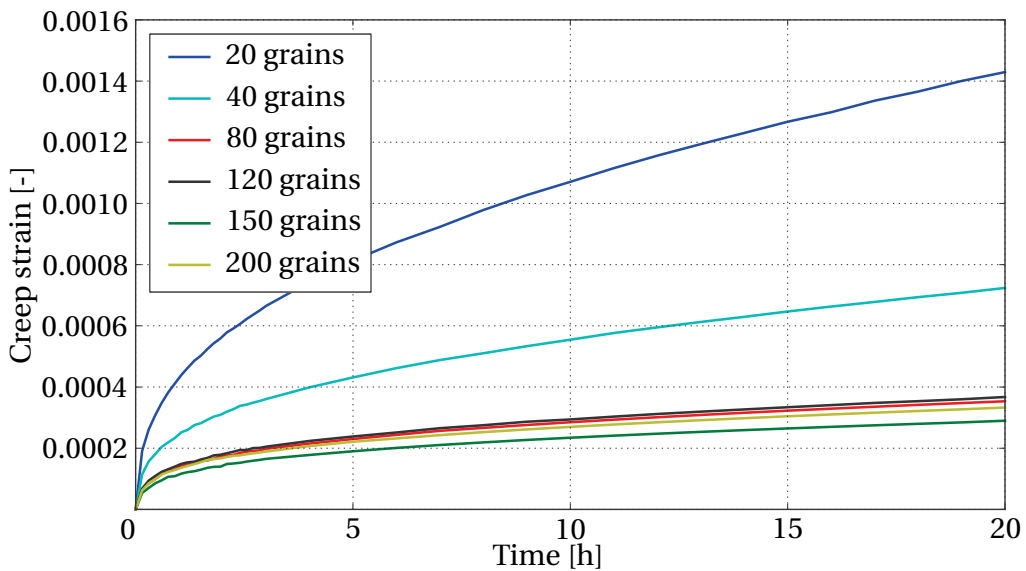


**Figure 5.5** Arithmetic mean of creep strain for unit cells with different number of grains

the law of the random value distribution is unknown and only the expectation value and the standard deviation are known. According to this rule we take the confidence interval equal  $3\sigma$  from the both sides of the arithmetic mean value.

The creep tests of 55 realizations of the unit cell require a lot of computational effort. If we accept the mean value of certain number of

realizations as a representative one, the analysis of the dependence on the certain model parameter demands number of parameters meaning  $\times$  number of realizations of the unit cell, which can be a huge number. To optimize this value additional 5 realizations are generated and their mean value and bounds of confidence interval are compared with those for 55 realizations.

In Fig. 5.4 one can see that the confidence intervals for 5 and 55 realizations lie very close. From Fig. 5.3 one can notice that the lower bound of the confidence interval almost two times overestimate the deviation from the averaged value. Therefore the relative error only between the upper bounds of the confidence intervals is estimated and it does not exceed 10%. Thus, for the further analysis, we can take 5 realizations as acceptable value for statistical representation.

## 5.5 Choice of the representative number of grains

In the real polycrystalline microstructure the grain boundaries play the role of defects, holding back the slip between the neighboring grains. Within the simulation under equal applied stress on the unit cell, the level of deformation in it will be different in dependence on the number of such planar defects. Thus, the unit cell with 10 grains possesses much less grain boundaries as that one consisting of 100. As a consequence the deformation field in the unit cell with 10 grains is much higher. The important task is to determine the saturated value of the grains number in a polycrystalline unit cell, where the obtained averaged strain field is not dependent on the grain number. The unit cells with the number of grains in range from 20 to 200 are tested under constant tensile stress of 40 MPa during 20 hours. The grain size is set equal to 0.21 mm. The following material parameters are used:

$$\lambda_1 = 374 \text{ GPa}, \quad \lambda_2 = 37 \text{ GPa}, \quad \lambda_3 = 125 \text{ GPa},$$

$$a = 1.96 \cdot 10^{-15} \frac{(\text{MPa})^{-n}}{\text{s}}, \quad n = 9.4, \quad \xi = 0.026.$$

The material model parameters are set from the same considerations as in previous section. For every number of grains 5 realizations of the unit cell are built. The arithmetic means of the averaged creep curves for every 5 realizations are calculated. The scatter of the obtained curves is shown in Fig. 5.5.

As one can see from the represented graph, the tendency of decrease of the averaged creep strain with the increase of the number of grains is held for the unit cells consisting of less than 80 grains. Starting from this number the

averaged creep curves are fluctuating in the narrow interval. The conclusion arises, that 80 is a minimum representative number of grains in the unit cell.

## 5.6 Choice of the grain boundary region thickness

The grain boundary region in the current model is responsible for the grain boundary sliding modeling (see Sect. 3.2). The thickness of this region is a pure phenomenological value and should be chosen from the numerical considerations. For this purpose the unit cells with different values of grain boundary thickness should be tested. In the developed Python code the possibility to rebuild the Voronoi tessellation with the same number and shape of grains, but different value of the grain boundary thickness is included. With this we can investigate the pure dependence on the grain boundary thickness without construction of many realizations. In Fig. 5.6 the normalized creep curves of the unit cell consisting of 80 grains with different thickness of the grain boundary is represented. The averaged creep strains are normalized to the elastic strain.

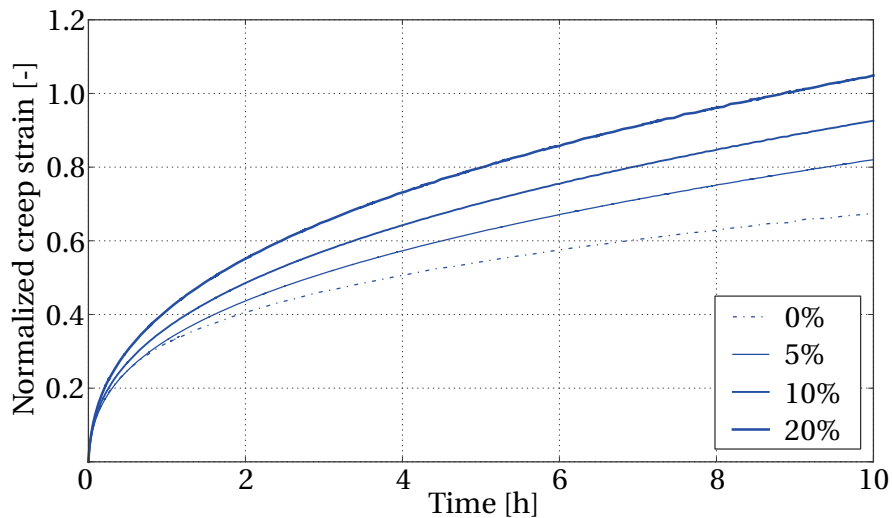


**Figure 5.6** Normalized creep curves for unit cell with different grain boundary thickness

As far as to the grain boundary region the much softer creep behavior as to the grain interior material is prescribed, the overall response of the unit cell will be softer with the increase of the grain boundary thickness. The grain boundary region is a complex geometrical structure and can be meshed only with tetragonal finite elements. And as smaller the width of this

region, then the more distorted elements would be generated, especially in the junction zones. The presence of such elements will lead to the problems with convergence of analysis and will lead to the significant increase of the computational time. From these reasons it is recommended to set the grain boundary thickness value higher than 5% of the grain boundary size.



---

## Tensile creep tests for polycrystalline copper at 550 °C

In the following chapter the analysis of the experimental data carried out under polycrystalline copper at 550 °C is provided. The experimentally obtained data are compared with the other creep data available in the literature. The temperature choice is conditioned by the previously used experimental data on single crystal copper [132]. The procedure of the experimental creep test is presented and the description of the inelastic strains measurement is discussed. The aim of the following chapter is to observe the described in the model mechanisms and to investigate their influence on the resulting creep curve.

### 6.1 Choice of the specimen and test conditions

The uniaxial tensile creep tests under polycrystalline copper are performed in the creep laboratory of the Mechanical Engineering Department at the Politecnico di Milano (Italy). Experimental tests are carried out in air, under constant load conditions on two classical lever–arm machines and on a computer load controlled machine, designed for creep tests. The load in the lever–arm machine is applied by means of weights, connected with the specimen holder by the system of levers (see Fig. 6.1a). The minimum possible applied load is limited by the weight of the platform, holding the weights. By this reason low stress tests, notably below the 10 MPa limit, are performed on the computer–controlled tensile testing machine. This type of machine is shown in Fig. 6.1b). The cylindrical specimens with the gauge diameter 6 mm and gauge length 30 mm were machined from Electrolytic–

Tough-Pitch (ETP) polycrystalline copper of 99.9% purity with the P content lower than 0.03%. The machined specimens are supplied as end items. This is the reason of the lack of information about the material processing and specimen's manufacturing. Drawing of the specimen, of the standard ridged type for the placement at the extensometer system, is presented in Fig. 6.2.

The magnitude of the applied stress is ranged between 4.8 and 30 MPa in order to obtain the creep curves in the region of the diffusion and power law creep, to have the possibility of comparison with the other experimental data, presented in the literature [137], and to obtain the rupture times in the wide range of stresses.

## 6.2 Experimental procedure

The procedure of the creep test is elaborated in accordance to EN ISO 204:2009 standard [20], taking into account ECCC (European Creep Collaborative Committee)<sup>1</sup> recommendations to obtain the comparable data through the experiments of the similar class. For every specimen the measurements of the actual diameter and the gauge length are made before the testing, they are kept as initial values for the further calculations of the initial stress, applied load, strain and ductility indices: elongation and reduction of area at rupture.

To measure the elongation of the specimen contact type extensometers, designed for high temperature creep testing, are used. The displacement between ridge can be read by a couple of Linear Variable Differential Transformers (LVDT) placed at the expound end of the extensometer system. The strain is then calculated on the basis of the average of the displacement records (i.e. average change of length of specimen gauge length). The actual temperature of the specimen is controlled with the 3 S-type thermocouples, directly placed on the bottom, middle and top parts with the help of special tins (see Fig. 6.1c)). The single wire thermocouples made of the Pt/Pt-10%Rh alloy are used. The sensitivity of these thermocouples is low, therefore their preferential application lies rather in the high temperature range. The detected variation of temperature during the test does not exceed 1%. After attaching the thermocouples and extensometers to the specimen it is screwed into the holders of the loading machine and the test can be started.

The possible presence of bending (to be kept < 20%) is checked by means of loading-unloading cycle carried at room temperature before heating at the beginning of the test. The stress magnitude should be well below the yield

---

<sup>1</sup><http://www.ommi.co.uk/etd/eccc/>



rate. At the end of the test the plastic strains are analyzed.

### 6.3 Experimental results

In total 12 specimens are tested until rupture, the life time is varying from 1 to 220 hours. The minimum creep strain rates corresponding to the applied stresses are reported in Table 6.1.

The set of creep curves for the stress level from 10 to 30 MPa are depicted in terms of creep strain rate vs. creep strain, Fig. 6.3. At several stress levels, for example, 10 MPa and 30 MPa no evident primary creep stage is observed.

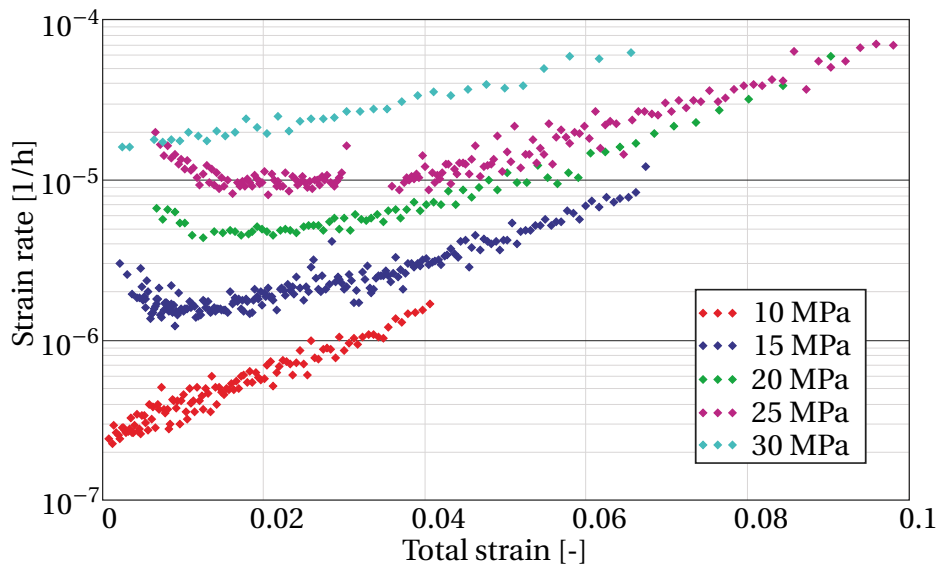


**Figure 6.3** Experimental creep curves of copper tested at 550 °C at different stresses

### 6.4 Validation of the secondary creep stage

The comparison of the experimental data with the data of Wilshire and Palmer [137], obtained for the pure copper with the grain size of 30  $\mu\text{m}$  at the temperatures 450 and 455 °C is presented. To avoid the temperature dependence and to follow the pure influence of the minimum creep strain rate on the applied stress the Arrhenius normalization rule is used. The normalized coefficients are determined as follows:

$$\dot{\varepsilon}^{\text{cr}} = a_0 \exp\left(-\frac{Q}{RT}\right) \left(\frac{\sigma}{G}\right)^n = \exp\left(-\frac{\alpha}{T}\right) \left(\frac{\sigma}{G}\right)^n, \quad (6.1)$$

**Table 6.1** Summarized data of the experimental creep tests, carried at 550 °C, showing the varying test parameters (applied stress,  $\sigma$ ) and creep test results (minimum creep strain rate,  $\dot{\epsilon}^{\text{cr}}$  and time to rupture,  $t_r$ )

| Specimen | $\sigma$ , MPa | $\dot{\epsilon}^{\text{cr}}$ , s <sup>-1</sup> | $t_r$ , h |
|----------|----------------|--|-----------|
| 1        | 4.8            | $1.04 \times 10^{-8}$                          | 220       |
| 2        | 5              | $3.61 \times 10^{-8}$                          | 166       |
| 3        | 10             | $2.78 \times 10^{-7}$                          | 20        |
| 4        | 10             | $8.89 \times 10^{-7}$                          | 20        |
| 5        | 10             | $3.22 \times 10^{-7}$                          | 30        |
| 6        | 15             | $6.62 \times 10^{-5}$                          | 0.4       |
| 7        | 15             | $1.22 \times 10^{-7}$                          | 9         |
| 8        | 15             | $1.79 \times 10^{-6}$                          | 7         |
| 9        | 20             | $4.44 \times 10^{-6}$                          | 3         |
| 10       | 25             | $1.01 \times 10^{-5}$                          | 2         |
| 11       | 30             | $1.39 \times 10^{-5}$                          | 0.72      |
| 12       | 30             | $1.82 \times 10^{-5}$                          | 0.67      |

where  $Q$  is the activation energy,  $R$  is the Boltzmann constant and  $T$  is the reference temperature.

The parameter  $\alpha$  is defined from the literature [137] and experimental creep strain rate data at the same stress and different temperature levels. Equation (6.1) in this case can be rewritten in the following manner:

$$\dot{\epsilon}_1^{\text{cr}} = f_1(T_1)f_2(\sigma_0),$$

$$\dot{\epsilon}_2^{\text{cr}} = f_1(T_2)f_2(\sigma_0).$$

After some algebra:

$$\frac{\dot{\epsilon}_1^{\text{cr}}}{f_1(T_1)} = \frac{\dot{\epsilon}_2^{\text{cr}}}{f_1(T_2)},$$

$$\frac{\dot{\epsilon}_1^{\text{cr}}}{\dot{\epsilon}_2^{\text{cr}}} = \frac{f_1(T_1)}{f_1(T_2)} = \frac{\exp\left(-\frac{\alpha}{T_1}\right)}{\exp\left(-\frac{\alpha}{T_2}\right)} = \exp\left(-\alpha\left(\frac{1}{T_1} - \frac{1}{T_2}\right)\right),$$

one can obtain

$$\alpha = -\frac{\ln(\dot{\epsilon}_1^{\text{cr}}/\dot{\epsilon}_2^{\text{cr}})}{\frac{1}{T_1} - \frac{1}{T_2}}.$$

The values of the shear modulus  $G$  used to normalize the applied stress levels are taken from the work of Chang and Himmel [26]. To get the values of

the shear modulus corresponding to the necessary temperature levels, linear interpolation of data [26] is used. The values are provided below:

$$G_{450} = 64388 \text{ MPa}, \quad G_{455} = 64252 \text{ MPa}, \quad G_{550} = 61676 \text{ MPa}.$$

Experimental (see Table 6.1) and literature creep data, normalized either in terms of strain rate and of stress, are presented in Fig. 6.4. As one can see, the normalized creep strain rate, obtained from the experimental tests, shows good agreement with the data, published by Wilshire and Palmer [137]. A progressive reduction of the slope with the applied stress can be observed. This could be correlated to a change in the creep strain mechanism from dislocation to diffusion as assumed by Wilshire and Palmer [137].

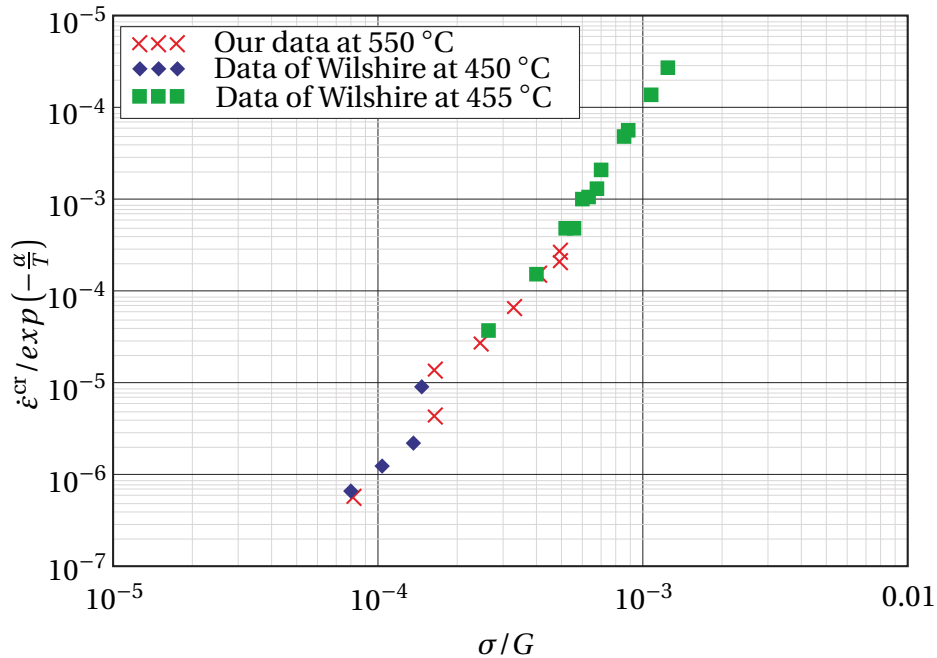


**Figure 6.4** Normalized minimum creep strain rate vs. normalized stress

## 6.5 Micrographs of copper under different applied stresses

In order to check the creep damage type for the experimentally measured microstructure and to observe its evolution during creep testing, the gauge length of crept samples is longitudinally cut for metallographic observations. The slices are prepared in uniform manner so that it is possible to acquire

the comparable micrographs. The preliminarily polished specimens are immersed in the etching solution for 5 seconds. The solution composition is 50 ml of HCl, 5 g of FeCl<sub>3</sub> and 100 ml of H<sub>2</sub>O.

The micrographs<sup>2</sup> of the specimens in initial state and after testing under 10 and 30 MPa are presented in Figs. 6.5, 6.6, 6.7 at 200x magnification. Additional micrographs at lower magnification 50 and 100x are given in Appendix B. The micrographs at lower magnification show the homogeneity of the material features either before and after creep.

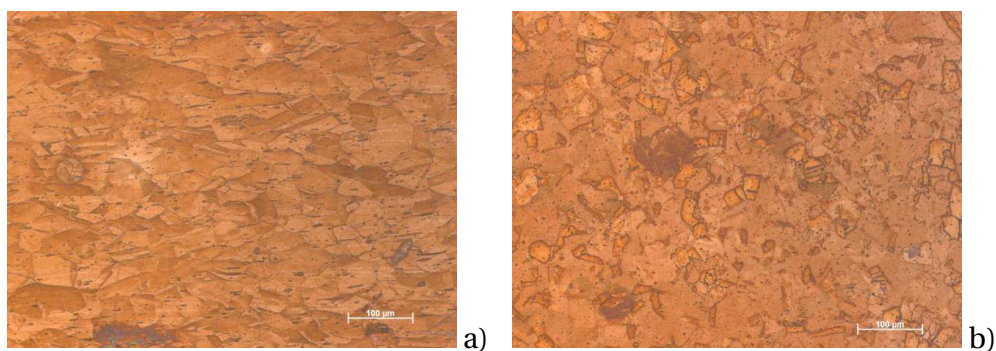


**Figure 6.5** Micrographs of the specimen in the initial state (original magnification 200x): a) longitudinal section; b) cross-section

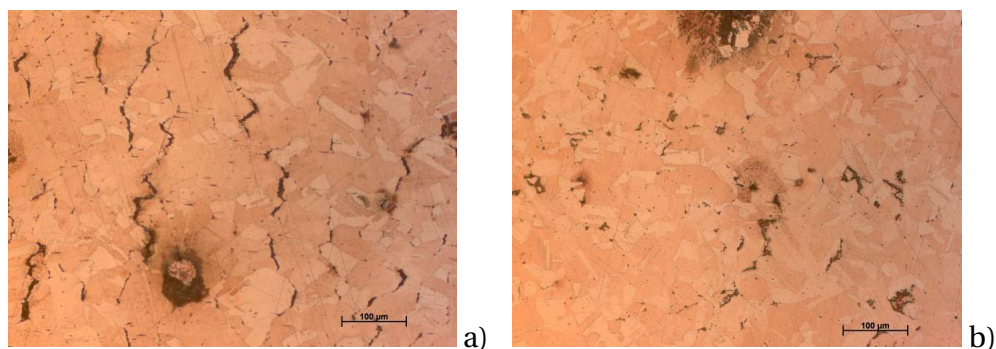


**Figure 6.6** Micrographs of the specimen 11, tested 1 hour at 30 MPa (original magnification 200x): a) longitudinal section; b) cross-section

---

<sup>2</sup>The micrographs of slices are made at the Institute of Materials and Joining Technology at the Otto-von-Guericke-University Magdeburg

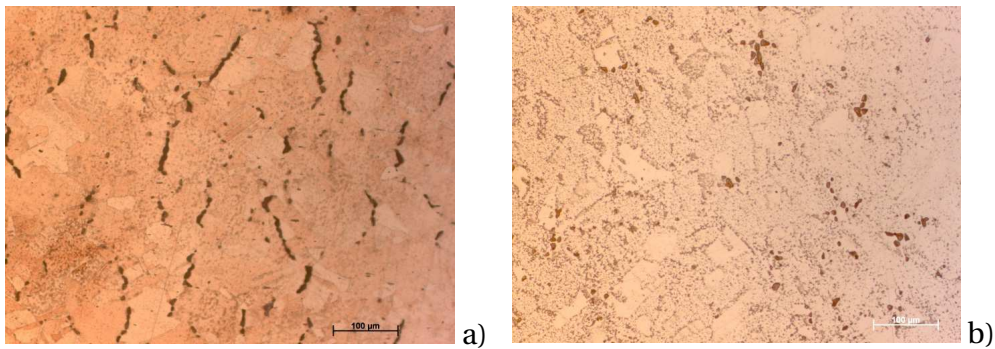


**Figure 6.7** Micrographs of the specimen 4, tested 20 hours at 10 MPa (original magnification 200x): a) longitudinal section; b) cross-section

On the micrographs of the material in initial state (see Fig. 6.5) one can observe grains of elongated shape, which indicates the possibility that the material was not annealed before the machining. As it is known from the literature the annealing of cold-worked parts causes grain recrystallization, leading to the grain size refinement and decrease of material anisotropy [64].

The loading direction, parallel to that of elongated grains, is horizontal in the micrographs. The evident cavitation of the grain boundaries orthogonal to the maximum tensile stress is noticed. In Figs. 6.6a) and 6.7a) one can see the perceptible difference in the damage. In both cases damage is manifested by the cavitation of the grain boundaries, but the size of cavities and the occupation of the surface of the micrograph manifest some distinctions. On the micrograph of the specimen, tested at 10 MPa (see Fig. 6.7a)) the large number of single cavities is evidently presented. At the same time some grain boundaries already possess micro cracks. The edges of the microcracks are rounded, with the discernible shape of former microcavities. Such microstructure of damage is characteristic for the active diffusion. On the micrograph of the specimen, tested at 30 MPa (see Fig. 6.6a)), one can observe the microcracks with already sharper edges and the lower number of single cavities. Such microstructure of damage is characteristic for the power law creep mechanism. The same tendency one can follow at lower magnifications (see Figs. B.3a), B.4a), B.5a), B.6a)).

---

## Model application

In the current chapter analysis of the averaged creep curve of the unit cell is performed. The influence of the represented in the model micromechanisms on the creep curve regions is investigated. In addition, the description of the existing tests under non-proportional loading is given. The possibilities of their modeling by means of the phenomenological continuum damage models are presented. For this purpose the short introduction to continuum damage theory is given. The results of non-proportional loading simulation with the unit cell model are given and discussed.

### 7.1 Verification of the model by the separate creep region

The purpose of the current section is to bring in correspondence the phenomenological creep curve micromechanical processes, exerting influence on it. The current model is constructed in such a way, that certain micromechanism corresponds to a set of material parameters. Some of them have direct physical meaning and the other one should be set, in dependence on their contribution to the averaged creep curve of the macromaterial.

#### 7.1.1 Primary creep stage validation

At the beginning of the creep deformation process the rearrangement of the dislocations occurs within the material of the single grain, leading to subgrains' formation. The material model parameter  $\xi$ , which is included in

the expression for the equivalent stress (2.37) and creep strain rate (2.36) for the material with the cubic symmetry case, represents the level of anisotropy of the single crystal material. If one assumes this parameter equal to 1, the above mentioned equations reduce to the isotropic case and the unit cell, consisting of grains made of such material, gives the homogeneous material response. In other words the interaction between the grains is ignored. To the  $\xi = 1$  case corresponds the highest creep curve in Fig. 7.1a), showing the linear dependence on time.

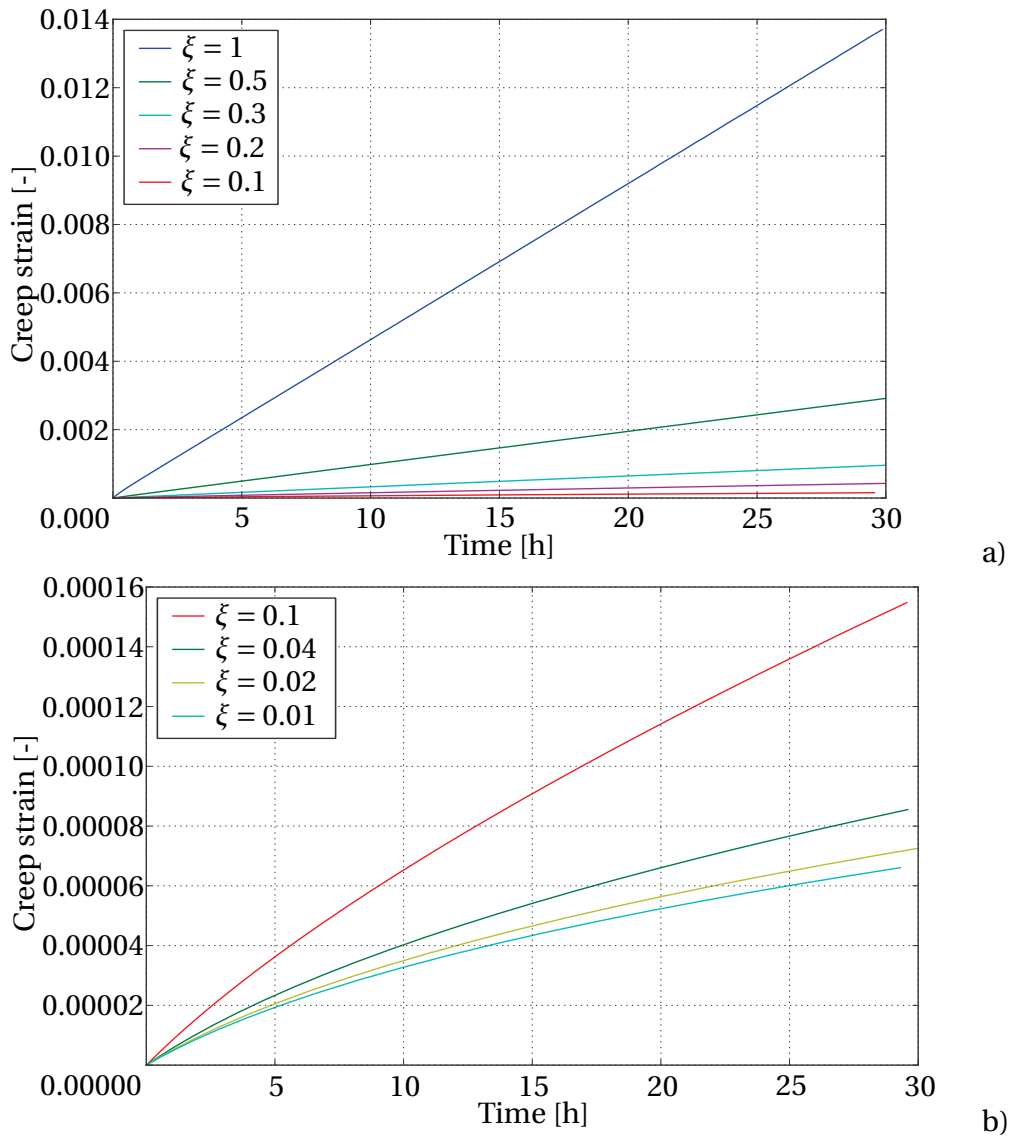


**Figure 7.1** Averaged creep strain variation with the change of  $\xi$  parameter: a)  $\xi = 0.1 - 1$ ; b)  $\xi = 0.01 - 0.1$

In the diagram are presented the averaged creep strains in the loading direction of the unit cells, numerically tested under tension of 52 MPa during 30 hours. All material model parameters are kept the same except  $\xi$ . With the decrease of the  $\xi$  value the strain level also decreases. It is caused by the fact that the material orientation becomes essential and some regions of the unit cell get less preferential orientation to the applied stress. Nevertheless until the  $\xi$  value approaches 0.1 the influence of the material orientation is not enough to cause the hardening in the averaged response of the unit cell. In Fig. 7.1b) one can see the variation of the averaged creep strain for the parameter  $\xi$  below 0.01. Such level of the anisotropy in grains leads to strain level decrease into 2 orders in comparison to the isotropic grain properties. With this the creep curves show the evident hardening and the primary creep stage. Thus the value of  $\xi$  parameter should be chosen in the range from 0.1 till 0.01, the lower value leads to problems with convergence.

### 7.1.2 Secondary creep stage verification

The group of user defined material model parameters of the grain boundary region, which can influence the secondary creep stage are the grain boundary thickness and the parameters  $\mu_1$ ,  $\mu_2$  and  $\mu_3$  related to the definition of the creep strain rate for the material with orthotropic symmetry, presented in Eq. (3.8). The model verification with respect to the grain boundary thickness is presented in Sect. 5.6. In the following subsection the influence of the grain boundary region parameters  $\mu_1$ ,  $\mu_2$  and  $\mu_3$  on the averaged creep curve of the unit cell is investigated.

In the grain boundary region these parameters are used to vary the contribution of the normal strain to the total deformation. With this the material reveals the different stiffness in normal and tangential direction to the grain boundary.

Thus, the verification of the secondary creep stage consists in the definition of the material model parameters for the grain boundary region in order to represent the grain boundary sliding. The material model parameters from the point of view of the physical considerations and comparison with the experimental data [7].

The material parameters  $\mu_1$ ,  $\mu_2$  and  $\mu_3$  for the grain interior material are set to 1 in order to reduce Eq. (3.8) to the cubic symmetry case (see Eq. (3.11)).

According to the test, published in [7], the contribution of the sliding strain to the total strain in polycrystal is  $\sim 10\%$ . Thus, within the current simulation the response of the unit cell with the grain boundary region, should

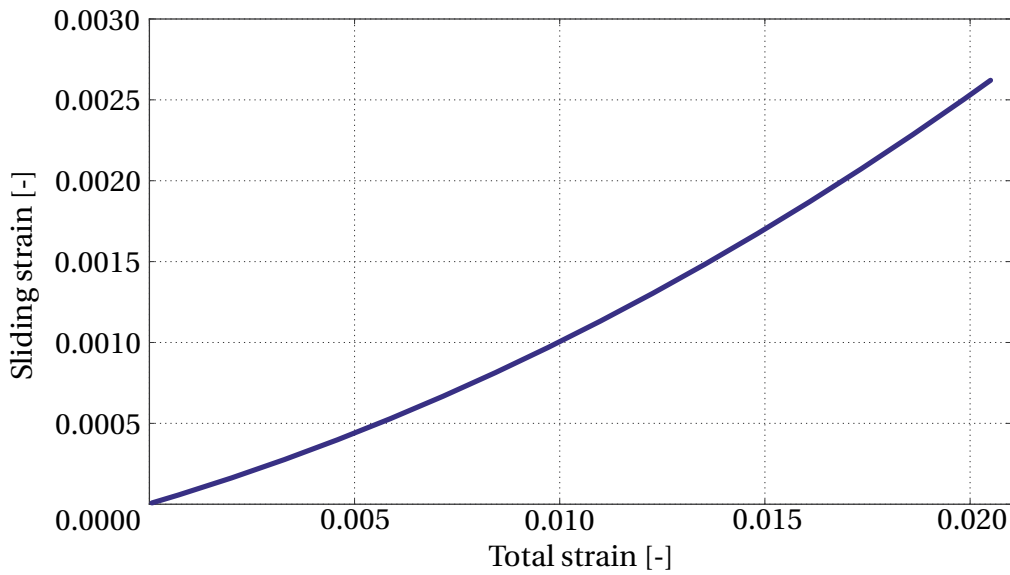


**Figure 7.2** Variation of the sliding strain and total strain in the unit cell consisting of 80 grains

be approximately 10% softer in comparison to the unit cell without the grain boundary region. In order to represent the dependence between the sliding strain and the total strain, two unit cells with the identical number, geometry and orientation of grains are constructed. The sliding strain is calculated as the difference between the averaged total strain of the unit cells with and without grain boundary region. In Fig. 7.2 one can see the relation of the sliding strain to the total strain for the unit cells with the material parameter set, presented in Table 7.1.

In addition, the local stresses concentrations are observed in the grain boundary region after creep testing. These stress peaks act as the driving forces for the creep cavity growth. The observed during simulation phenomena is consistent with the experimental observations in [7].

### 7.1.3 Tertiary creep stage verification

For the tertiary creep stage description the cavitation model of Tvergaard and the stiffness matrix reduction models are involved, described in Chapter 4. The driving force for the cavity growth is the normal stress, acting on the grain boundary. In order to verify the stress redistribution between the grain interior and the grain boundary region two identical models with different material parameters for the grain interior, responsible for the softer and harder behavior, are tested. The material parameters are set according to

**Table 7.1** Material model parameters

| Parameter                      | Grain interior     | Grain boundary    |
|--------------------------------|--------------------|-------------------|
| $\lambda_1$ , GPa              | 374                | 600               |
| $\lambda_2$ , GPa              | 37                 | 37                |
| $\lambda_3$ , GPa              | 125                | 125               |
| $A$ , (MPa) $^{-n}$ /s         | $4 \cdot 10^{-15}$ | $6 \cdot 10^{-8}$ |
| $n$                            | 9.4                | 4                 |
| $\mu_1, \mu_2, \mu_3$          | 1                  | 0.2               |
| $\mu_{12}, \mu_{23}, \mu_{13}$ | 0.2                | 0.3               |

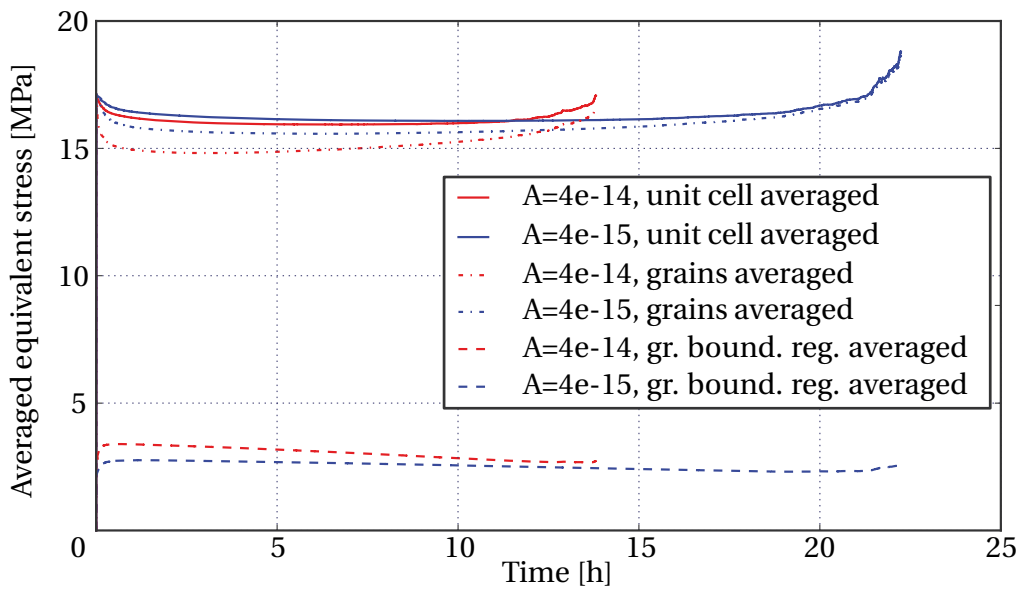
**Figure 7.3** Equivalent stress variation with time for the unit cells with the different creep constant  $A$  of the grain interior

Table 7.1. The different creep behavior of the grain interior is varied by change of the creep parameter  $A$  for the correspondent region. The resulting equivalent stresses redistribution one can see in Fig. 7.3.

On the diagram the evolution of the averaged value of the equivalent stress (see Eq. (3.6)) with time within the unit cell, grains and grain boundary region is presented. As one can see the averaged level of the equivalent stress within the unit cell is almost equal for the analysis, which is consistent with the equilibrium condition. But the averaged stresses redistribution within the grains and the grain boundary region is different. The unit cell with softer creep behavior reveals smaller stress level in comparison to the harder

unit cell. This leads to higher stresses accumulation in the grain boundary region and faster tertiary stage initiation. In addition, one can consider the equivalent stress drop within the grain boundary region after approximately the half of the deformation time which corresponds to the creep strain rate increase due to the damage accumulation in the material.

## 7.2 Non-proportional loading test

### 7.2.1 Continuum damage mechanics approach

#### 7.2.1.1 Isotropic damage

Despite the creep fracture modeling on the level of grains is performed, where the damage variable has a direct physical nature, an overview on the possible ways of the continuum creep damage representation for the sake of completeness, is given. In many textbooks and articles, one can find an extended overview and comparison of the models, for example in [71, 80, 85, 89, 119]. The damage variable is introduced to present the increase of the creep strain rate, denoting the tertiary creep stage. The continuum damage theories, representing damage through the scalar parameter are called isotropic damage theories. Such theories are applicable under assumptions of constant loading and material isotropy.

First Kachanov [58] represents damage as the scalar variable, developing in time by the following law:

$$\dot{\psi} = -B \left( \frac{\sigma_{\max}}{\psi} \right)^\kappa,$$

where  $B$  and  $\kappa$  are material parameters and  $\sigma_{\max}$  is the maximum tensile stress, acting at the body point. According to this definition the initial material state condition is  $\psi = 1$  and the fracture condition  $\psi = 0$ . The variable  $\psi$  itself is named continuity.

This idea was evolved by Rabotnov [109]. The damage parameter  $\omega$  is now defined as follows:

$$\omega = 1 - \psi.$$

The damage evolution equation depends on the applied stress and the accumulated level of damage:

$$\dot{\omega} = \frac{B\sigma^\kappa}{(1-\omega)^\mu}. \quad (7.1)$$

Rabotnov supplements this equation with the creep strain rate evolution equation for the uniaxial loading case in the following form:

$$\dot{\epsilon}^{\text{cr}} = \frac{A\sigma^k}{(1-\omega)^m}, \quad (7.2)$$

where  $A$ ,  $m$ ,  $n$  and  $\mu$  are additional material parameters. Equation (7.2) corresponds to the power law creep for undamaged material ( $\omega = 0$ ). The author supposed that the applied stress and accumulated damage contribute to the creep strain rate with different power law exponents. Such a representation in some cases gives higher correspondence between the model and the experimental data, but leads to additional complications in the material parameters identification.

The Rabotnov parameter  $\omega$  is related to the reduction of cross-section area due to defects (voids, cracks). Following from this expression

$$S = \frac{\sigma}{(1-\omega)}$$

receives the meaning of the net stress, increasing with the decrease of the area, bearing the applied load. For the multiaxial loading case the model was extended by Leckie and Hayhurst [49, 70]. The stress state effect on the fracture within the phenomenological modeling is usually represented through the isochronous surface. This surface is obtained as the depiction of the loci of constant stress states, leading to the same times to fracture. The authors firstly represent the isochronous equi-damage surface for the multi-axial state of stress in the following manner:

$$\sigma^*(\boldsymbol{\sigma}) = \alpha\sigma_1 + \beta I_1(\boldsymbol{\sigma}) + (1 - \alpha - \beta)\sigma_{\text{vM}}, \quad (7.3)$$

where  $\sigma_1$  is the first principal stress,  $\sigma_{\text{vM}}$  is the von Mises equivalent stress (see Eq. (2.25)) and  $I_1$  is the first invariants of the stress tensor, defined as the hydrostatic stress:

$$I_1(\boldsymbol{\sigma}) = \text{tr}(\boldsymbol{\sigma}).$$

The material model parameters  $\alpha$  and  $\beta$  in Eq. (7.3) allow to distinguish between two types of rupture, which are inherent to metallic materials [49]. For example, the cavity growth in copper is governed by the maximum tensile stress, which corresponds to  $\alpha \rightarrow 1$ , at the same time for aluminium it is mostly affected by the effective stress. For some steels, which exhibit the mixed rupture mode, the certain combination of these parameters should be determined from the experiments fitting.

For the multiaxial stress state the creep strain rate tensor is proposed to have the following form:

$$\dot{\boldsymbol{\epsilon}}^{\text{cr}} = \frac{3A}{2} \left[ \frac{\sigma_{\text{vM}}}{(1-\omega)} \right]^n \left( \frac{\boldsymbol{s}}{\sigma_{\text{vM}}} \right),$$

where  $\boldsymbol{s}$  is the stress deviator. The generalized damage evolution equation depends on the isochronous equi-damage surface, analogously to Eq. (7.1):

$$\dot{\omega} = B \frac{(\sigma^*)^\kappa}{(1-\omega)^\mu}.$$

In addition to the interpretation of the scalar damage parameter  $D$  as a material deterioration, Chaboche [23] presents the possibility to describe the coupled damage evolution due to different processes, such as plasticity, creep and fatigue:

$$\begin{aligned} dD_1 &= f_1(\phi, \alpha, D_1, D_2, D_3, \dots) d\sigma, \\ dD_2 &= f_2(\phi, \alpha, D_1, D_2, D_3, \dots) dt, \\ dD_3 &= f_3(\phi, \alpha, D_1, D_2, D_3, \dots) dN, \end{aligned}$$

where  $\phi$  is the so called forcing variable, which has the meaning of stress or inelastic strain, depending on the described process.

### 7.2.1.2 Anisotropic damage

If the non-proportionality of loading takes place, the damaged state in the material becomes anisotropic. It requires anisotropic continuum damage theory. Such theories are basically built as the generalization of the isotropic theories, with the introduction of damage as the vectorial or tensorial variable. The anisotropic theory of Murakami and Ohno [86] interprets the material damage as the reduction of the effective area due to cavity formation and the stress concentration at the cavities. The second-rank tensorial damage variable in the unit volume is defined as follows:

$$\boldsymbol{\Omega} = \frac{1}{S_{\text{g}}(V)/3} \sum_{k=1}^N \int \left[ \boldsymbol{n}^{(k)} \otimes \boldsymbol{n}^{(k)} \right] dS_{\text{g}}^{(k)}, \quad (7.4)$$

where  $dS_{\text{g}}^{(k)}$  and  $\boldsymbol{n}^{(k)}$  with  $(k = 1 \dots N)$  denote the area of grain boundary, occupied by the  $k$ th cavity and the vector, normal to the grain boundary, respectively.  $S_{\text{g}}(V)$  is the total area of the grain boundaries in  $V$ . If  $\Omega_j$  are the principal values and  $\boldsymbol{n}_j$  are the principal directions, Eq. (7.4) reduces to

$$\boldsymbol{\Omega} = \Omega_j \boldsymbol{n}_j \otimes \boldsymbol{n}_j,$$

where  $\Omega_j$  is specified as the cavity density in three principal directions.

The evolution equation of the tensorial damage variable is written in the following form:

$$\dot{\mathbf{\Omega}} = \left\langle \frac{\chi(\boldsymbol{\sigma})^*}{A} \right\rangle^r [\gamma \mathbf{I} + (1 - \gamma) \mathbf{n}^{(1)} \otimes \mathbf{n}^{(1)}],$$

where  $\chi(\boldsymbol{\sigma})^*$  is the invariant, describing the isochronous surface analogous to presented in Eq. (7.3),  $\mathbf{n}^{(1)}$  is the direction of the maximum principal stress,  $A$ ,  $r$  and  $\gamma$  are material parameters. The effective stress in this case is represented as:

$$\tilde{\mathbf{S}} = \frac{1}{2} [\boldsymbol{\Gamma} : \boldsymbol{\sigma} + (\boldsymbol{\Gamma} : \boldsymbol{\sigma})^T],$$

where the asymmetrical fourth-order tensor  $\boldsymbol{\Gamma}$  is constructed on the damage tensor  $\mathbf{\Omega}$ . The constitutive equations of viscoplasticity are obtained involving the effective stress concept and are written as:

$$\dot{\boldsymbol{\varepsilon}}_p = \frac{3}{2} \dot{P} \frac{\tilde{\mathbf{S}}'}{J_2(\tilde{\mathbf{S}})},$$

with the evolution equation for the isotropic hardening

$$\dot{P} = \left[ \frac{J_2(\tilde{\mathbf{S}})}{K} \right]^n P^{-n/m},$$

where  $\tilde{\mathbf{S}}'$  is the deviator of  $\tilde{\mathbf{S}}$  and  $K$ ,  $n$ ,  $m$  are material model parameters.

Chaboche [24] improves the following theory by additional description of elastic region for damaged material and equivalent equations of viscoplasticity for undamaged and damaged materials. An asymmetrical fourth-order damage tensor  $\mathbf{D}$  is described through the characterization of effective elastic modulus for damaged and undamaged states:

$$\mathbf{D} = \mathbf{I} - \tilde{\boldsymbol{\Lambda}} : \boldsymbol{\Lambda}^{-1}.$$

The stress in damaged material in the elastic region can be expressed as follows:

$$\boldsymbol{\sigma} = (\mathbf{I} - \mathbf{D}) : \boldsymbol{\Lambda} : \boldsymbol{\varepsilon}^{\text{el}}.$$

With the representation of the effective stress

$$\tilde{\boldsymbol{\sigma}} = (\mathbf{I} - \mathbf{D})^{-1} : \boldsymbol{\sigma},$$

the law of viscoplastic flow is written as:

$$\dot{\boldsymbol{\varepsilon}}_p = \frac{3}{2} \left[ \frac{\tilde{\sigma}_{\text{VM}}}{K} \right]^n P^{-n/m} \frac{(\mathbf{I} - \mathbf{D})^{-1} : \tilde{\boldsymbol{\sigma}}'}{\tilde{\sigma}_{\text{VM}}},$$

where  $\tilde{\sigma}_{\text{VM}} = \sqrt{\frac{3}{2} \tilde{\mathbf{s}} \cdot \tilde{\mathbf{s}}}$  and  $\tilde{\mathbf{s}}$  is the deviatoric part of the effective stress  $\tilde{\boldsymbol{\sigma}}$ .

Another important aspect in damage modeling is the crack closure effect under compression. An overview on this phenomena is given, for example, in [12] and is determined as the damage deactivation. For the isotropic damage case Lemaitre [71] proposed to stop the damage growth by introducing the parameter  $h$  in front of the scalar damage variable in the expression for the effective principal stress in the case of compression:

$$\tilde{\sigma}_1 = \frac{\sigma_1}{1 - hD}, \quad \text{if } \sigma_1 < 0.$$

The parameter  $h$  is usually taken around 0.2, so the accumulated damage during compression still gives a small contribution. For the multiaxial state of the stress this approach is extended through the decomposition of the stress tensor on the positive and negative parts. In terms of the principal stress directions the spectral decomposition has the form [71]:

$$\boldsymbol{\sigma} = \sum_{i=1}^3 \sigma_i \mathbf{n}_i \otimes \mathbf{n}_i,$$

$$\boldsymbol{\sigma}^+ = \sum_{i=1}^3 H(\sigma_i) \sigma_i \mathbf{n}_i \otimes \mathbf{n}_i, \quad \boldsymbol{\sigma}^- = \sum_{i=1}^3 H(-\sigma_i) \sigma_i \mathbf{n}_i \otimes \mathbf{n}_i,$$

where  $H$  is the Heaviside's function of the principal stress component. Another possibility to account damage activation and deactivation by means of the Heaviside's function is described in [3].

For the anisotropic damage case the accounting of the different damage effect in tension and compression leads to the serious complications and model sophistication. For the non-proportional loading case such theories can lead to the discontinuities in the stress-strain response [65, 66, 139].

## 7.2.2 Non-proportional loading experiments

For the first time the results of the non-proportional creep tests were published by Trampczynski et al. [125]. The authors tested tubular specimen made of aluminium alloy and pure copper. These two materials are specifically chosen due to their different rupture behavior under the multi-axial state of stress. As it was already mentioned in Sect. 7.2.1.1 the rupture in copper is governed by the maximum principal tensile stress, at the same time for aluminium the rupture criteria is the maximum effective stress. Thus, the non-proportionality of the loading leads to the change of magnitude and the direction of whether the principal or the effective stress.

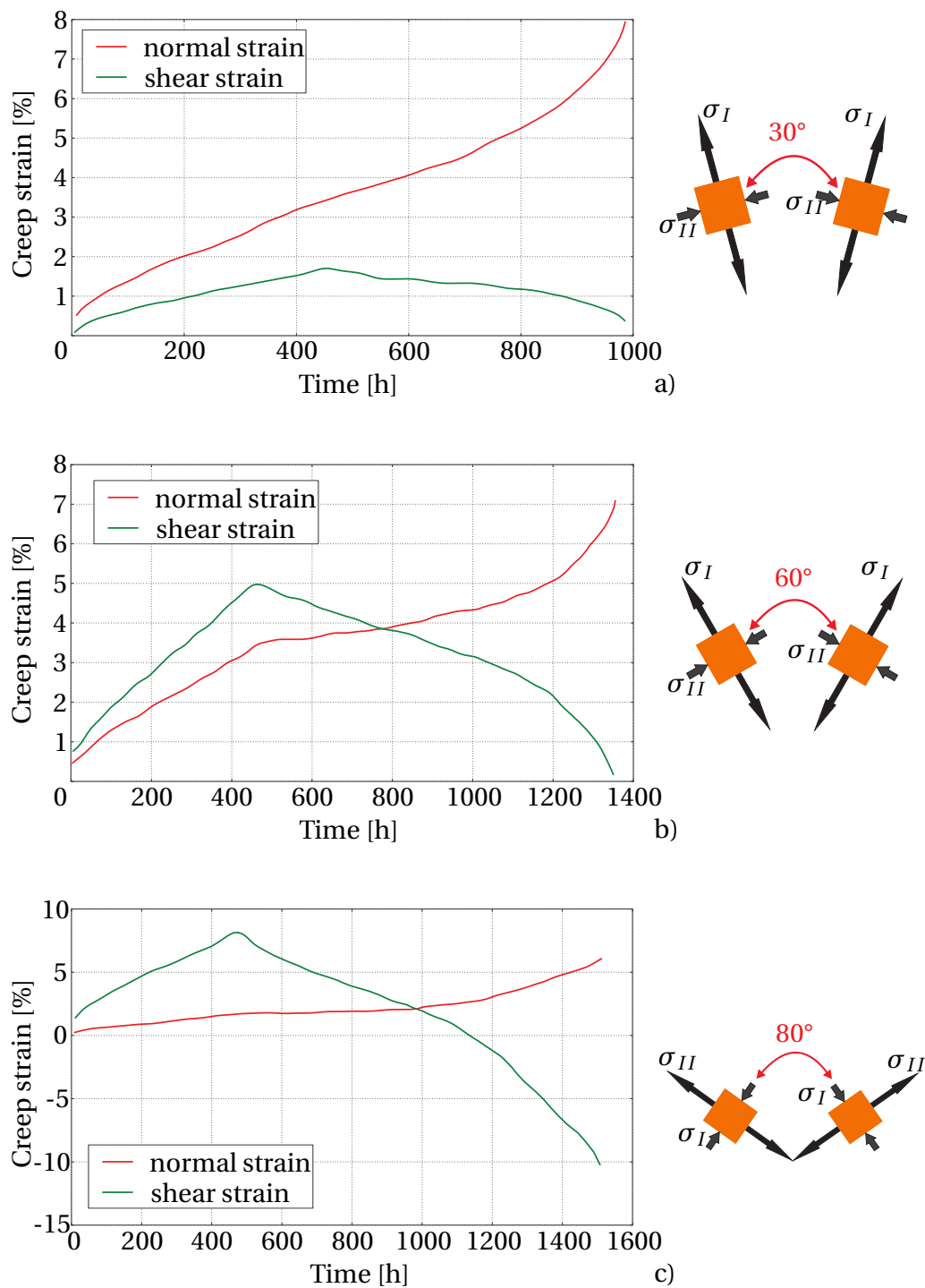


**Figure 7.4** Creep curves of the axial and torsional strains of the non-proportional loading tests [87] with the principal stress direction rotation at : a) 30°; b) 60°; c) 80°.

The experimental conditions were chosen according to this phenomena. The authors performed the test under constant tension and reversed torsion, leading to the main stress direction rotation at  $33.7^\circ$ . The obtained creep curve revealed significant creep strain rate decrease after the reversion of torsion. In addition, the prolongation of time to rupture in comparison to the tests without reversion of torsion was observed. In order to confirm and to extend results of [125] the analogous tests were performed by Murakami and Sanomura [87] with the principal stress rotation at  $30^\circ$ ,  $60^\circ$  and  $80^\circ$ . The reported creep curves are depicted in Fig. 7.4. The non-proportional loading tests of 304 type steel at  $593^\circ\text{C}$  are given in [69]. The axial and torsional strain evolution over time of the aluminium alloy are published in [15].

An attempt to predict the time to rupture of the non-proportional loading tests Murakami and Sanomura [87] is made in [3, 73] among others. In [73] the constitutive model of the material includes the second-order damage tensor, introduced in Murakami and Ohno [86]. The evolution equation of the creep damage is written in terms of a so called modified stress tensor, in which the compressive principal stresses are replaced by zeroes. The time to ruptures are calculated based of the failure criterion, written in the form of a scalar-valued function of the stress tensor, the stress deviator and the parameter, defining the ultimate strength of the undamaged material. The calculated time to rupture is overestimated the experimental one for the cases of the principal stress rotation on the  $30^\circ$  and  $60^\circ$  and underestimated for the case of  $80^\circ$  principal stress rotation.

### **7.2.3 Description of the non-proportional loading test with unit cell model**

The unit cell, consisting of 80 grains and the grain size  $210\ \mu\text{m}$  is built. The grain boundary region thickness ratio to the grain size is set equal to 0.1 in order to avoid stress peaks due to distorted element's geometry, as it is recommended in Sect. 5.6. The represented unit cell is tested with the material model parameters set, presented in Table 7.1.

The tensile loading of the unit cell is performed in different directions and magnitudes. The tension in  $\mathbf{x}$  direction is constant during the whole test for both loading variants. For the case of proportional loading the tension in  $\mathbf{y}$  direction is added in order to represent the multiaxial state of stress. The non-proportional loading is represented by the change at the time 5 hours the tension from  $\mathbf{y}$  to  $\mathbf{z}$  direction. For both loading regimes the magnitude of the

**Table 7.2** Scheme of the applied loading

| Non-proportional loading |               |           | Proportional loading |               |           |
|--------------------------|---------------|-----------|----------------------|---------------|-----------|
| Loading direction        | Stress, [MPa] | Time, [h] | Loading direction    | Stress, [MPa] | Time, [h] |
| $x$                      | 30            | 0–12      | $x$                  | 30            | 0–12      |
| $y$                      | 15            | 0–5       | $y$                  | 15            | 0–12      |
| $z$                      | 15            | 5–12      | $z$                  | 15            | —         |

principal stresses is kept the same. The loading conditions are summarized in Table 7.2.

In Fig. 7.5 the evolution with time of the averaged total strain in the  $x$  direction is shown. The evident time to rupture prolongation after the non-proportional loading test is observed as well as the creep strain rate decrease after the principal stress rotation.

In order to confirm the influence of the grain boundary damage on the time to rupture prolongation, the cross-sections of the unit cell after 9 hours of testing under proportional and non-proportional loadings are plotted. In Fig. 7.6 one can see the damaged state within the cross-section of the unit

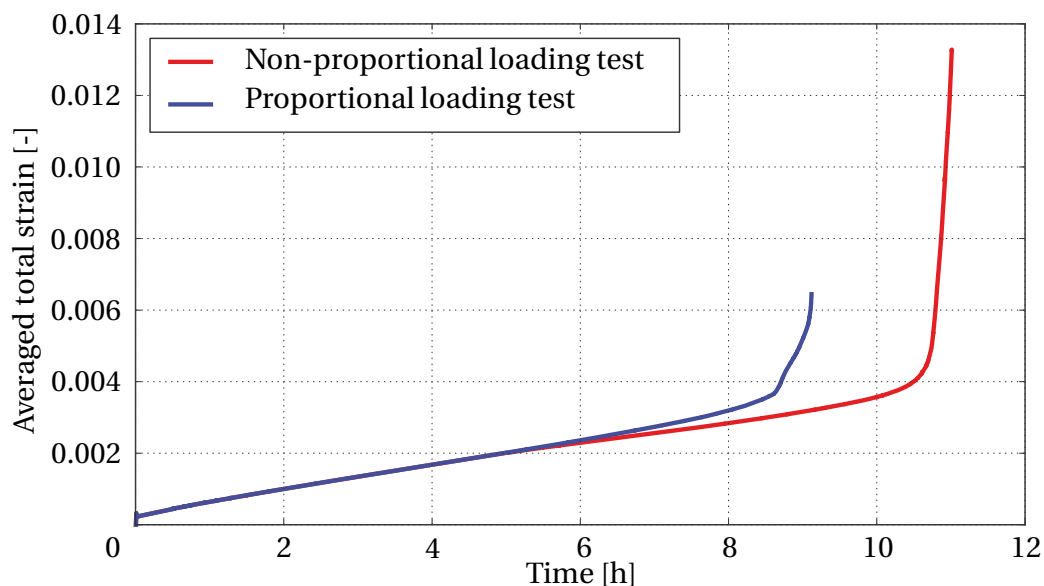


**Figure 7.5** Simulated creep curves for proportional and non-proportional tests. For the non-proportional loading test the stress rotation occurs after 5 hours of loading

cells described above. Under the damaged state the coefficient in front of the steady-state creep strain rate in Eq. (4.3) is understood, defining the influence of the cavitation on the creep strain rate. In the diagram, corresponding to the non-proportional loading case the area of damaged grain boundaries is lower than in the case of proportional one. It means that the principal stress rotation stops damage growth in some grain boundaries and activates it in another one, which were undamaged before. In general the material of the unit cell behaves as the less damaged under the new applied stress, which leads to the prolongation of the time to rupture.

Thus, the influence of the grain boundary damage on the prolongation of time to rupture for the non-proportional loading case is confirmed by the performed tests under polycrystalline unit cells.

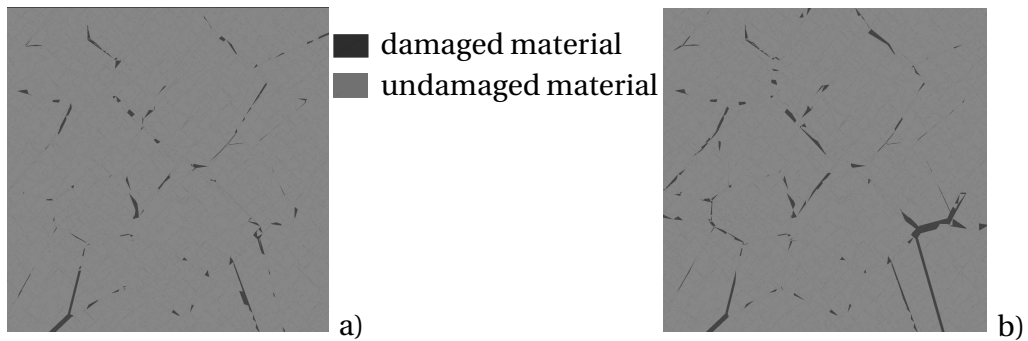


**Figure 7.6** Damage distribution within the cross section of the unit cell after 9 hours of creep test: a) non-proportional loading; b) proportional loading

---

## Conclusions and outlook

The current thesis deals with the investigation of the grain boundary cavitation in polycrystalline aggregates. The main idea was to perform the simulation in the following manner that only some micromechanisms directly influencing the cavitation process are included. These are power law creep in the grain interior, grain boundary sliding and growth of grain boundary cavities. Other phenomena, which take place during creep and influence the creep curve, such as dislocations and vacancies movement, subgrains and slip bands formation etc. are not analyzed. This assumption is taken on the one hand due to complexity of these mechanisms and on the other hand in order to investigate the pure contribution of chosen mechanisms.

To achieve this aim the numerical procedure is developed allowing to construct the geometry of a polycrystalline aggregate by means of the unit cell. The anisotropic nature of the grain interior material is introduced by the randomly oriented coordinate system for each grain.

The contribution of the above mentioned mechanisms on each of three creep stages is analyzed. The decrease of the creep strain rate at the beginning of the creep deformation, denoting the primary creep stage takes place due to hardening. The hardening in the polycrystalline material occurs due to microstructural change in dislocation density, their interaction with obstacles, etc. (see Sect. 2.3.1). After applying of load on the unit cell grains start to deform with the different magnitude. This occurs due to the fact, that some of them have more preferable orientation to the applied stress than others. The following from it heterogeneity in deformations leads to the hardening of the unit cell. The analysis of the averaged creep response of the unit cell during

the primary creep stage is discussed in Sect. 7.1.1. The direct dependence of the deformation level and presence of the primary creep stage on the level of material anisotropy is shown. The represented in the current work hardening due to interaction of grains usually gives around 1/10 to the total hardening observed in polycrystal. To improve the current model the hardening due to dislocation rearrangement should be included in the the evolution equation for the creep strain rate (2.36).

In the current work the deformation of the polycrystal is simulated by the power law creep of the grain interior material and the grain boundary sliding. On the averaged creep curve of the unit cell the secondary stage is characterized by the minimum creep strain rate, which is held during significant life time.

The value of minimum creep strain rate is characterized by the material parameter set for the grain interior material such as power law constant and power law exponent, determined in Sect. 2.3.3. Another factor, showing the influence on the value of minimum creep strain rate is the grain size and shape. This belongs to the investigation of statistical representability of the unit cell and is in details discussed in Sects. 5.4, 5.4.

The special grain boundary region represents the sliding of mutual grains. The grain boundary sliding by itself leads to the minimum creep strain rate increase by 10% for copper [7], which is by itself insufficient for the cavitation acceleration. Nevertheless the presents of the grain boundary region, with the described in Sect. 3.2 material behavior, leads to the significant stress concentrations, which force the cavity growth. The following observation within the numerical simulation if fully consistent with the experimental one [7]. The modeling of the secondary creep stage is discussed in Sects. 3.2, 7.1.2.

The tertiary creep stage is characterized by the creep strain rate increase, which can be caused by both grain material softening and grain boundary cavitation. It is known that, depending of the actual material properties and deformation mechanism, the softening in the polycrystalline material can occur due to subgrain coarsening, precipitate coarsening and decrease in dislocation density [33]. In these cases a smooth increase of the minimum creep strain rate, denoting beginning of the tertiary stage can be observed. The cavities growth and subsequent interlinkage leads to the material degradation and the rapid strain rate increase. The averaged creep curves of the tensile tested unit cells are presented and discussed in Sect. 7.2.3. The smoother tertiary stage as it can be observed in the experimental data (see Sect. 6.3) can be obtained by introduction of softening mechanism in the material model.

The case of non-proportional loading is analyzed. The creep strain rate reduction after the principal stresses rotation is observed, leading to the prolongation of the time to rupture. The dependence of the time to rupture on the direction of the cavitated grain boundaries is proved. Thus, the complex of processes, occurring in the material during non-proportional loading is qualitatively reproduced with the developed polycrystal model.



## APPENDIX

## A

## Derivation of elasticity equations in engineering constants

One can rewrite Eq. (2.1) in the inverse form, representing the dependence of the elastic strain tensor on the stress tensor components:

$$\begin{aligned} \boldsymbol{\varepsilon}^{\text{el}} = & \frac{1}{3}\alpha_1 \text{tr}\boldsymbol{\sigma} \mathbf{I} \\ & + \alpha_2 \left[ \sigma_{11} \left( \mathbf{g}_1 \otimes \mathbf{g}_1 - \frac{1}{3}\mathbf{I} \right) + \sigma_{22} \left( \mathbf{g}_2 \otimes \mathbf{g}_2 - \frac{1}{3}\mathbf{I} \right) + \sigma_{33} \left( \mathbf{g}_3 \otimes \mathbf{g}_3 - \frac{1}{3}\mathbf{I} \right) \right] \\ & + \alpha_3 \left[ \tau_{12} \left( \mathbf{g}_1 \otimes \mathbf{g}_2 + \mathbf{g}_2 \otimes \mathbf{g}_1 \right) + \tau_{13} \left( \mathbf{g}_1 \otimes \mathbf{g}_3 + \mathbf{g}_3 \otimes \mathbf{g}_1 \right) \right. \\ & \left. + \tau_{23} \left( \mathbf{g}_2 \otimes \mathbf{g}_3 + \mathbf{g}_3 \otimes \mathbf{g}_2 \right) \right], \end{aligned} \quad (\text{A.1})$$

where  $\alpha_1 = 1/\lambda_1$ ,  $\alpha_2 = 1/\lambda_2$ ,  $\alpha_3 = 1/\lambda_3$  are new material model parameters. If one performs the tensile test in the direction  $\mathbf{g}_1$  with the stress magnitude  $\sigma_0$ , the elasticity law (A.1) reduces to the following formula:

$$\begin{aligned} \boldsymbol{\varepsilon}^{\text{el}} = & \mathbf{g}_1 \otimes \mathbf{g}_1 \left( \frac{1}{3}\alpha_1 \sigma_0 + \frac{2}{3}\alpha_2 \sigma_0 \right) - \mathbf{g}_2 \otimes \mathbf{g}_2 \left( \frac{1}{3}\alpha_2 \sigma_0 - \frac{1}{3}\alpha_1 \sigma_0 \right) \\ & - \mathbf{g}_3 \otimes \mathbf{g}_3 \left( \frac{1}{3}\alpha_2 \sigma_0 - \frac{1}{3}\alpha_1 \sigma_0 \right). \end{aligned}$$

The value of the normal strain is determined as the strain tensor projection on the direction  $\mathbf{g}_1$ :

$$\varepsilon_n = \sigma_0 \frac{1}{3} (\alpha_1 + 2\alpha_2) \quad (\text{A.2})$$

and the values of the transverse strains are determined as projections of the strain tensor on the directions  $\mathbf{g}_2$  and  $\mathbf{g}_3$ :

$$\varepsilon_t = -\sigma_0 \frac{1}{3} (\alpha_2 - \alpha_1). \quad (\text{A.3})$$

From the definition of the elastic modulus and Poisson's ratio one can write:

$$\sigma_0 = E\varepsilon_n, \quad \varepsilon_t = -\nu\varepsilon_n. \quad (\text{A.4})$$

Combining Eqs. (A.4) and (A.2), (A.3) one can express the material parameters  $\alpha_1$  and  $\alpha_2$  through the engineering constants in the following form:

$$\alpha_1 = \frac{1-2\nu}{E}, \quad \alpha_2 = \frac{1+\nu}{E}. \quad (\text{A.5})$$

The elastic properties of the crystals depend on their orientation, so it is necessary to mention, that in the present derivation the elastic modulus  $E$  and the Poisson's ratio  $\nu$  in the [001] crystallographic direction are understood. This is illustrated in Fig. 2.4.

If one performs the shear test in the plane with normal  $\mathbf{g}_1$  in the direction  $\mathbf{g}_2$  with the stress magnitude  $\tau_{12}$  the elastic stress tensor has the form:

$$\boldsymbol{\varepsilon} = \alpha_3 \tau_{12} (\mathbf{g}_1 \otimes \mathbf{g}_2 + \mathbf{g}_2 \otimes \mathbf{g}_1). \quad (\text{A.6})$$

From the definition of the shear modulus as

$$\gamma_{12} = \frac{1}{G} \tau_{12}$$

it follows:

$$\alpha_3 = \frac{1}{2G}, \quad (\text{A.7})$$

where  $G$  is the shear modulus of the single crystal copper in the [001] crystallographic direction.

The next task is to obtain the dependencies between parameters  $\alpha_1$ ,  $\alpha_2$ ,  $\alpha_3$  and  $\lambda_1$ ,  $\lambda_2$  and  $\lambda_3$ . Let us represent the traces of both the strain and the stress tensors:

$$\text{tr}\boldsymbol{\sigma} = \lambda_1 \text{tr}\boldsymbol{\varepsilon}, \quad \text{tr}\boldsymbol{\varepsilon} = \alpha_1 \text{tr}\boldsymbol{\sigma}. \quad (\text{A.8})$$

From this one can easily determine:

$$\lambda_1 = \frac{1}{\alpha_1} = \frac{E}{1-2\nu}. \quad (\text{A.9})$$

Let us consider some calculations:

$$\boldsymbol{\sigma} \cdot \left( \mathbf{g}_1 \otimes \mathbf{g}_1 - \frac{1}{3} \mathbf{I} \right) = \mathbf{g}_1 \cdot \boldsymbol{\sigma} \cdot \mathbf{g}_1 - \frac{1}{3} \text{tr}\boldsymbol{\sigma},$$

$$\mathbf{g}_1 \cdot \boldsymbol{\sigma} \cdot \mathbf{g}_1 = \frac{1}{3} \lambda_1 \text{tr}\boldsymbol{\varepsilon} + \frac{2}{3} \lambda_2 \varepsilon_{11},$$

$$\boldsymbol{\sigma} \cdot \left( \mathbf{g}_1 \otimes \mathbf{g}_1 - \frac{1}{3} \mathbf{I} \right) = \frac{2}{3} \lambda_2 \varepsilon_{11},$$

$$\sigma_{11} - \frac{1}{3} \text{tr} \boldsymbol{\sigma} = \frac{2}{3} \lambda_2 \varepsilon_{11}.$$

The expression  $\sigma_{11} - \frac{1}{3} \text{tr} \boldsymbol{\sigma}$  can be calculated from Eq. (2.1) as follows:

$$\sigma_{11} - \frac{1}{3} \text{tr} \boldsymbol{\sigma} = \lambda_2 \left( \varepsilon_{11} - \frac{1}{3} \text{tr} \boldsymbol{\varepsilon} \right). \quad (\text{A.10})$$

The analogous derivations for the elasticity law in the inverse form Eq.(A.1) lead to the formula:

$$\boldsymbol{\varepsilon} \cdot \left( \mathbf{g}_1 \otimes \mathbf{g}_1 - \frac{1}{3} \mathbf{I} \right) = \left[ \frac{1}{3} \alpha_1 \text{tr} \boldsymbol{\sigma} + \alpha_2 \sigma_{11} \left( 1 - \frac{1}{3} \right) - \frac{1}{3} \text{tr} \boldsymbol{\varepsilon} \right] = \frac{2}{3} \alpha_2 \sigma_{11},$$

$$\varepsilon_{11} - \frac{1}{3} \text{tr} \boldsymbol{\varepsilon} = \frac{2}{3} \alpha_2 \sigma_{11},$$

and finally:

$$\varepsilon_{11} - \frac{1}{3} \text{tr} \boldsymbol{\varepsilon} = \frac{1+\nu}{E} \left( \sigma_{11} - \frac{1}{3} \text{tr} \boldsymbol{\sigma} \right). \quad (\text{A.11})$$

Substituting Eq. (A.10) in Eq. (A.11) one can get the expression of  $\lambda_2$  in engineering constants:

$$\lambda_2 = \frac{E}{1+\nu}. \quad (\text{A.12})$$

From Eq. (2.1) the shear stress  $\sigma_{12}$  follows as:

$$\tau_{12} = \mathbf{g}_1 \cdot \boldsymbol{\sigma} \cdot \mathbf{g}_2 = \frac{1}{2} \lambda_3 \gamma_{12}. \quad (\text{A.13})$$

From Eq. (A.1) the correspondent shear strain is  $\gamma_{12} = 2\alpha_3 \tau_{12}$  and consequently the shear stress:

$$\tau_{12} = \frac{\lambda_3}{2} \gamma_{12}. \quad (\text{A.14})$$

By combination of the Eqs. (A.13), (A.14) and (A.7) one can get the expression for  $\lambda_3$ :

$$\lambda_3 = 2G. \quad (\text{A.15})$$



## APPENDIX

**B**

---

## Micrographs of the copper specimens

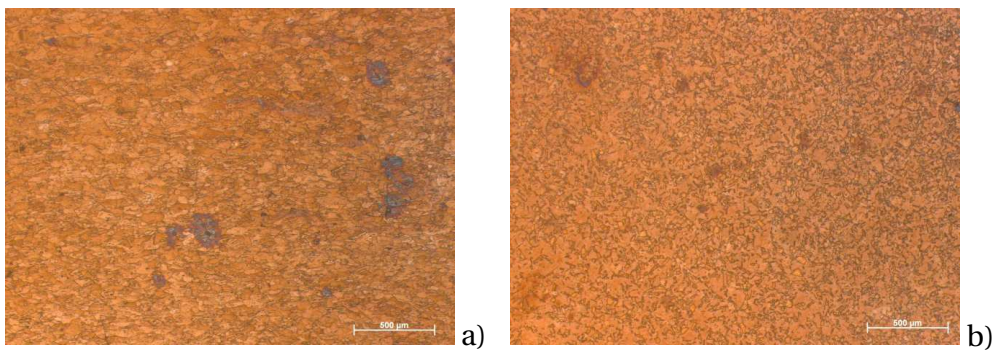


**Figure B.1** Micrographs of the specimen in the initial state (original magnification 50x): a) longitudinal section; b) cross-section

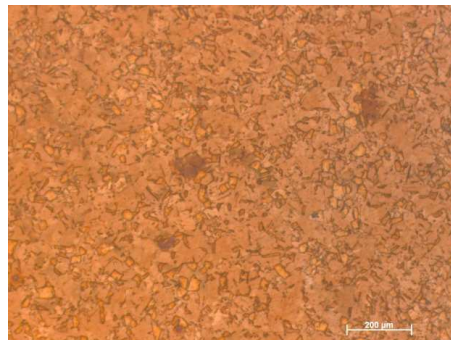


**Figure B.2** Micrographs of longitudinal section of the specimen in the initial state (original magnification 100x)

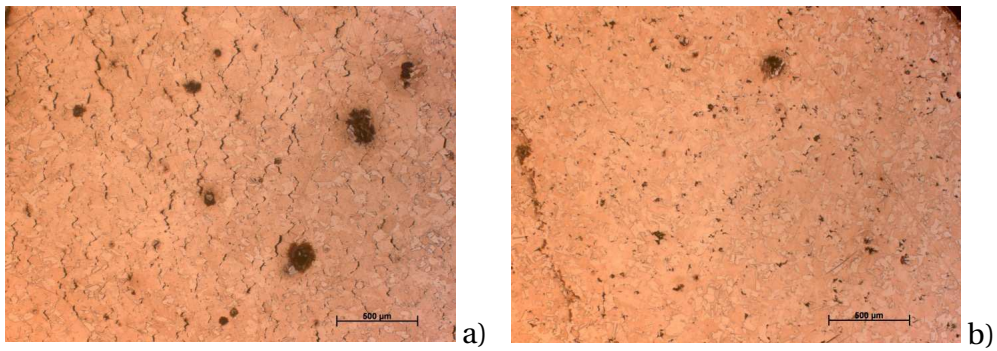


**Figure B.3** Micrographs of the specimen 11, tested 1 hour at 30 MPa (original magnification 50x): a) longitudinal section; b) cross-section

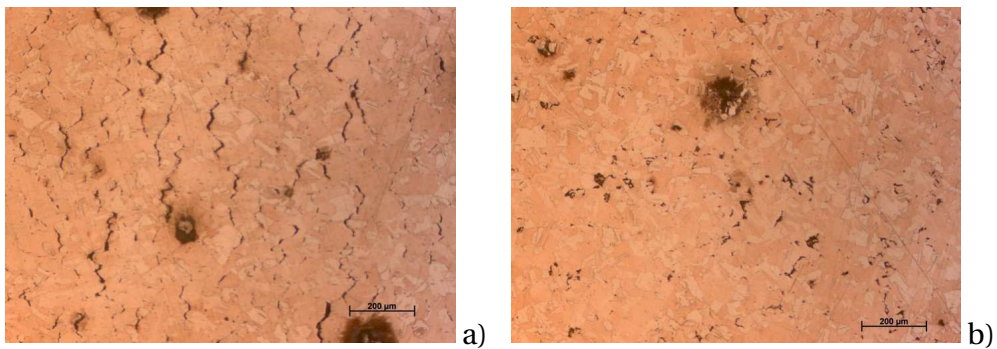


**Figure B.4** Micrographs of the specimen 11, tested 1 hour at 30 MPa (original magnification 100x): a) longitudinal section; b) cross-section

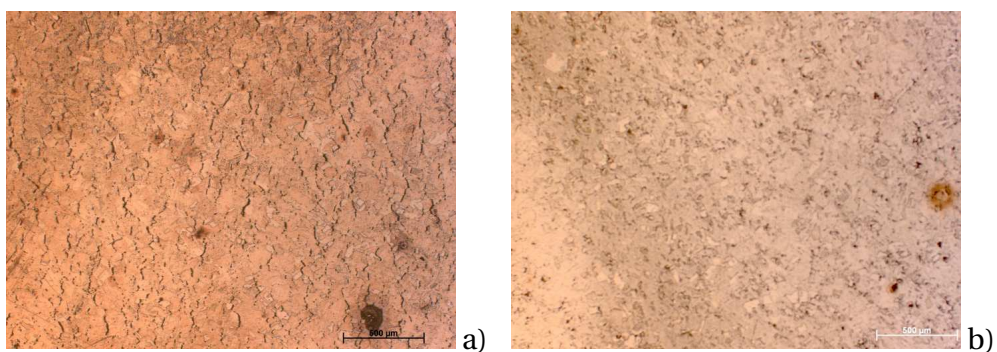


**Figure B.5** Micrographs of the specimen 4, tested 20 hours at 10 MPa (original magnification 500x): a) longitudinal section; b) cross-section

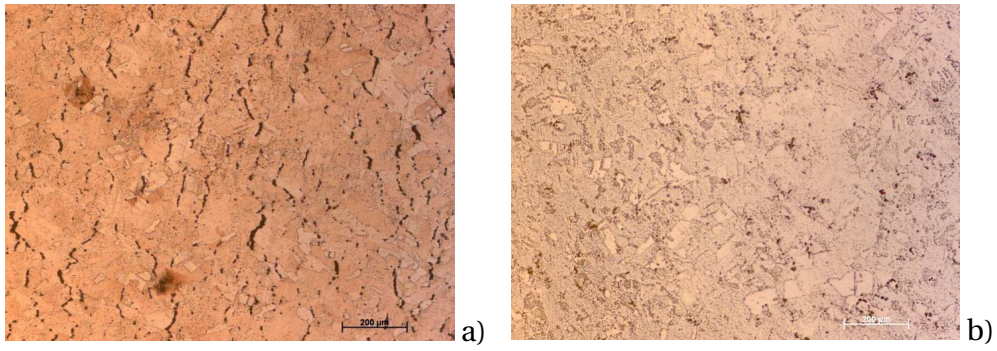


**Figure B.6** Micrographs of the specimen 4, tested 20 hours at 10 MPa (original magnification 100x): a) longitudinal section; b) cross-section



## APPENDIX

## C

## Crystallographic planes and directions in copper crystal

**Table C.1** First octahedral slip system

| $k$ | Slip direction, $\mathbf{b}_{\text{oct1}}^k$       | Normal to the slip plane, $\mathbf{v}_{\text{oct1}}^k$            |
|-----|--|---|
| 1   | $\frac{1}{\sqrt{2}}(\mathbf{g}_2 - \mathbf{g}_3)$  | $\frac{1}{\sqrt{3}}(\mathbf{g}_1 + \mathbf{g}_2 + \mathbf{g}_3)$  |
| 2   | $\frac{1}{\sqrt{2}}(-\mathbf{g}_1 + \mathbf{g}_3)$ |   |
| 3   | $\frac{1}{\sqrt{2}}(\mathbf{g}_1 - \mathbf{g}_2)$  |   |
| 4   | $\frac{1}{\sqrt{2}}(\mathbf{g}_2 - \mathbf{g}_3)$  | $\frac{1}{\sqrt{3}}(-\mathbf{g}_1 + \mathbf{g}_2 + \mathbf{g}_3)$ |
| 5   | $\frac{1}{\sqrt{2}}(\mathbf{g}_1 + \mathbf{g}_3)$  |   |
| 6   | $\frac{1}{\sqrt{2}}(-\mathbf{g}_1 - \mathbf{g}_2)$ |   |
| 7   | $\frac{1}{\sqrt{2}}(\mathbf{g}_2 + \mathbf{g}_3)$  | $\frac{1}{\sqrt{3}}(-\mathbf{g}_1 + \mathbf{g}_2 - \mathbf{g}_3)$ |
| 8   | $\frac{1}{\sqrt{2}}(\mathbf{g}_1 - \mathbf{g}_3)$  |   |
| 9   | $\frac{1}{\sqrt{2}}(-\mathbf{g}_1 - \mathbf{g}_2)$ |   |
| 10  | $\frac{1}{\sqrt{2}}(\mathbf{g}_2 + \mathbf{g}_3)$  | $\frac{1}{\sqrt{3}}(\mathbf{g}_1 + \mathbf{g}_2 - \mathbf{g}_3)$  |
| 11  | $\frac{1}{\sqrt{2}}(\mathbf{g}_1 - \mathbf{g}_2)$  |   |
| 12  | $\frac{1}{\sqrt{2}}(\mathbf{g}_1 + \mathbf{g}_3)$  |   |

**Table C.2** Second octahedral slip system

| $k$ | Slip direction, $\mathbf{b}_{\text{oct2}}^k$                       | Normal to the slip plane, $\mathbf{v}_{\text{oct2}}^k$            |
|-----|--|---|
| 1   | $\frac{1}{\sqrt{6}}(\mathbf{g}_1 - 2\mathbf{g}_2 + \mathbf{g}_3)$  | $\frac{1}{\sqrt{3}}(\mathbf{g}_1 + \mathbf{g}_2 + \mathbf{g}_3)$  |
| 2   | $\frac{1}{\sqrt{6}}(\mathbf{g}_1 + \mathbf{g}_2 - 2\mathbf{g}_3)$  |   |
| 3   | $\frac{1}{\sqrt{6}}(-2\mathbf{g}_1 + \mathbf{g}_2 + \mathbf{g}_3)$ |   |
| 4   | $\frac{1}{\sqrt{6}}(-\mathbf{g}_1 - 2\mathbf{g}_2 + \mathbf{g}_3)$ | $\frac{1}{\sqrt{3}}(-\mathbf{g}_1 + \mathbf{g}_2 + \mathbf{g}_3)$ |
| 5   | $\frac{1}{\sqrt{6}}(2\mathbf{g}_1 + \mathbf{g}_2 + \mathbf{g}_3)$  |   |
| 6   | $\frac{1}{\sqrt{6}}(-\mathbf{g}_1 + \mathbf{g}_2 - 2\mathbf{g}_3)$ |   |
| 7   | $\frac{1}{\sqrt{6}}(-2\mathbf{g}_1 - \mathbf{g}_2 + \mathbf{g}_3)$ | $\frac{1}{\sqrt{3}}(-\mathbf{g}_1 + \mathbf{g}_2 - \mathbf{g}_3)$ |
| 8   | $\frac{1}{\sqrt{6}}(\mathbf{g}_1 - \mathbf{g}_2 - 2\mathbf{g}_3)$  |   |
| 9   | $\frac{1}{\sqrt{6}}(\mathbf{g}_1 + 2\mathbf{g}_2 + \mathbf{g}_3)$  |   |
| 10  | $\frac{1}{\sqrt{6}}(2\mathbf{g}_1 - \mathbf{g}_2 + \mathbf{g}_3)$  | $\frac{1}{\sqrt{3}}(\mathbf{g}_1 + \mathbf{g}_2 - \mathbf{g}_3)$  |
| 11  | $\frac{1}{\sqrt{6}}(-\mathbf{g}_1 - \mathbf{g}_2 - 2\mathbf{g}_3)$ |   |
| 12  | $\frac{1}{\sqrt{6}}(-\mathbf{g}_1 + 2\mathbf{g}_2 + \mathbf{g}_3)$ |   |

**Table C.3** Cubic slip system

| $k$ | Slip direction, $\mathbf{b}_{\text{cub}}^k$        | Normal to the slip plane, $\mathbf{v}_{\text{cub}}^k$ |
|-----|--|---|
| 1   | $\frac{1}{\sqrt{2}}(-\mathbf{g}_2 + \mathbf{g}_3)$ | $\mathbf{g}_1$  |
| 2   | $\frac{1}{\sqrt{2}}(\mathbf{g}_2 + \mathbf{g}_3)$  |   |
| 3   | $\frac{1}{\sqrt{2}}(-\mathbf{g}_1 + \mathbf{g}_3)$ | $\mathbf{g}_2$  |
| 4   | $\frac{1}{\sqrt{2}}(\mathbf{g}_1 + \mathbf{g}_3)$  |   |
| 5   | $\frac{1}{\sqrt{2}}(\mathbf{g}_1 + \mathbf{g}_2)$  | $\mathbf{g}_3$  |
| 6   | $\frac{1}{\sqrt{2}}(\mathbf{g}_1 - \mathbf{g}_2)$  |   |



---

## Bibliography

- [1] SIMULIA ABAQUS 6.9. *ABAQUS Analysis User's Manual*. Dassault Systèmes Simulia Corp., USA, 2009.
- [2] H. Altenbach. Classical and nonclassical creep models. In H. Altenbach and J. Skrzypek, editors, *Creep and Damage in Materials and Structures*, pages 45 – 95. Springer, Wien, New York, 1999. CISM Lecture Notes No. 399.
- [3] H. Altenbach, C. Huang, and K. Naumenko. Modelling of creep damage under the reversed stress states considering damage activation and deactivation. *Technische Mechanik*, 21(4):273 – 282, 2001.
- [4] H. Altenbach, K. Naumenko, and P. Zhilin. A micro-polar theory for binary media with application to phase-transitional flow of fiber suspensions. *Continuum Mechanics and Thermodynamics*, 15:539 – 570, 2003.
- [5] A. Arsenlis, D. M. Parks, R. Becker, and V. V. Bulatov. On the evolution of crystallographic dislocation density in non-homogeneously deforming crystals. *J. Mech. Phys. Solids*, 52:1213 – 1246, 2004.
- [6] R. J. Asaro and A. Needleman. Texture development and strain hardening in rate dependent polycrystals. *Acta Metall.*, 33:923–953, 1985.
- [7] A. Ayensu and T. Langdon. The inter-relationship between grain boundary sliding and cavitation during creep of polycrystalline copper. *Metall. Mater. Trans. A*, 27A:901 – 907, 1996.

- [8] G. Backhaus. *Deformationsgesetze*. Akademie-Verlag, Berlin, 1983.
- [9] S. Bargmann and M. Ekh. Microscopic temperature field prediction during adiabatic loading using gradient extended crystal plasticity. *International Journal of Solids and Structures*, 50(6):899 – 906, 2013.
- [10] R. L. Bell and T. G. Langdon. An investigation of grain–boundary sliding during creep. *J. Mater. Sci.*, 2:313–323, 1967.
- [11] A. Bertram and J. Olschewski. Formulation of anisotropic linear viscoelastic constitutive laws by a projection method. *High temperature constitutive modeling: Theory and application ASME*, MD-Vol. 26, AMD-Vol. 121:129 – 137, 1991.
- [12] J. Besson, G. Cailletaud, J.-L. Chaboche, and S. Forest. *Non-Linear Mechanics of Materials*. Springer Netherlands, Dordrecht, Heidelberg, London, New York, 2010.
- [13] J. Betten. *Kontinuumsmechanik*. Springer, Berlin, 1993.
- [14] J. Betten. *Creep Mechanics*. Springer, Berlin, 2005.
- [15] J. Betten, S. Sklepus, and A. Zolochovsky. A creep damage model for initially isotropic materials with different properties in tension and compression. *Eng. Fract. Mech.*, 59:623 – 641, 1998.
- [16] E. W. Billington. *Introduction to the Mechanics and Physics of Solids*. Hilger, Bristol, 1986.
- [17] J. P. Boehler, editor. *Application of Tensor Functions in Solid Mechanics*. Springer, Wien, 1987.
- [18] A. Borbely, W. Blum, and T. Ungar. On the relaxation of the long-range internal stresses of deformed copper upon unloading. *Mater. Sci. Eng.*, A726:186 – 194, 2000.
- [19] J. T. Boyle and J. Spence. *Stress Analysis for Creep*. Butterworth, London, 1983.
- [20] BS EN ISO 204. Metallic materials. uniaxial creep testing in tension. method of test, 2009.
- [21] A. V. Burlakov, G. I. Lvov, and O. K. Morachkovsky. *Polzuchest' tonkikh obolochek (Creep of thin shells), [in Russian]*. Kharkov State Univ. Publ., Kharkov, 1977.

- [22] R. W. Cannon. The contribution of grain boundary sliding to axial strain during diffusion creep. *Phil. Mag.*, 25:6:1489–1497, 1971.
- [23] J.-L. Chaboche. Continuous damage mechanics – a tool to describe phenomena before crack initiation. *Nucl. Eng. Des.*, 64:233 – 247, 1981.
- [24] J.-L. Chaboche. Anisotropic creep damage in the framework of continuum damage mechanics. *Nuc. Eng. Des.*, 79:309 – 319, 1984.
- [25] J.-L. Chaboche. Constitutive equations for cyclic plasticity and cyclic viscoplasticity. *Int. J. Plast.*, 5:247 – 302, 1989.
- [26] Y. A. Chang and L. Himmel. Temperature dependence of the elastic constants of Cu, Ag, and Au above room temperature. *J. Appl. Phys.*, 37:3567 – 3572, 1966.
- [27] A. C. F. Cocks and M. F. Ashby. Intergranular fracture during power-law creep under multiaxial stresses. *Met. Sci.*, 14:395 – 402, 1980.
- [28] F. W. Crossman and M. F. Ashby. The non-uniform flow of polycrystals by grain-boundary sliding accommodated by power-law creep. *Acta Metall. Mater.*, 23:425–440, 1975.
- [29] L. T. Dame and D. C. Stouffer. Anisotropic constitutive model for nickel-base single crystal alloys: development and finite element implementation. *NASA contractor report*, CR-175015, 1986.
- [30] O. Diard, S. Leclercq, G. Rousselier, and G. Cailletaud. Evaluation of finite element based analysis of 3D multicrystalline aggregates plasticity: Application to crystal plasticity model identification and the study of stress and strain fields near grain boundaries. *Int. J. Plasticity*, 21:691–722, 2005.
- [31] S. Diebels. *Mikropolare Zweiphasenmodelle: Formulierung auf der Basis der Theorie Poröser Medien*. Habilitationsschrift, Universität Stuttgart, Bericht Nr. II-4, 2000.
- [32] A. D. Drozdov. *Finite Elasticity and Viscoelasticity: A Course in the Nonlinear Mechanics of Solids*. World Scientific, 1996.
- [33] B. F. Dyson and M. McLean. Micromechanism-quantification for creep constitutive equations. In S. Murakami and N. Ohno, editors, *IUTAM Symposium on Creep in Structures*, pages 3 – 16. Kluwer, Dordrecht, 2001.

- [34] K. Dzieciol, A. Borbely, F. Sket, A. Isaac, M. Di Michiel, P. Cloetens, Th. Buslaps, and A. R. Pyzalla. Void growth in copper during high-temperature power-law creep. *Acta Mater.*, 59:671–677, 2011.
- [35] W. Ehlers, E. Ramm, S. Diebels, and G.A. D’Addeta. From particle ensembles to cosserat continua: homogenisation of contact forces towards stresses and couple stresses. *Int. J. Solids and Structures*, 40: 6681 – 6702, 2003.
- [36] A. C. Eringen. *Microcontinuum Field Theories*, volume I: Foundations and Solids. Springer, New York, 1999.
- [37] A. C. Eringen. *Microcontinuum Field Theories*, volume II: Fluent Media. Springer, New York, 2001.
- [38] L. P. Evers, W. A. M. Brekelmans, and M. G. D. Geers. Scale dependent crystal plasticity framework with dislocation density and grain boundary effects. *Int. J. Solids Struct.*, 41:5209–5230, 2004.
- [39] B. Fedelich. A microstructural model for the monotonic and the cyclic mechanical behavior of single crystals of superalloys at high temperatures. *International Journal of Plasticity*, 18(1):1–49, 2002.
- [40] S. Forest, G. Cailletaud, and R. Sievert. A cosserat theory for elastoviscoplastic single crystals at finite deformation. *Arch. Mech*, 49: 705–736, 1997.
- [41] F. Fritzen, T. Böhlke, and E. Schnack. Periodic three-dimensional mesh generation for crystalline aggregates based on Voronoi tessellation. *Comput. Mech.*, 43:701 – 713, 2009.
- [42] R. C. Gifkins. Grain-boundary sliding and its accommodation during creep and superplasticity. *Metall. Trans. A*, 7A:1225–1232, 1976.
- [43] V. P. Gupta and P. R. Strutt. Dislocation structures in copper single crystals deformed in high temperature creep. *Can. J. Phys.*, 45:1213–1220, 1967.
- [44] M. E. Gurtin. A gradient theory of single-crystal viscoplasticity that accounts for geometrically necessary dislocations. *J. Mech. Phys. Solids*, 50:5–32, 2002.

- [45] C.-S. Han, H. Gao, Y. Huang, and W. D. Nix. Mechanism-based strain gradient crystal plasticity – I. Theory. *J. Mech. Phys. Solids*, 53:1188 – 1203, 2005.
- [46] S. Han, S. Li, and D. J. Smith. Comparison of phenomenological and crystallographic models for single crystal nickel base superalloys. I. Analytical identification. *Mech. Mater.*, 33:251 – 266, 2001.
- [47] S. Han, S. Li, and D. J. Smith. Comparison of phenomenological and crystallographic models for single crystal nickel base superalloys. II. Numerical simulations. *Mech. Mater.*, 33:267 – 282, 2001.
- [48] D. G. Harlow, H.-M. Lu, J. A. Hittinger, T. J. Delph, and R. P. Wei. A three-dimensional model for the probabilistic intergranular failure of polycrystalline arrays. *Modelling Simul. Mater. Sci. Eng.*, 4:261 – 279, 1996.
- [49] D. R. Hayhurst. Creep rupture under multi-axial states of stress. *J. Mech. Phys. Solids*, 20:381 – 390, 1972.
- [50] R. Hertzberg. *Deformation and Fracture Mechanisms of Engineering Materials*. John Wiley Sons, New York, 1989.
- [51] R. Hill. *The Mathematical Theory of Plasticity*. Materials Research and Engineering. Oxford University Press, London, 1950.
- [52] R. Hill. *The Mathematical Theory of Plasticity. Materials Research and Engineering*. Oxford University Press, London, 1950.
- [53] R. Hill. New horizons in the mechanics of solids. *J. Mech. Phys. Solids*, 5:66 – 74, 1956.
- [54] D. Hull and D. E. Rimmer. The growth of grain-boundary voids under stress. *Phil. Mag.*, 4:673 – 687, 1959.
- [55] J. W. Hutchinson. Bounds and self-consistent estimates for creep of polycrystalline materials. *Proc. R. Soc. London A*, 348:101 – 127, 1976.
- [56] T. H. Hyde, W. Sun, P. A. Agyakwa, P. H. Shipway, and J. A. Williams. Anisotropic creep and fracture behaviour of a 9CrMoNbV weld metal at 650°C. In J. J. Skrzypek and A. Ganczarski, editors, *Anisotropic Behaviour of Damaged Materials*, Lecture Notes in Applied and Computational Mechanics Vol. 9, pages 295–316. Springer Berlin Heidelberg, 2003.

- [57] L. M. Kachanov. *Osnovy teorii plastichnosti (Basics of the theory of plasticity)*, [in Russian]. Nauka, Moskva, 1969.
- [58] L. M. Kachanov. *Fundamentals of Fracture Mechanics [in Russian]*. Nauka, Moscow, 1974.
- [59] L. M. Kachanov. *Introduction to Continuum Damage Mechanics*. Kluwer Academic, Dordrecht, 1986.
- [60] M. Kachanov, B. Shafiro, and I. Tsukrov. *Handbook of Elasticity Solutions*. Kluwer Academic, Dordrecht, 2003.
- [61] S. Kaliszky. *Plastizitätslehre. Theorie und Technische Anwendungen*. VDI-Verlag, Düsseldorf, 1984.
- [62] M. E. Kassner and M. T. Perez-Prado. *Fundamentals of Creep in Metals and Alloys*. Elsevier, San Diego, 2004.
- [63] A. S. Khan and S. Huang. *Continuum Theory of Plasticity*. Wiley, New York, 1995.
- [64] Z. L. Kowalewski, L. Dietrich, and K. Turski. The effects observed in engineering materials after annealing and ageing processes. *J. Mater. Process. Tech.*, 119:165–173, 2001.
- [65] D. Krajcinovic and G. U. Fonseka. The continuous damage theory of brittle materials. Part 1: General theory. *J. Appl. Mech.*, 48:809–815, 1981.
- [66] D. Krajcinovic and G. U. Fonseka. The continuous damage theory of brittle materials. Part 2: Uniaxial and plane response modes. *J. Appl. Mech.*, 48:816–824, 1981.
- [67] A. Krawietz. *Materialtheorie. Mathematische Beschreibung des phänomenologischen thermomechanischen Verhalten*. Springer, Berlin, 1986.
- [68] M. Kuroda and V. Tvergaard. Studies of scale dependent crystal viscoplasticity models. *J. Mech. Phys. Solids*, 54:1789 – 1810, 2006.
- [69] Ho Kwang-II. An anisotropic creep damage model for multiaxial cyclic loading histories. *KSME Journal*, 4:92–97, 1990.
- [70] F. A. Leckie and D. R. Hayhurst. Creep rupture of structures. *Proc. Royal Soc. London*, 340:323–347, 1974.

- [71] J. Lemaitre. *A Course on Damage Mechanics*. Springer, Berlin, 1996.
- [72] I. M. Lifshitz. On the theory of diffusion–viscous flow of polycrystalline bodies. *Sov. Phys. JETP–USSR*, 17:909 – 920, 1963.
- [73] Z. Lis. Creep damage of solids under non–proportional loading. *Z. Angew. Math. Mech.*, 72:T 164 – T 166, 1992.
- [74] Y. Liu, Y. Kageyama, and S. Murakami. Creep fracture modeling by use of continuum damage variable based on Voronoi simulation of grain boundary cavity. *Int. J. Mech. Sci.*, 40:147 – 158, 1998.
- [75] T. Luther and C. Könke. Polycrystal models for the analysis of intergranular crack growth in metallic materials. *Eng. Fract. Mech.*, 76: 2332—2343, 2009.
- [76] R. Mahnken. Anisotropic creep modeling based on elastic projection operators with application to CMSX–4 superalloy. *Comput. Method. Appl. M.*, 191:1611–1637, 2002.
- [77] N. N. Malinin. *Prikladnaya teoriya plastichnosti i polzuchesti (Applied theory of plasticity and creep)*, [in Russian]. Mashinostroenie, Moskva, 1975.
- [78] N. N. Malinin. *Raschet na polzuchest' konstrukcionnykh elementov (Creep calculations of structural elements)*, [in Russian]. Mashinostroenie, Moskva, 1981.
- [79] G. A. Maugin. *The Thermomechanics of Plasticity and Fracture*. Cambridge University Press, Cambridge, 1992.
- [80] D. L. McDowell. Anisotropy of creep–fatigue deformation and damage under non–proportional loading. Technical report, Martin Marietta Energy Systems, May 1986.
- [81] V. Monchiet, C. Gruescu, O. Cazacu, and D. Kondo. A micromechanical approach of crack–induced damage in orthotropic media: Application to a brittle matrix composite. *Eng. Fract. Mech.*, 83:40 – 53, 2012.
- [82] F. C. Monkman and N. J. Grant. An empirical relationship between rupture life and minimum creep rate in creep–rupture tests. *Proc. ASTM*, 56:593 – 620, 1956.

- [83] T. Mori and K. Tanaka. Average stress in matrix and average elastic energy of materials with misfitting inclusions. *Acta Metall.*, 21:571 – 574, 1973.
- [84] H. B. Mühlhaus, editor. *Continuum Models for Materials with Microstructure*. John Wiley & Sons, Chichester, 1995.
- [85] S. Murakami. *Continuum Damage Mechanics – A Continuum Mechanics Approach to the Analysis of Damage and Fracture*. Springer, Dordrecht, Heidelberg, London, New York, 2012.
- [86] S. Murakami and N. Ohno. A continuum theory of creep and creep damage. In A. R. S. Ponter and D. R. Hayhurst, editors, *Creep in Structures*, pages 422 – 444. Springer, Berlin, 1981.
- [87] S. Murakami and Y. Sanomura. Creep and creep damage of copper under multiaxial states of stress. In A. Sawczuk and B. Bianchi, editors, *Plasticity Today – Modelling, Methods and Applications*, pages 535 – 551. Elsevier, London, New York, 1985.
- [88] A. Musienko and G. Cailletaud. Simulation of inter- and transgranular crack propagation in polycrystalline aggregates due to stress corrosion cracking. *Acta Mater.*, 57:3840 – 3855, 2009.
- [89] K. Naumenko and H. Altenbach. *Modeling of Creep for Structural Analysis*. Springer, Berlin, Heidelberg, 2007.
- [90] K. Naumenko, H. Altenbach, and A. Kutschke. A combined model for hardening, softening and damage processes in advanced heat resistant steels at elevated temperature. *International Journal of Damage Mechanics*, 20:578 – 597, 2011.
- [91] K. Naumenko, A. Kutschke, Y. Kostenko, and Th. Rudolf. Multi-axial thermo-mechanical analysis of power plant components from 9-12%Cr steels at high temperature. *Engineering Fracture Mechanics*, 78:1657 – 1668, 2011.
- [92] A. Needleman and J. R. Rice. Plastic creep flow effects in the diffusive cavitation of grain boundaries. *Acta Metall.*, 28:1315 – 1332, 1980.
- [93] S. Nemat-Nasser. *Micromechanics: Overall Properties of Heterogeneous Materials*. Elsevier, Amsterdam, 1999.

- [94] A. F. Nikitenko. Eksperimental'noe obosnovanie gipotezy suschestvovaniya poverkhnosti polzuchesti v usloviyakh slozhnogo nagruzheniya, (experimental justification of the hypothesis on existence of the creep surface under complex loading conditions), [in Russian]. *Problemy prochnosti*, (8):3 – 8, 1984.
- [95] T. Nørbygaard. *Studies of grain boundaries in materials subjected to diffusional creep*. PhD thesis, Risø National Laboratory, Roskilde, 2002.
- [96] N. Nouri, V. Ziaei-Rad, and S. Ziaei-Rad. An approach for simulating microstructures of polycrystalline materials. *Comput. Mech.*, 52:181–192, 2013.
- [97] F. K. G. Odqvist. *Mathematical Theory of Creep and Creep Rupture*. Oxford university press, Oxford, 1974.
- [98] F. K. G. Odqvist. Historical survey of the development of creep mechanics from its beginnings in the last century to 1970. In A. R. S. Ponter and D. R. Hayhurst, editors, *Creep in Structures*, pages 1 – 12. Springer, Berlin, 1981.
- [99] F. K. G. Odqvist and J. Hult. *Kriechfestigkeit metallischer Werkstoffe*. Springer, Berlin u.a., 1962.
- [100] N. Ohno, T. Mizuno, H. Kawaji, and I. Okada. Multiaxial creep of a nickel-base directionally solidified alloy: anisotropy and simulation. *Acta Metall. Mater.*, 40:559 – 567, 1992.
- [101] P. Onck and E. van der Giessen. Microstructurally-based modelling of intergranular creep fracture using grain elements. *Mech. Mater.*, 26:109 – 126, 1997.
- [102] O. O. Onofrio. *An approach for impression creep of lead free micro-electronic solders*. PhD thesis, Naval postgraduate school Monterey, California, 2002.
- [103] A. Orlova. Dislocation structure of copper single crystals in high-temperature creep test. *Czech. J. Phys. B*, 20:985 – 993, 1970.
- [104] A. Orlova and K. Kucharova. Interpretation of creep curves of double-notch copper single crystal specimens. *Philos. Mag. A*, 79:339 – 348, 1999.

- [105] C. Oytana, P. Delobelle, and A. Mermet. Constitutive equations study in biaxial stress experiments. *Trans. ASME. J. Engng Mat. & Techn.*, 104(3): 1 – 11, 1982.
- [106] V. Palmov. *Vibrations in Elasto-Plastic Bodies*. Springer, Berlin, 1998.
- [107] R. K. Penny and D. L. Marriott. *Design for Creep*. Chapman & Hall, London, 1995.
- [108] J.-P. Poirier. *Creep of Crystals*. Cambridge University Press, Cambridge, 1985.
- [109] Yu. N. Rabotnov. *Creep Problems in Structural Members*. North-Holland, Amsterdam, 1969.
- [110] W. A. Rachinger. Relative grain translations in the plastic flow of aluminium. *J. Inst. Met.*, 81:33 – 41, 1952.
- [111] R. Raj and M. F. Ashby. On grain boundary sliding and diffusional creep. *Metall. Trans.*, 2:1113–1127, 1971.
- [112] R. Raj and M. F. Ashby. Intergranular fracture at elevated temperatures. *Acta Metall.*, 23:653 – 666, 1975.
- [113] H. Riedel. *Fracture at High Temperatures*. Springer, Berlin, 1987.
- [114] G. J. Rodin and D. M. Parks. A self-consistent analysis of a creeping matrix with aligned cracks. *J. Mech. Phys. Solids*, 36:237 – 249, 1988.
- [115] E. Schmid and W. Boas. *Kristallplastizität*. Springer, Berlin, 1935.
- [116] F. Schubert, G. Fleury, and T. Steinhaus. Modelling of the mechanical behaviour of the single-crystal turbine alloy CMSX-4 during thermomechanical loading. *Modelling Simul. Mater. Sci. Eng.*, 8:947 – 957, 2000.
- [117] M. Y. Sheh and D. C. Stouffer. Anisotropic constitutive model for nickel-base single crystal superalloys. *NASA report*, CR-182157, 1988.
- [118] I. Simonovski and L. Cizelj. Towards modeling intergranular stress corrosion cracks on grain size scales. *Nucl. Eng. Des.*, 246:107 – 114, 2012.
- [119] J. Skrzypek and A. Ganczarski. *Modeling of Material Damage and Failure of Structures: Theory and Applications*. Foundations of Engineering Mechanics. Springer, Berlin Heidelberg, 1999.

- [120] J. J. Skrzypek. *Plasticity and Creep*. CRC Press, Boca Raton, 1993.
- [121] W. F. Smith. *Foundations of Materials Science and Engineering*. McGraw-Hill, Inc., Singapore, 1993.
- [122] O. V. Sosnin. K voprosu o suschestvovanii potentsiala polzuchseti, (on the question on existense of creep potential), [in Russian]. *Izv. AN SSSR Mekhanika tverdogo tela*, (5):85 – 89, 1971.
- [123] B. Svendsen and S. Bargmann. On the continuum thermodynamic rate variational formulation of models for extended crystal plasticity at large deformation. *Journal of the Mechanics and Physics of Solids*, 58(9):1253–1271, 2010.
- [124] P. Towashiraporn, G. Subbarayan, and C. S. Desai. A hybrid model for computationally efficient fatigue fracture simulations at microelectronic assembly interfaces. *Int. J. Solids Struct.*, 42:4468 – 4483, 2005.
- [125] W. A. Trampczynski, D. R. Hayhurst, and F. A. Leckie. Creep rupture of copper and aluminium under non-proportional loading. *J. Mech. Phys. Solids*, 29:353 – 374, 1981.
- [126] I. Tsukrov and M. Kachanov. Effective moduli of an anisotropic material with elliptical holes of arbitrary orientational distribution. *Int. J. Solids Struct.*, 37:5919 – 5941, 2000.
- [127] V. Tvergaard. Constitutive relations for creep in polycrystals with grain boundary cavitation. *Acta Metall.*, 32:1977 – 1990, 1984.
- [128] V. Tvergaard. Effect of grain boundary sliding on creep constrained diffusive cavitation. *J. Mech. Phys. Solids*, 33:447 – 469, 1985.
- [129] E. van der Giessen and V. Tvergaard. A creep rupture model accounting for cavitation at sliding grain boundaries. *Int. J. Fracture*, 48:153–178, 1991.
- [130] W. Voigt. *Lehrbuch der Kristallphysik*. Druck und Verlag von B. G. Teubner, Leipzig und Berlin, 1910.
- [131] R. von Mises. Mechanik der plastischen Formänderung von Kristallen. *ZAMM*, 8(3):161 – 185, 1928.

- [132] M. Vöse, F. Otto, B. Fedelich, and G. Eggeler. Micromechanical investigations and modelling of a Copper–Antimony–Alloy under creep conditions. *Mech Mater*, 69:41 – 62, 2014.
- [133] T. Watanabe. Grain boundary sliding and stress concentration during creep. *Metall. Trans. A*, 14A:531 – 545, 1983.
- [134] E. S. Wentzel. *Probability Theory [in Russian]*. Fizmatgiz, Moscow, 1962.
- [135] C. Westwood, J. Pan, and A. D. Crocombe. Nucleation, growth and coalescence of multiple cavities at a grain–boundary. *Eur. J. Mech. A–Solid.*, 23:579 – 597, 2004.
- [136] C. Westwood, J. Pan, L. Huirong, S. Kucherenko, and A. Crocombe. A simplified model for cavity growth along a grain–boundary by coupled surface and grain–boundary diffusion. *Eur. J. Mech. A–Solid.*, 19:17 – 30, 2000.
- [137] B. Wilshire and C. J. Palmer. Grain size effects during creep of copper. *Scripta Mater.*, 46:483 – 488, 2002.
- [138] S. Yefimov, I. Groma, and E. van der Giessen. A comparison of a statistical–mechanics based plasticity model with discrete dislocation plasticity calculations. *J. Mech. Phys. Solids*, 52:279 – 300, 2004.
- [139] J. W. Yu. On energy–based coupled elastoplastic damage theories: constitutive modeling and computational aspects. *Int. J. Solids Struct.*, 25:803 – 833, 1989.

# Lebenslauf

## Persönliche Daten

Name, Vorname: Ozhoga–Maslovskaja, Oksana  
Geburtsdatum: 17 Oktober 1986  
Geburtsort: Kharkiv  
Familienstand: ledig  
Nationalität: ukrainisch

## Schulbildung

1993–2003 Gymnasium, Kharkiv

## Studium

2003–2007 Bachelor of Science Technische Mechanik  
Nationale Technische Universität  
"Kharkiver Polytechnisches Institut",  
Kharkiv (Ukraine)

2007–2009 Master of Science Technische Mechanik  
Nationale Technische Universität  
"Kharkiver Polytechnisches Institut",  
Kharkiv (Ukraine)

## Berufserfahrung

2010–2013 Wissenschaftliche Mitarbeiterin  
Otto–von–Guericke–Universität,  
Magdeburg (Deutschland)

Magdeburg, 26.02.2014

Oksana Ozhoga–Maslovskaja